THE WAKSMAN FOUNDATION OF JAPAN INC.

Report of Researches in 2010

Dr. Selman A.Waksman

2011

Published by
THE WAKSMAN FOUNDATION OF JAPAN INC.
30-8 Daikyo-cho, Shinjuku-ku, Tokyo, Japan

THE WAKSMAN FOUNDATION OF JAPAN INC. Report of Researches in 2010

THE WAKSMAN FOUNDATION OF JAPAN INC.

Honorary President

Prince Takahito Mikasa

Board of Directors

Chairman : Ichiro Kitasato, Adviser, The Kitasato Institute.
Former Chairman of The Board, Meiji Seika Kaisya, Ltd.

Shogo Sasaki, Prof. Emeritus, Keio Univ.

Teruhiko Beppu, Prof. Emeritus, Tokyo Univ.

Takeshi Ishikawa, Vice President
Retirement Allowance Foundation of Private Colleges and Universities

Tadakatsu Shimamura, Prof. Emeritus, Showa Univ.

Toshiro Sato, Adviser, The Kitasato Institute.

Managing Director : Takeji Nishikawa, Prof. Emeritus, Keio Univ.

Comptroller : Yoshiharu Wakiyama, Senior Adviser, Kaken Pharmaceutical Co., Ltd.

Shirow Enoki, Chairman, Anges MG, Inc.

Councilors

Ryoichi Mori, Prof. Emeritus, Kyushu Univ.

Keizo Takemi, Prof., Tokai Univ.

Koichi Yamanishi, Director, General National Institute of Biomedical Innovation.

Sachiko Goto, Prof. Emeritus, Toho Univ.

Yoshihiro Miwa, President & CEO, Kowa Co., Ltd.

Isao Uchida, Senior Adviser, Yokogawa Electric Corporation.

Shigeo Koyasu, Prof., Keio Univ. Sch. Med.

Takashi Shoda, Chairman of the Board, Representative Director, Daiichi Sankyo Co., Ltd.

Yasuma Sugihara, Former Chairman and CEO, Mobil Sekiyu K.K.

2 0 1 1

Edited and Published by

THE WAKSMAN FOUNDATION OF JAPAN INC.

30-8 Daikyo-cho, Shinjuku-ku,
Tokyo 160-0015, Japan
http : //www.waksman.or.jp/
E-mail: toshihisa-sato@waksman.or.jp

Printed by

D CRAFT SEIKOU CO., LTD.

Tokyo, Japan

PREFACE (2000)

Since the Waksman Foundation published its first cinqueannual report in 1962, annual report followed regularly until 1986 without changing its style, i.e. yellow cover in B5 size. The royalties of patent of streptomycin expired in 1970 and the Foundation was forced to change the way of running. Fortunately, it manages to continue its activity by supporting the research activities of Japanese investigators and by encouraging them to take part in an international meeting and also by hosting scientific meetings with professional societies. The total number of support counts 628 research projects and costs approximately 4,500,000 U.S. dollars. The Foundation is administered by the Board of Directors consisting of 5-9 representatives of professional societies and Prince Takahito Mikasa as the honorary President.

At our recent business meeting it was decided unanimously to publish the reports of the researchers who recieved research grant from the Foundation for the past 15 years to commemorate the year 2000. To meet with the current style of a scientific journal the Foundation has adopted an international size and totally renewed the cover as you are aware of. From the new millennium on it is expected that the report from the awardees of the research grants will be distributed regularly each year.

Shozo Yokogawa
Chairman, Board of Directors,
The Waksman Foundation of Japan, Inc.

Preface to the First Report (1962)

It is indeed a privilege to take this opportunity to write a few words of introduction to the first report of the Waksman Foundation of Japan Inc., covering five years of its activities and comprising the results of the work of the first two years of research carried out by various scholars in Japan in the fields of microbiology and medical science, supported by this Foundation.

In 1952, I accepted the invitation from Keio University and the Kitasato Institute, to deliver the centennial lecture in honor of the great Japanese bacteriologist, Shibasaburo Kitasato. Before departing for Japan, I proposed to the trustees of the Rutgers Research and Educational Foundation which owned the patents on streptomycin, to share the royalties under the patent in Japan, for the support of research in microbiology and allied fields in that country. The trustees heartily approved my recommendation that I make such announcement to that effect.

Soon upon my arrival in Japan (December 17, 1952), I invited a group of eminent microbiologists, biochemists, and clinical investigators to meet with me in order to discuss the plan. Everyone present was very enthusiastic about the proposal. It was decided that a proper committee be selected to work out the plan of a Foundation under which the royalties were to be received and distributed for the support of Japanese investigators working in different universities in Japan and elsewhere, in the fields of microbiology and medical research. The committee recommended that a Board of Directors be selected and the proposed Foundation be named THE WAKSMAN FOUNDATION OF JAPAN INCORPORATION.

The Rutgers Research and Educational Foundation approved at once the above recommendations and issued a statement, signed by Dr. Lewis Webster Jones, President of the Foundation, to the effect that

"The Rutgers Research and Educational Foundation desires to emphasize that its principal concern is the advancement of scientific knowledge in the public interest and that it confidently expects that the Waksman Foundation for Microbiology and Medical Research in Japan will be similarly motivated, thereby serving the peoples of both countries."

This announcement was received with enthusiasm both by the scientific world and the popular press in Japan and in the United States. It took several years before the Waksman Foundation of Japan Inc. was properly organized, and before applications were received and approved. In 1958, I had the privilege of participating in the first official meetings of the Board of Directors of the Japanese Foundation and to greet personally the first group of scholars to whom grants had been made.

In summarizing these brief remarks in connection with the first cinqueannual report of the Waksman Foundation of Japan Inc., I would like to enphasize that this example of collaboration between universities and scientists of the United States and Japan may serve to encourage collaboration between scientific workers throughout the world towards a better understanding between men and women and towards a happier and healthier human race, so that all the nations on this earth can live in peace and that man may finally "break

his swords and build out of them plowshares" for the betterment of mankind as a whole.

Selman A. Waksman
Professor Emeritus
Rutgers-State University N. J., U. S. A.

The "Waksman Foundation of Japan Inc." was established in 1957 with the spirit of humanity by Dr. S.A. Waksman, Professor of Microbiology, Rutgers University, U.S.A. The Foundation's operations are possible only because Dr. S.A. Waksman and the Rutgers Research and Educational Foundation donated patent royalties he received from the production in Japan of the discovery, Streptomycin.

Because of these royalties, each year many Japanese scholars and research workers in the fields of Microbiology and medical science are encouraged and find it possible to continue their work. Especially, in accordance with Dr. Waksman's suggestion, the funds are distributed to scholars in local and economically hampered schools and laboratories and to those developing research workers who are endeavoring to expand in their fields. This thought of Dr. Waksman's is most appreciated, as it matches our Oriental phylosophy, and results in the search for a jewel among ordinary stones, which is the highest work of the science-leader.

Some five years have now passed since the start of this Foundation, and many persons have received aid through this period.

The reports which are presented herein cover the first and second group of research workers who received financial assistance from the Foundation.

Toshio Katow, M. D.
Executive Director

Contents

—— Report of Researches in 2010 ——

A novel mechanism for the generation and maintenance of memory T cells

Naoto Ishii

Department of Microbiology and Immunology, Tohoku University Graduate School of Medicine, Sendai 980-8575, Japan

Introduction

The adaptive immune responses to infection are mounted by the optimal differentiation of naïve T and B cells into effector cells, and subsequently into long-lived memory cells. Memory $CD8^+$ T cells represent the major effector arm of the adaptive immune system to maintain long-lived protective immunityagainst intracellular bacteria, protozoa, and viruses. Upon a subsequent infection by the same pathogen, pathogen-specific memory $CD8^+$ T cells that have been maintained in the absence of Ag are poised to respond quickly, specifically, and with sufficient amplitude to protect the host. Therefore, understanding the mechanisms underlying the generation and maintenance of memory $CD8^+$ T cells is critical, not only for contributing to basic immunology but also for improved clinical applications, such as the design of new vaccines.

Accumulating evidence shows that TCR signals and homeostatic cytokines, such as IL-7 and IL-15, are critical regulators of the generation and maintenance of $CD8^+$ memory T cells. TCR signals are essential for the survival of naïve T cells and the generation of functional memory T cells. However, the roles played by costimulatory signals in the generation and maintenance of $CD8^+$ memory T cells are still unclear. Among the T-cell costimulatory molecules are several TNF receptor superfamily members, including OX40 (CD134), CD27, and 4-1BB, which contribute to the survival and expansion of effector T cells. Some of these T cells subsequently differentiate into long-lived memory T cells. OX40's role in the generation of memory $CD4^+$ T cells has been intensively studied and convincingly demonstrated to be important. In addition, recent studies suggest that OX40 signals are also important for the generation of memory $CD8^+$ T cells, although how and when OX40 signals are required remains to be elucidated.

In the present study, we took advantage of a useful model for acute bacterial infection. This model combines infection by r*LM*-OVA (recombinant *Listeria monocytogenes* expressing OVA), which mimics the bacterial Ag during infection, with the MHC class I-restricted OVA-specific TCR-transgenic OT-I system. We also relied on the $KLRG1^{low}$ phenotype as a specific marker for memory precursor T cells, which helped us to investigate the role of OX40 signals during infection, to determine when the effector $CD8^+$ T cells undergo memory commitment. Finally, we used extensive adoptive transfer experiments to demonstrate the critical roles played by OX40 signals in both the generation and the maintenance of memory $CD8^+$ T cells.

Materials and Methods

Mice

Six- to eight-week-old female wild-type C57BL/6 mice were purchased from Japan SLC Inc. (Shizuoka, Japan). OX40 ligand (OX40L)-deficient mice and $Ly5.1^+$-C57BL/6 mice were previously described. OT-I TCR-transgenic mice were a gift from Dr. W. Heath (WEHI, Melbourne, Australia) and were used as a source of $CD8^+$ T cells specifically responsive

to the $OVA_{257-264}$ peptide. $Ly5.1^+$ wild-type OT-I and $Ly5.1^+$ $OX40^{-/-}$OT-I mice were generated in-house by intercrossing OT-I mice with $Ly5.1^+$ wild-type and $Ly5.1^+$ $OX40^{-/-}$ mice, respectively. All the mice were on a C57BL/6 background, and they were bred and maintained under specific pathogen–free conditions at the Institute for Animal Experimentation, Tohoku University Graduate School of Medicine. All procedures were performed according to protocols approved by the Institutional Committee for the Use and Care of Laboratory Animals of Tohoku University.

Microorganism, immunization, and assessment of bacterial burden

The recombinant *Listeria monocytogenes* expressing OVA (r*LM*-OVA) was previously described. Mice were infected via the tail vein with a sublethal dose of r*LM*-OVA (1×10^4 CFU; 0.1 LD_{50}) in 0.2 ml of PBS. To examine the protective function of memory T cells, the recipient mice that harbored long-lived wild-type or $OX40^{-/-}$ OT-I cells were re-challenged with a higher dose of r*LM*-OVA (1×10^5CFU). To evaluate the bacterial burden, the spleen and liver were removed and separately homogenized in 3 ml of PBS. Serial dilutions of each tissue extract were spread on BHI agar plates containing erythromycin, and the number of colonies was counted after incubation for 24-48 h at 37°C.

Antibodies

The following antibodies and reagents were purchased from BD Biosciences (San Diego, USA): anti-CD8-allophycocyanin, anti-TCR-Vα2-PE, anti-TCR-Vß5-FITC, anti-Ly5.1-biotin, anti-Ly5.1-allophycocyanin, anti-CD62L-FITC, anti-CD62L-biotin, anti-OX40-biotin, and streptavidin-allophycocyanin. Anti-mouse KLRG-allophycocyanin was purchased from eBioscience (San Diego, USA). The inhibitory anti-OX40L mAb (MGP34; rat IgG2c) was previously described. The anti-IL-7R α chain mAb (A7R34; rat IgG2a) was a gift from S. Nishikawa (CDB, RIKEN, Kobe, Japan). Control rat Ig was purchased from Cappel (Durham, USA). For staining OX40L and IL-7Rα, MGP34 and A7R34 were biotinylated and visualized using streptavidin-allophycocyanin.

Lymphocyte isolation, cell sorting, and adoptive transfer

Naïve $CD8^+$ T cells (1×10^4) were purified from the spleen of Ag-naïve wild-type OT-I or $OX40^{-/-}$ OT-I mice with the $Ly5.1^+$ congenic marker. They were then injected into the lateral tail vein of naïve $Ly5.2^+$ congenic mice that were infected with r*LM*-OVA 24 h after the cell transfer (first host). For the secondary adoptive transfer of memory T cells, $Ly5.1^+$ memory donor cells were isolated 40 days after infection as described above, and labeled with carboxy-fluorescein succinimidyl ester (CFSE) (Molecular Probes, Eugene, USA), as described previously.

Results

OX40 signals are dispensable for the expansion and function of activated $CD8^+$ T cells, but determine the number of the $KLRG1^{low}$ MPEC population.

OX40 signals are not essential for the initial proliferation of $CD4^+$ T cells during the priming phage of Ag stimulation, but significantly promote the survival and clonal expansion of effector $CD4^+$ T cells in the later effector phase. Indeed, the recipient mice harboring wild-type and $OX40^{-/-}$ donor cells showed a similar kinetics of bacterial burdens after r*LM*-OVA infection, and cleared the bacteria equally well from the spleen and liver by day 6 post-infection (data not shown). This suggests that both wild-type and $OX40^{-/-}$ donor cells were activated and differentiated under a similar inflammatory environment mediated by *Listeria* infection. Although previous reports demonstrated that OX40 signals enhanced granzyme B expression in effector $CD8^+$ T cells, wild-type and $OX40^{-/-}$ donor cells produced a comparable amount of granzyme B (data not shown). These results indicate that the OX40 signals are dispensable for the expansion and function of activated $CD8^+$ T cells during the acute phase of infection.

To investigate the phenotypic heterogeneity of

the effector $CD8^+$ T-cell population, we used KLRG1 expression to distinguish between short-lived effector cells ($KLRG1^{high}$) and MPECs ($KLRG1^{low}$), as well as the expression of the IL-7 receptor α chain (IL-7R) (high on MPECs) and CD62L. Flowcytometric analysis gated on KLRG1 expression at various time points after infection revealed phenotypic heterogeneity in the wild-type and $OX40^{-/-}$ effector T cells in the spleen. Six days after *Listeria* infection, effector $CD8^+$ T cells differentiated into the two distinct cell lineages: $KLRG1^{high}$ and $KLRG1^{low}$, in which the $KLRG1^{low}$ ($IL\text{-}7R^{high}$) population were expected to contain memory precursors. Although the total donor cell numbers in recipient mice harboring wild-type or $OX40^{-/-}$ OT-I cells were comparable even 10 days after infection, the subpopulation profiles were quite different in terms of KLRG1 expression. In particular, the percentage and the absolute number of $KLRG1^{low}$ MPECs in the $OX40^{-/-}$ OT-I cells were markedly lower than in the wild-type OT-I cells (Fig. 1A and 1B).

Collectively, these observations suggest that OX40 signals are necessary for the optimal generation of $KLRG1^{low}CD8^+$ MPECs, in spite of their dispensability for the effector function of activated $CD8^+$ T cells.

OX40 signals are essential for the generation of functional memory $CD8^+$ T cells.

We next assessed the accumulation of long-lived OT-I donor cells in the spleens of infected mice at the memory phase. About 2-fold more wild-type OT-I donor cells had accumulated than $OX40^{-/-}$ OT-I cells on day 30 (Fig. 2A). Intriguingly, on day 60 and until day 150 after infection, the number of persisting $OX40^{-/-}$ donor T cells in the spleen was markedly reduced compared with wild-type donor T cells (Fig. 2A). These results suggest that OX40 critically contributes to the generation and the maintenance of memory $CD8^+$ T cells.

Phenotypic analysis of the persisting donor cells on day 90 demonstrated that wild-type donor cells were predominantly $KLRG1^{low}IL\text{-}7R^{high}CD62L^{high}$ (Fig. 2B). In contrast, in the absence of OX40, a substantial percentage of the $IL\text{-}7R^{high}CD62L^{high}$ donor $CD8^+$ T cells strongly expressed KLRG1, indicating that the majority of long-lived $OX40^{-/-}$ donor T cells was unable to acquire the memory phenotype (Fig. 2B). In addition, consistent with a previous report, these data imply that a high expression of IL-7R on $OX40^{-/-}$ OT-I cells is not sufficient to support their survival.

Next, the functionality of long-lived wild-type and $OX40^{-/-}$ OT-I cells during in vitro recall responses was examined. Ninety days post-infection, whole splenocytes from each recipient mouse were collected and stimulated with $OVA_{257-264}$ peptide, and the synthesis of IL-2 and IFNγ was analyzed by intracellular staining. Long-lived $OX40^{-/-}$ OT-I donor cells, especially the $KLRG1^{low}$ population, failed to produce IL-2, while wild-type memory $CD8^+$ T cells secreted substantial amounts of IL-2; both kinds of donor cells produced IFNγ at the same level, regardless of KLRG1 expression (data not shown). In addition, 60% of wild-type $KLRG1^{low}$ cells produced IL-2, whereas only 34% of $OX40^{-/-}$ $KLRG1^{low}$ population were positive for IL-2, suggesting the importance of OX40 in IL-2 secretion by each $KLRG1^{low}$ T cell. The absolute number of IL-2–producing $KLRG1^{low}$ cells derived from $OX40^{-/-}$ OT-I cells in vitro was also markedly reduced.

OX40 is essential for the self-renewal potential of memory $CD8^+$ T cells.

Although the more rapid reduction of MECs in $OX40^{-/-}$ T cells during the contraction phase is one of the possible mechanisms for the failure of $OX40^{-/-}$ donor cells to generate memory T cells, it cannot fully explain their decrease after the contraction phase (between day 60 and day 150 in Fig. 2A). Therefore, we postulated that OX40 might also be implicated in the maintenance of memory T cells. Since the basal homeostatic proliferation contributes to the maintenance of memory $CD8^+$ T cells by mediating their Ag-independent self-renewal, we have addressed whether OX40 might be involved in the basal homeostatic proliferation. Wild-type memory OT-I or $OX40^{-/-}$ memory OT-I cell populations from the first host were isolated, labeled with CFSE, and then adoptively transferred into Ag-naïve wild-type second hosts. The basal homeostatic proliferation of

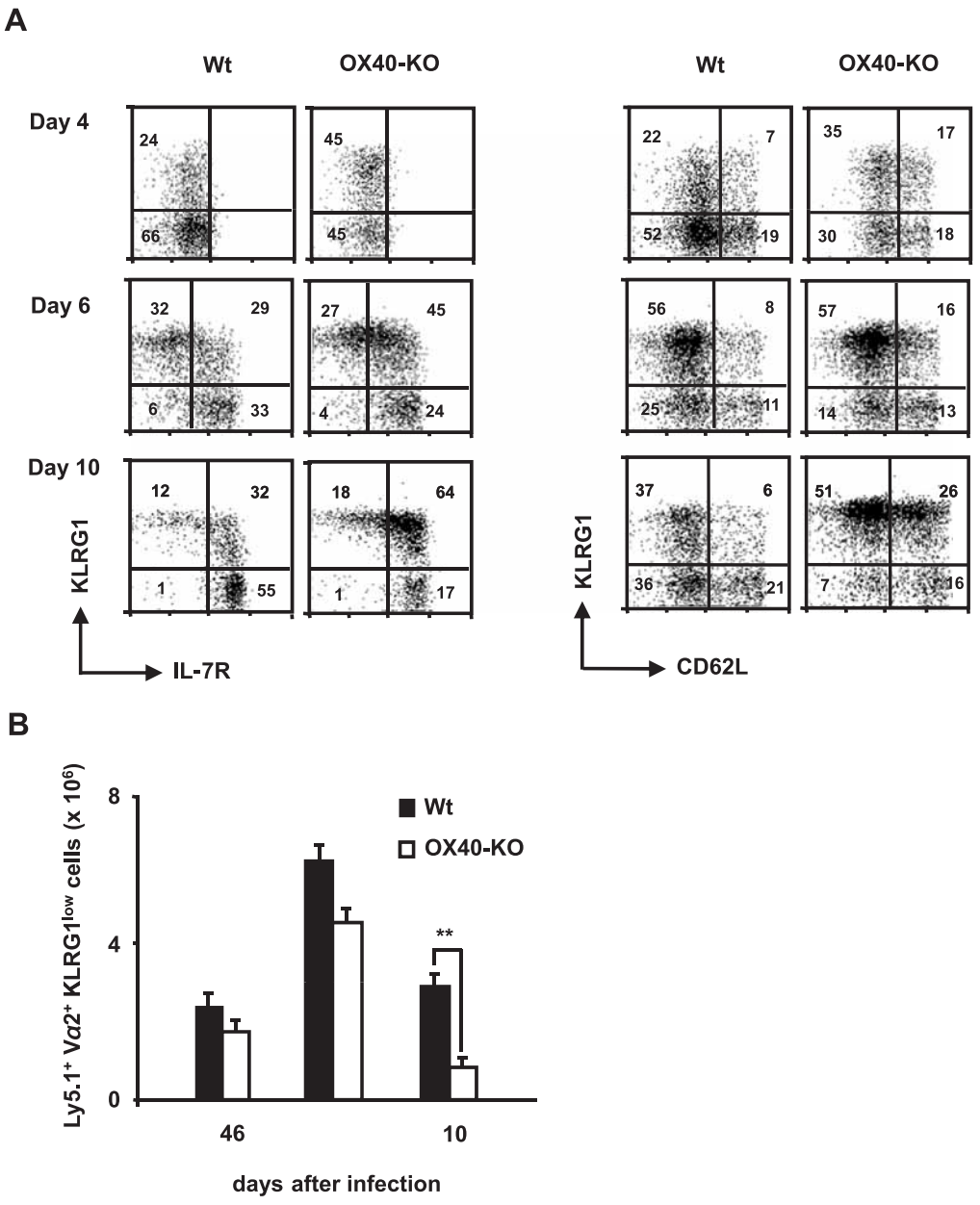

Fig. 1. OX40 signals are dispensable for the expansion and function of activated $CD8^+$ T cells, but determine the number of $KLRG1^{low}$ MPECs.

Purified naïve $Ly5.1^+$ OT-I or $Ly5.1^+$ $OX40^{-/-}$OT-I cells (1 x 10^4 each) were adoptively transferred i.v into $Ly5.2^+$ congenic wild-type mice that were infected with r*LM*-OVA (1 x 10^4CFU) 24 h after transfer. **A.** On the indicated days post-infection, the spleen were removed, and separately homogenized in PBS. The kinetic expression of KLRG1 and IL-7R (left), and KLRG1 and CD62L (right) on $Ly5.1^+$ wild-type OT-I or $Ly5.1^+$ $OX40^{-/-}$ OT-I donor cells was examined on the indicated days post-infection. The number in each quadrant indicates the percentage of each subset. Results shown are the expression profiles of $Ly5.1^+V\alpha2^+$ cells in pooled splenocytes from 3 mice, and are representative from each time point from one representative experiment of two. Similar results were obtained in two independent experiments. **B.** The absolute numbers of $KLRG1^{low}$ cells in $Ly5.1^+$ wild-type (■) and $OX40^{-/-}$ (□) OT-I donor cells were counted on the indicated days infection. Results represent the mean ± SD of the donor cell number from 4 mice per group. Similar results were obtained in two independent experiments.

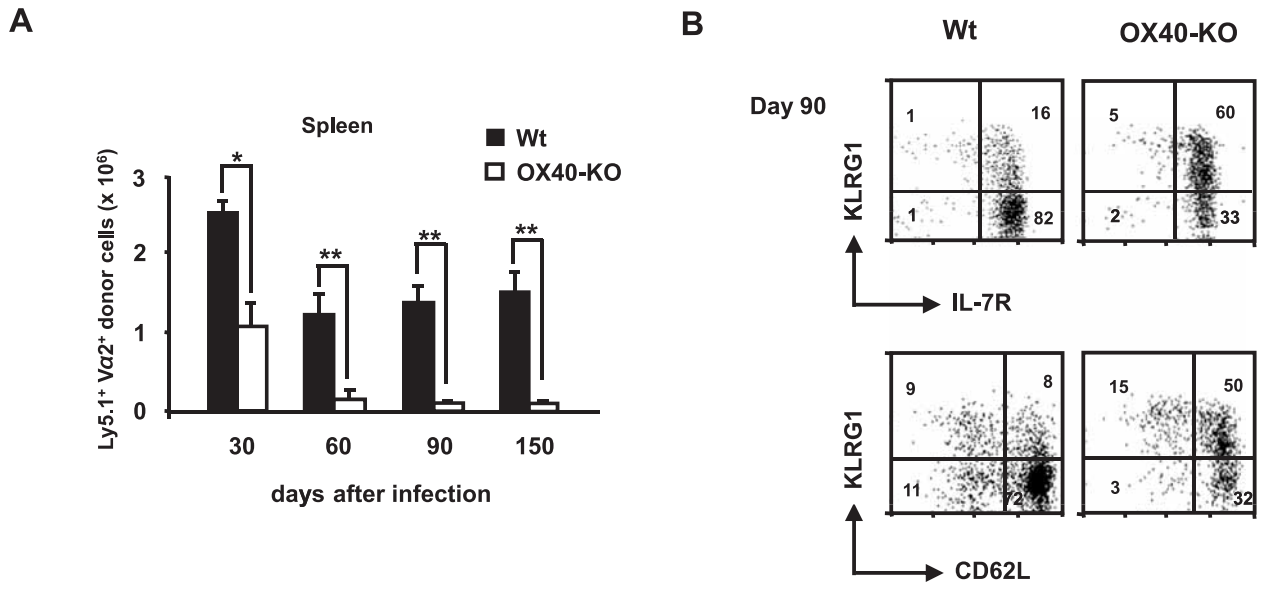

Fig. 2. OX40 signals are essential for the generation of memory CD8$^+$ T cells.
A. Purified naïve Ly5.1$^+$ OT-I or Ly5.1$^+$ OX40$^{-/-}$OT-I cells (1 x 10^4 each) were adoptively transferred i.v into Ly5.2$^+$ congenic wild-type mice that were infected with r*LM*-OVA (1 x 10^{4}CFU) 24 h after transfer. The absolute number of Ly5.1$^+$TCR-Vα2$^+$ donor cells in the spleens of recipient mice was counted on the indicated days after the infection. Results represent the mean $\pm$ SD of the donor cell numbers from 4 mice per group. Similar results were obtained in two independent experiments. **B.** The expression of KLRG1 and IL-7R (upper), and KLRG1 and CD62L (lower) on Ly5.1$^+$ long-lived OT-I or OX40$^{-/-}$ OT-I cells in the spleen of the recipient mice on day 90 after infection was examined. Results are representative of 4 mice in each group. Similar results were obtained in the 4 mice in each group.

these memory CD8$^+$ T cells was assessed by the dilution of CFSE intensity 30 days after transfer. When wild-type OT-I memory CD8$^+$ T cells were transferred, the KLRG1^{low} population divided between one and four times, but most of the KLRG1^{high} cells appeared to stop after one division (Fig. 3). The significantly greater self-renewal potential of the KLRG1^{low}long-lived CD8$^+$ T cells is concordant with their being memory CD8$^+$ T cells, which is consistent with the findings for viral infection. In striking contrast, long-lived KLRG1^{low} OX40$^{-/-}$ donor cells failed to undergo homeostatic proliferation, and their KLRG1^{high} population almost disappeared (Fig. 3). Furthermore, the absolute number of long-lived OX40$^{-/-}$ donor cells in the second host was much lower than that of wild-type donor cells (Fig. 3). These data indicate that OX40 signals critically mediate the basal homeostatic proliferation of memory CD8$^+$ T cells, especially KLRG1^{low}memory CD8$^+$ T cells.

We next addressed whether OX40 signals during the memory phase are responsible for the self-renewal of memory T cells. Persisting wild-type OT-I donor cells were isolated from the first host 40 days after infection, and adoptively transferred into an Ag-naïve wild-type or OX40L-deficient second host. In contrast to the OX40$^{-/-}$long-lived CD8$^+$ T cells, which could not divide, wild-type memory OT-I cells in the OX40L-deficient host exhibited a robust homeostatic proliferation and similar cell accumulation as in the wild-type host (data not shown). These transfer experiments imply that OX40 signals are not essential during the memory phase for the self-renewal of memory CD8$^+$ T cells, which may be programmed by previously provided OX40 signals.

Identification of the OX40 target genes involved in memory maintenance

OX40 signals are essential, not only for the survival of KLRG1^{low}memory precursor but also for

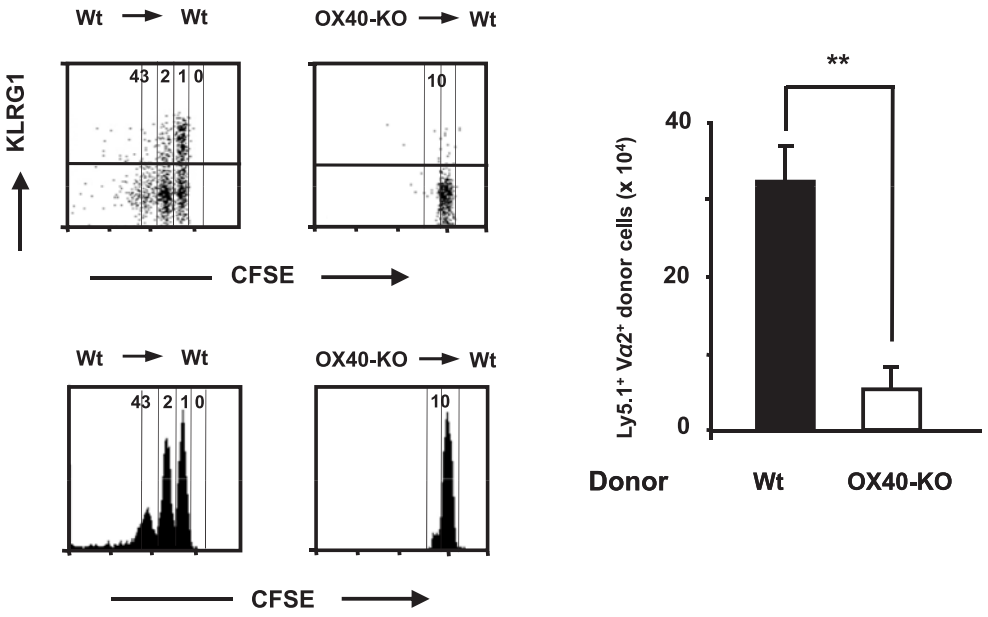

Fig. 3. OX40 is essential for the self-renewal potential of memory CD8$^+$ T cells. Long-lived Ly5.1$^+$ donor cells from the first host were transferred into Ag-naïve second host, and their homeostatic proliferation was assessed. **A.** Ly5.1$^+$ donor cells in the first host, which possessed either wild-type or OX40$^{-/-}$ donor cells, were collected 40 days after infection by using an AutoMACS cell sorter. The purified long-lived Ly5.1$^+$ donor cells from the first host were labeled with CFSE and transferred (1 x 10^6 in each group) into wild-type congenic mice (n=3). The dilution of CFSE intensity of Ly5.1$^+$TCR-Vα2$^+$ donor cells in the spleen of recipient mice was assessed by flowcytometry. The absolute number of Ly5.1$^+$TCR-Vα2$^+$ donor cells in the spleen of the second host was counted. The data shown in the flowcytometric analysis are representative of 3 mice per each group. The graph represents the mean ± SD of the absolute numbers of the donor T cells in the spleen of recipient mice (n = 3 in each group) on day 30 post transfer. Similar results were obtained in two independent experiments.

imprinting the self-renewing ability of memory CD8$^+$ T cells onto memory precursor cells during priming. We thus hypothesized that OX40 signals might induce an epigenetic and irreversible change in the memory precursor effector T cells, which may induce the memory precursor into the functional memory T cells.

To identify the genes, expression of which were changed in the memory precursor effector T cells by inhibiting OX40 signals, we examined DNA microarray analysis with the four indicated populations (OX40-KO KLRG1^{high}, OX40-KO KLRG1^{low}, WT KLRG1^{high}, and WT KLRG1^{low}) from the recipient mice 6 days after infection. Fig. 4 demonstrates several gene expression patterns. Among them, Otc, TGFb2, Flt2, IL-11, and Blr1, expression of which failed to be elevated in OX40-KO memory precursor cells as compared with the WT precursor cells, were found. To understand the physiological roles of these genes on memory T cell generation, further examination will be required.

Discussion

Recent findings have clearly demonstrated that effector CD8$^+$ T cells are phenotypically diverse in terms of KLRG1 expression, and indicate that KLRG1^{low} effector CD8$^+$ T cells become committed to the memory fate during acute viral infection. The present study has confirmed these observations in an acute bacterial infection model and further

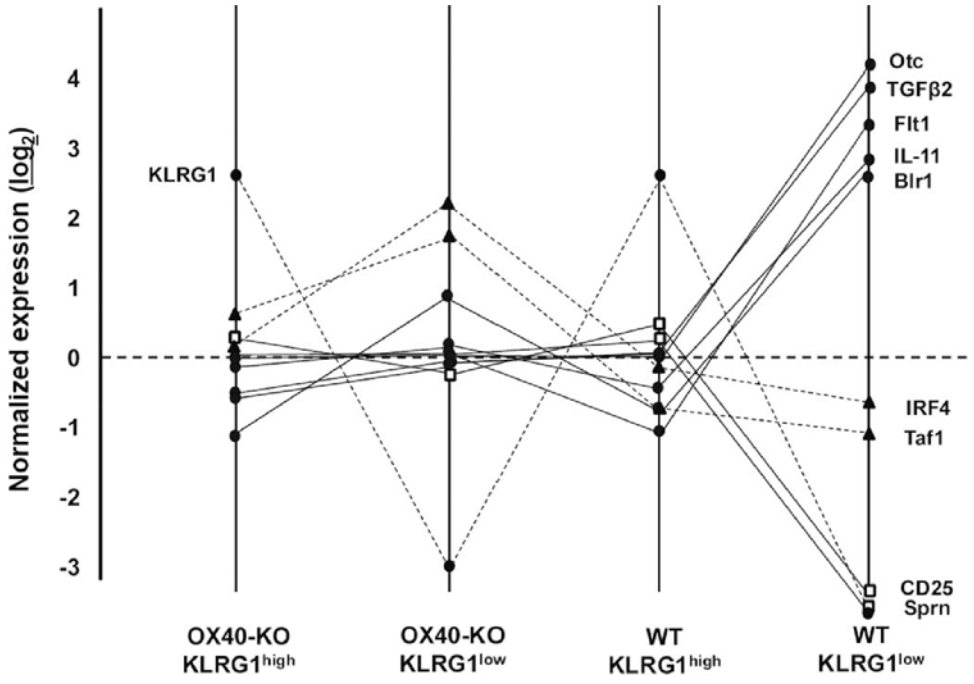

Fig. 4. DNA microarray analysis with memory precursor cells
Purified naïve Ly5.1$^+$ OT-I or Ly5.1$^+$ OX40$^{-/-}$OT-I cells (1 x 10^4 each) were adoptively transferred i.v into Ly5.2$^+$ congenic wild-type mice that were infected with r*LM*-OVA (1 x 10^{4}CFU) 24 h after transfer. Six days after infection, OX40-KO KLRG1^{high}, OX40-KO KLRG1^{low}, WT KLRG1^{high}, and WT KLRG1^{low} donor cell populations (1 x 10^6 each) were independently purified from the recipient and subjected to DNA microarray analysis. Normalized expression of several genes, expression of which was changed by the absence of OX40 is demonstrated.

obtained several new findings on the OX40 roles in the homeostasis of KLRG1^{low} effector and memory T cells. With regard to the OX40 signals' roles in the generation and homeostasis of memory CD8$^+$ T cells, several previous papers have suggested OX40 to be important for the survival of heterogeneous effector CD8$^+$ T cells. The present results demonstrate that OX40 signals promote the survival of KLRG1^{low} CD8$^+$ MPECs, a subset of effector T cells. Since OX40 stimulation directly induces NFκB-associated survival signals in activated T cells, the NFκB activation may be involved in the OX40-mediacted survival of KLRG1^{low} CD8$^+$ MPECs.

We also show here that OX40 signals critically potentiated the maintenance of the memory CD8$^+$ T cells. Furthermore, the OX40 signals activated during priming appeared to be sufficient to imprint the self-renewal potential of KLRG1^{low} memory CD8$^+$ T cells onto the MPECs (Fig. 3). In addition, we previously demonstrated using an acute viral infection model that OX40 signals during Ag-priming are required for the expansion of memory CD8$^+$ T cells during secondary infection. Therefore, OX40 signals during priming seem to imprint the memory competency onto CD8$^+$ MPECs. The OX40-mediated memory imprinting may indicate a novel role for T-cell costimulatory signals apart from the conventional survival signals. We thus have attempted to identify the genes that are induced by OX40 signals, which contribute to the commitment of effector CD8 T cells onto the memory T cells by using a DNA microarray method. Although several interesting genes were identified as shown in Fig. 4, the function of these genes in the generation and maintenance of memory T cells is still unknown. Our next study will

therefore focus on the identification of the molecule(s) responsible for OX40-induced memory imprinting.

The deficiency of the $OX40^{-/-}$ donor T cells in survival and self-renewal may be owing to some abnormality in unidentified endogenous factors, because the circumstances for memory generation and maintenance in the recipient (such as the lymph node structure, $CD4^+$ T cells, APCs, stromal cells, and probably stromal cytokines, IL-7 and IL-15) were the same for wild-type and $OX40^{-/-}$ donor cells in our experimental setting. We examined the donor cell expression of receptors for the homeostatic cytokines IL-7 and IL-15, which are expressed by recipient cells, because these cytokines mediate the homeostatic proliferation of memory T cells. However, IL-7R and CD122 (the shared β subunit for IL-2 and IL-15 receptors) levels on the $KLRG1^{low}$population of $OX40^{-/-}$ $CD8^+$ T cells were similar to those on the $KLRG1^{low}$population of wild-type $CD8^+$ T cells (Figs. 1B, 2B, and data not shown). In addition, the in vitro culture of activated $OX40^{-/-}$ OT-I T cells showed a robust proliferative response to exogenous IL-2 (data not shown), suggesting that a lack of signaling molecules involved in the γc/JAK3/Stat-pathway may not cause their impaired survival and self-renewal, and indicating that defective IL-7 and IL-15 signals are probably not associated with the impaired generation and maintenance of $CD8^+$ T cells. We nevertheless found that $KLRG1^{low}$ long-lived T cells are the main producer of IL-2, and that the IL-2 production by $KLRG1^{low}$ MPECs and memory T cells that were generated in the absence of OX40 signals was severely impaired.

IL-2 is a well-known T-cell-derived cytokine, which also controls several T-cell responses including their activation, expansion, and activation-induced cell death, and the generation of functional memory $CD8^+$ T cells, in an autocrine or paracrine manner. IL-2 thus might be a key factor for the OX40-mediated survival of MPECs and maintenance of memory $CD8^+$ T cells. This scenario is partially supported by a recent report showing that IL-2 signals during priming imprint functional memory properties onto $CD8^+$ T cells, although the same paper also demonstrated that IL-2 is dispensable for the generation of long-lived $CD8^+$ T cells. Based on this scenario, the ability of memory precursor and memory $CD8^+$ T cells to produce IL-2 might be conferred on activated $CD8^+$ T cells by OX40 signals during Ag-priming. A precise understanding of OX40-mediated memory imprinting may provide us not only with important insights into the mechanisms of the development and homeostasis of memory T cells, but also with beneficial information for designing new vaccination strategies.

Conclusion

- OX40 signals are necessary for the optimal generation of $KLRG1^{low}CD8^+$ MPECs, in spite of their dispensability for the effector function of activated $CD8^+$ T cells.
- OX40 signals are essential for the generation of functional memory $CD8^+$ T cells.
- OX40 signals critically mediate the basal homeostatic proliferation of memory $CD8^+$ T cells, especially $KLRG1^{low}$memory $CD8^+$ T cells.
- OX40 signals are not essential during the memory phase for the self-renewal of memory $CD8^+$ T cells, which is programmed by previously provided OX40 signals.

Role of small RNA in regulation of bacterial multidrug resistance

Kunihiko Nishino

Laboratory of Microbiology and Infectious Diseases, Institute of Scientific and Industrial Research, Osaka University, 8-1 Mihogaoka, Ibaraki, Osaka 567-0047, Japan

Introduction

Multidrug efflux pumps cause serious problems in cancer chemotherapy and the treatment of bacterial infections. Bacterial drug resistance is often associated with multidrug efflux pumps, which can decrease drug accumulation within the cell. Bacterial multidrug efflux pumps are classified into five families on the basis of sequence similarity as major facilitator, resistance-nodulation-cell division (RND), small multidrug resistance, multidrug and toxic compound extrusion, and ATP-binding cassette. Of these, the RND family of efflux pumps plays major roles in both intrinsic and elevated resistance of Gram-negative bacteria to a wide range of compounds. RND efflux pumps require two other proteins to function, namely a membrane fusion protein and an outer membrane protein. The AcrAB efflux system, present in most Enterobacteriaceae, belongs to the RND family of efflux pumps and utilizes the outer membrane protein TolC. There are many putative and proven drug efflux pumps in the *Escherichia coli* genome. Since many such efflux pumps have overlapping substrate spectra, it is intriguing that bacteria, with their economically organized genomes, harbor such large sets of multidrug efflux genes.

Hfq is a well-conserved RNA binding protein that was originally identified in *E. coli* as a host factor required for the replication of Qβ bacteriophage. It functions in a hexameric ring-shaped structure as an RNA chaperone by mediating the binding of small RNAs (sRNAs) preferentially to single-stranded AU-rich regions of messenger RNA (mRNA) targets. sRNAs often bind to the 5′ untranslated leader region of cognate messengers to modulate their stability and/or translation. Since many transcriptional regulators are subject to post-transcriptional regulation mediated by sRNAs in conjunction with Hfq, an *hfq* mutant shows pleiotropic phenotypes. In recent years, Hfq has been established as an important virulence factor in bacterial pathogens. Although there is much evidence that Hfq is related to bacterial virulence, role of Hfq in bacterial multidrug resistance is yet to be defined. Here, we demonstrate that Hfq affects drug susceptibilities and accumulation in *E. coli* (1). In addition, we show that the AcrAB drug efflux system contributes to the Hfq-mediated drug resistance and that Hfq regulates the production of AcrB at the post-transcriptional level. Our data suggest that Hfq plays an important role in controlling AcrB level and thereby mediates drug resistance in *E. coli* (1).

The small RNA DsrA, first identified as a regulator of capsular polysaccharide synthesis, also regulates many pathogenicity factors, including genes involved in acid resistance and genes within the locus of enterocyte effacement (LEE). DsrA regulates target gene expression by antagonizing H-NS-mediated transcription inhibition and by stimulating synthesis of the RpoS σ factor. Despite study of key components of the DsrA regulatory network, the role of DsrA in drug resistance has remained elusive. In this study, we also report that DsrA controls the multidrug susceptibilities of *E. coli* by regulating the expression of the MdtEF drug efflux pump (2).

Materials and methods

Bacterial strains, plasmids, and growth conditions

Bacterial strains and plasmids used in this study are listed in Table 1. *E. coli* strains were derived from the wild-type strains W3104, MC4100, and MG1655. Bacterial strains were grown at 37°C in Luria-Bertani (LB) broth.

Construction of gene deletion mutants

To construct the *hfq* and *acrAB* deletion mutant from *E. coli* W3104 and MC4100 cells, the precise in-frame deletions were generated by crossover PCR. The following oligonucleotide primers were used: *hfq*-No (CGCGGATCCTAAAACTTTAACGGAACTGAC), *hfq*-Ni (CACGCAATAACCTTCACACTCCAAATTTATAACCATTCTCTCTTTTCCTTATATGCTTAT), *hfq*-Co (CGCGTCGACTGGGTCCAGCCACGCACCAGG), *hfq*-Ci (GTTATAAATTTGGAGTGTGAAGGTTATTGCGTGTAAGGTTTCGGGCTGTTTTTTTACACG), *acrA*-No (CGCGGATCCATTCGCATTTGTGGAATATAATCTCCATCA), *acrA*-Ni (CACGCAATAACCTTCACACTCCAAATTTATAACCATATGTAAACCTCGAGTGTCCG), *acrB*-Co (CGCGGATCCATGGAAAAAACTTACTGACCTGGAC), and *acrB*-Ci (GTTATAAATTTGGAGTGTGAAGGTTATTGCGTGTGATACAACGTGTAATCACTAAGGCC). The fragment containing the deletion was then cloned into the *Bam*HI-*Sal*I (for *hfq* deletion) or *Bam*HI sites (for *acrAB* deletion) (underlined in the primer sequences above) of the pKO3 vector, which is a gene replacement vector that contains a temperature-sensitive origin of replication and markers for positive and negative selection for chromosomal integration and excision. The deletion was introduced into the chromosome by use of the pKO3 gene-replacement protocol, as described previously. The plasmid obtained was electroporated into W3104 and MC4100. Cells were then recovered in 1 mL SOC (2% Bacto Tryptone, 0.5% yeast extract, 10 mM NaCl, 2.5 mM KCl, 10 mM $MgCl_2$, 20 mM glucose) for 1 h at 30°C. Cells were plated on chloramphenicol (20 mg/L)-containing LB agar plates and incubated at 43°C for overnight. From these plates, five colonies were picked up and inoculated into 1 mL of LB. After that, cells were plated at 30°C on 5% (w/v) sucrose plates. The outgrowing bacteria were plated on LB plates with or without chloramphenicol at 30°C. Chloramphenicol-susceptible mutants were selected. Chromosomal insertions and deletions were confirmed by PCR.

To construct the Δ*acrB*, Δ*tolC*, Δ*mdtEF*, and Δ*rpoS* mutants, gene disruption was performed as described by Datsenko and Wanner. The following oligonucleotide primers were used for the construction of the mutants: *acrB*-P1 (AAAAAGGCCGCTTACGCGGCCTTAGTGATTACACGTTGTAGTGTAGGCTGGAGCTGCTTC), *acrB*-P2 (GAACAGTCCAAGTCTTAACTTAAACAGGAGCCGTTAAGACCATATGAATATCCTCCTTAG), *tolC*-P1 (ACTGGTGCCGGGCTATCAGGCGCATAACCATCAGCAATAGGTGTAGGCTGGAGCTGCTTC), *tolC*-P2 (TTACAGTTTGATCGCGCTAAATACTGCTTCACCACAAGGACATATGAATATCCTCCTTAG), *mdtE*-P1 (TTAAAGAACCGTTATTTCTCAAGAATTTTCAGGGACTAAAGTGTAGGCTGGAGCTGCTTC), *mdtF*-P2 (AGGCTGAACCTTCATGTTCAACCTTACTCTCATTTACACGCATATGAATATCCTCCTTAG), *rpoS*-P1 (CCAGCCTCGCTTGAGACTGGCCTTTCTGACAGATGCTTACGTGTAGGCTGGAGCTGCTTC), and *rpoS*-P2 (TTGAATGTTCCGTCAAGGGATCACGGGTAGGAGCCACCTTCATATGAATATCCTCCTTAG). The chloramphenicol resistance *cat* gene or the kanamycin resistance *aph* gene, flanked by Flp recognition sites, was amplified by PCR with the primers listed above. The resulting PCR products were used to transform the recipient MG1655 strain harboring the plasmid pKD46, which expresses lambda Red recombinase. The chromosomal structure of the mutated loci was verified by PCR using the following primers: *acrB*-F (GTGACACTAATACCAGGATTGCTCTGAATA), *acrB*-R (CCAAACGCTATTTTAGTCCCGCAACAGGGC), *tolC*-F (GACGAAATCTATAAAGATCTAATGAAAAAA), *tolC*-R (GGAACGATGCGTGGCGTATGGATTTTGTCC), *mdtE*-F (TGATTTCATTACCCCCGGTGATTACTAAAG), *mdtF*-R (CTCTTCCCTGATGATTT

Table 1. *E. coli* strains and plasmids used in this study

Strain or Plasmid	Characteristics
Strains	
W3104	
MC4100	
NKE461	W3104Δ*hfq*
NKE19	W3104Δ*acrAB*
NKE451	W3104Δ*acrAB*Δ*hfq*
NKE610	MC4100Δ*hfq*
NKE596	MC4100Δ*acrAB*
NKE602	MC4100Δ*acrAB*Δ*hfq*
NKE621	MC4100/pNN387*acrAB*
NKE641	MC4100/pNN387*tolC*
NKE736	MC4100Δ*hfq*/pNN387*acrAB*
NKE1282	MC4100Δ*hfq*/pNN387*tolC*
MG1655	Wild-type
NKE96	Δ*acrB*
NKE154	Δ*acrB*/pHSG398
NKE197	Δ*acrB*/p*dsrA*
NKE128	Δ*acrB* Δ*tolC*
NKE160	Δ*acrB* Δ*tolC*/pHSG398
NKE202	Δ*acrB* Δ*tolC*/p*dsrA*
NKE139	Δ*acrB mdtEF*
NKE176	Δ*acrB mdtEF*/pHSG398
NKE207	Δ*acrB mdtEF*/p*dsrA*
NKE1372	Δ*acrB rpoS*
NKE1373	Δ*acrB rpoS*/pHSG398
NKE1374	Δ*acrB rpoS*/p*dsrA*
NKE1487	Δ*acrB hns*
Plasmids	
pKO3	*repA*(Ts) Cm^r $sacB^+$
pNN387	Cm^r; single-copy vector containing promoter less *lacZY*
pNN387*acrAB*	pNN387 (*acrAB* promoter - *lacZ*)
pNN387*tolC*	pNN387 (*tolC* promoter - *lacZ*)
pACYC177	Vector; Ap^r, Km^r
p*hfq*	0.5-kb HincII-PstI fragment containing *hfq* gene cloned into pACYC177, Km^r
pHSG398	Vector; Derivative of pUC18 containing Cmr in place of Ap^r
p*acrAB*	5.1-kb BamHI-SphI fragment containing *acrAB* genes cloned into pHSG398, CP^r
pKD46	Red recombinase expression plasmid, Ap^R
pKD3	$rep_{R6K\gamma[\rho]}Ap^RFRT\ Cm^RFRT$
pKD4	$rep_{R6K\gamma[\rho]}Ap^RFRT\ Km^RFRT$
pCP20	$rep_{pSC101}{}^{ts}\ Ap^R\ Cm^R\ cI857\lambda P_R flp$
pHSG398	$rep_{pMBI}\ Cm^R$
p*dsrA*	*dsrA* cloned into pHSG398, Cm^R

CTGCCGGGCTACC), *rpoS*-F (TGCGTATTGGTG ACGCTGGCAGCCTGCTTT), *rpoS*-R (GCCGCGT TGTTTATGCTGGTAACGCGCTGC), C-1 (TTATA CGCAAGGCGACAAGG), C-2 (GATCTTCCGTCA CAGGTAGG), K-1 (CAGTCATAGCCGAATAGCC T), and K-2 (CGGTGCCCTGAATGAACTGC). The *cat* or *aph* genes were eliminated by using plasmid pCP20, as previously described. To construct the Δ*hns* mutant, gene disruption was performed as previously described.

Plasmid construction

The *hfq* gene was amplified from W3104 genomic DNA by using primers CGCGTTAACATGTGTACAA TTGAGACGTAT and CGCCTGCAGGCGTATAAC CCTCTAAATAGA, which introduced *Hinc*II and *Pst*I sites (underlined in the primer sequences above). The PCR fragment contained a region from 85 bp upstream to 75 bp downstream of the *hfq* gene. The fragment was cleaved with *Hinc*II and *Pst*I, and then cloned into the corresponding sites of pACYC177, resulting in p*hfq* (Table 1). To produce p*acrAB*, the *acrAB* genes were amplified by using primers CGCGGATCCATGTTC GTGAATTTACAGGCG and CGCGCATGCAACGC GTCCCCTTCTTAGC, which introduced *Bam*HI and *Sph*I sites (underlined in the primer sequences above). This fragment contained a region from 140 bp upstream of *acrA* to 545 bp downstream of *acrB*. The fragment was cleaved with *Bam*HI and *Sph*I, and then cloned into the corresponding sites of pHSG398, resulting p*acrAB* (Table 1).

The *dsrA* gene was amplified from MG1655 genomic DNA using the primers *dsrA*-F_*Bam*HI (G CGGGATCCTATGGCGAATATTTTCTTGTC) and *dsrA*-R_*Sal*I (GCGGTCGACATTCATGACTTCAGC GTCTCT), which introduced *Bam*HI and *Sal*I sites at the ends of the amplified fragment. This PCR product was cloned between the *Bam*HI and *Sal*I sites of the vector pHSG398 (Takara Bio) to produce the plasmid p*dsrA*.

Determination of MIC for toxic compounds

The antibacterial activities of various agents were determined on LB agar (1% tryptone, 0.5% yeast extract, 0.5% NaCl) plates containing chloramphenicol, novobiocin, acriflavine, crystal violet, rhodamine 6G, benzalkonium, oxacillin, cefamandole, or nalidixic acid (Sigma, St. Louis, MO, USA) at various concentrations. Agar plates were made by the two-fold agar dilution technique, as described previously. To determine the minimum inhibitory concentrations (MICs), bacteria were grown in LB broth at 37°C overnight, diluted into the same medium, and then tested at a final inoculum size of 10^5 cfu/μL using a multipoint inoculator (Sakuma Seisakusyo, Tokyo, Japan) after incubation at 37°C for 20 h. The MIC was the lowest concentration of compound that inhibited cell growth.

Screening for positive regulators of drug resistance

Manipulation of DNA generally followed the standard practice. A genomic library was made by partial *Sau*3AI digestion of chromosomal DNA as follows. Chromosomal DNA prepared from an overnight culture of the wild-type strain MG1655 was digested with *Sau*3AI (1 U/μL) for 15, 20, 30, or 40 min. The digested DNA was separated on a 0.8% agarose gel, and fragments approximately 0.5–3.0 kb in size were purified and ligated into the *Bam*HI site of vector pHSG398 (Takara Bio, Japan). Ligation products were transformed into *E. coli* DH5α, selecting for chloramphenicol-resistant transformants. Plasmid DNA was prepared from a pool of 16,000 transformants and used to transform the *acrB* deletion strain NKE96. Cells were plated on LB agar medium containing 15 mg/L chloramphenicol and 2 mg/L oxacillin. After then, LB agar plates were incubated at 37°C for overnight to select drug-resistant transformants.

Observation of drug accumulation in E. coli cells

E. coli cells were spotted onto LB agar plates containing rhodamine 6G (0.5 or 1 mg/L) at a final inoculum size of 10^5 CFU/spot, using a multipoint inoculator (Sakuma Seisakusyo), and were incubated at 37°C for 20 h. Drug accumulation in *E. coli* cells was observed as the staining of cells with rhodamine 6G by

using a scanner (K100D super; Pentax, Tokyo, Japan).

Reporter gene assay

To investigate the transcription of *acrAB* and *tolC*, the promoter regions of these genes were cloned in front of the *lacZ* reporter gene in a single-copy pNN387 vector. The resulting plasmids were transformed into the MC4100 strain for ß-galactosidase activity measurements. Then, transformants were grown at 37°C in LB broth containing 15 mg/L chloramphenicol until the optical density at 600 nm reached 0.6. ß-galactosidase activity in cell lysates that was assayed using *o*-nitrophenyl-ß-D-galactopyranoside as a substrate, as described by Miller, with a slight modification.

Detection of AcrB

AcrB production was determined as follows. *E. coli* cells were grown in LB broth until the optical density at 600 nm reached 0.6. The cells were harvested, washed twice with 50 mM potassium phosphate buffer (pH 7.0), and then disrupted by sonication with Branson Sonifier 250D (Branson Ultrasonics Corp., CT, USA) for 1.5 min. After undisrupted cells were removed by low-speed centrifugation (10,000 $\times g$, 10 min), membrane fraction was collected by ultracentrifugation (200,000 $\times g$, 30 min). Membrane was then resuspended in 50 mM potassium phosphate buffer (pH 7.0). Cell membrane fractions were standardized to 15 μg of protein and were then separated by sodium dodecyl sulfate-polyacrylamide gel electrophoresis on an 8% polyacrylamide gel, followed by electroblotting onto a polyvinylidene difluoride membrane. The AcrB protein was detected with polyclonal anti-AcrB antibodies, alkaline phosphatase-conjugated goat anti-rabbit immunoglobulin G (Bio-Rad Laboratories, CA, USA), and the CDP-Star reagent (GE Healthcare, Tokyo, Japan), as described previously. Production of AcrB was scanned by LAS-3000 (Fujifilm, Tokyo, Japan) and quantified by Science Lab 2001 Image Gauge Ver. 4.0 software (Fujifilm, Tokyo, Japan).

RNA extraction and determination of specific transcript levels by quantitative real-time PCR following reverse transcription

Bacterial strains NKE154, NKE197, NKE1373, NKE1374, NKE96, and NKE1487 were grown at 30°C in LB broth. Cells were collected for total RNA extraction when the cultures reached an optical density of 0.6 at 600nm. Total RNA was isolated from bacterial cultures using an RNeasy Protect Bacteria Mini Kit (Qiagen) and RNase-Free DNase (Qiagen), according to the manufacturer's instructions. The absence of genomic DNA from DNase-treated RNA samples was confirmed by both nondenaturing agarose electrophoresis gels and PCR with primers known to target genomic DNA. RNA concentration was determined spectrophotometrically. Bulk cDNA samples were synthesized from total RNA using TaqMan Reverse Transcription Reagents (PE Applied Biosystems) and random hexamers, according to the manufacturer's instructions. Specific primer pairs were designed using ABI PRISM Primer Express software (PE Applied Biosystems), as previously described. *rrlA* of 23S rRNA and *rrsA* of 16S rRNA were chosen as normalizing genes. Real-time PCR was performed with each specific primer pair using SYBR Green PCR Master Mix (PE Applied Biosystems). Reactions were carried out using an ABI PRISM 7000 Sequence Detection System (PE Applied Biosystems); the fluorescence signal due to SYBR Green intercalation was monitored to quantify the double-stranded DNA product formed in each PCR cycle.

Results and discussion

To investigate the role of Hfq in drug susceptibilities, the *hfq* gene was deleted from *E. coli* strains W3104 and MC4100, as described in Materials and methods. In both backgrounds, *hfq* mutants were sensitive to chloramphenicol (4-fold), novobiocin (4-fold), acriflavine (8-fold), crystal violet (4-fold), rhodamine 6G (>4-fold), benzalkonium (8-fold), oxacillin (4-fold), cefamandole (4-fold), and nalidixic acid (4-fold), compared with the parental strains (Table 2). In both

Table 2. Susceptibility of *E. coli* strains to toxic compounds

Strain	MIC (μg/ml)								
	CHL	NOV	ACR	CV	R6G	BENZ	OXA	FAM	NAL
W3104	4	128	256	32	>512	64	256	0.5	4
W3104Δ*hfq*	**1**	**32**	**32**	**8**	**128**	**8**	**64**	**0.13**	**1**
W3104Δ*hfq*/ pACYC177	1	32	32	8	128	8	N.D.	N.D.	1
W3104Δ*hfq*/ p*hfq*	4	128	256	32	>512	64	N.D.	N.D.	4
W3104Δ*acrAB*	0.5	2	8	1	2	4	1	0.063	1
W3104Δ*acrAB*/ pHSG398	N.D.	2	8	1	2	4	1	0.063	1
W3104Δ*acrAB*/ p*acrAB*	N.D.	128	256	32	>512	64	256	0.5	4
W3104Δ*acrAB*Δ*hfq*	0.5	**1**	8	1	2	4	1	0.063	1
W3104Δ*acrAB*Δ*hfq*/ pHSG398+ pACYC177	N.D.	1	8	1	2	4	N.D.	N.D.	1
W3104Δ*acrAB*Δ*hfq*/ p*acrAB*+p*hfq*	N.D.	128	256	32	>512	64	N.D.	N.D.	4
MC4100	4	128	256	64	>512	64	256	0.5	4
MC4100Δ*hfq*	**1**	**32**	**32**	**8**	**128**	**8**	**64**	**0.13**	**1**
MC4100Δ*hfq*/ pACYC177	1	32	32	8	128	8	N.D.	N.D.	1
MC4100Δ*hfq*/ p*hfq*	4	128	256	64	>512	64	N.D.	N.D.	4
MC4100Δ*acrAB*	0.5	2	8	1	2	4	1	0.063	1
MC4100Δ*acrAB*/ pHSG398	N.D.	2	8	1	2	4	1	0.063	1
MC4100Δ*acrAB*/ p*acrAB*	N.D.	128	256	64	>512	64	256	0.5	4
MC4100Δ*acrAB*Δ*hfq*	0.5	**1**	8	1	2	4	1	0.063	1
MC4100Δ*acrAB*Δ*hfq*/ pHSG398+ pACYC177	N.D.	1	8	1	2	4	N.D.	N.D.	1
MC4100Δ*acrAB*Δ*hfq*/ p*acrAB*+p*hfq*	N.D.	128	256	64	>512	64	N.D.	N.D.	4

CHL, chloramphenicol; NOV, novobiocin; ACR, acriflavine; CV, crystal violet; R6G, rhodamine 6G; BENZ, benzalkonium; OXA, oxacillin; FAM, cefamandole; NAL, nalidixic acid.

Values in boldface are smaller than those of a corresponding parental strains.

MIC determinations were repeated at least three times.

N.D., not determined because vectors have chloramphenicol or ampicillin resistance cassette.

W3104 and MC4100, Δ*hfq* strains complemented with p*hfq* behaved like the wild type. These data indicate that Hfq affects the intrinsic multidrug resistance of *E. coli*.

One of the major mechanisms of bacterial multidrug resistance is active drug efflux. Enhanced drug efflux activity reduces intracellular drug accumulation. Therefore, we investigated the effect of Hfq on drug accumulation in *E. coli* cells. *E. coli* W3104, W3104Δ*hfq* and W3104Δ*acrAB* cells were spotted onto agar plates containing 0.5 or 1 mg of rhodamine 6G/L, and the plates were then incubated at 37°C for 20 h. Rhodamine 6G did not inhibit cell growth at these concentrations (Figure 1), however a difference in the color of cells was observed between these strains. The W3104Δ*hfq* and W3104Δ*acrAB* strains appeared red on plates containing rhodamine 6G, whereas the W3104 strain was white. This result indicates greater drug accumulation in the W3104Δ*hfq* and W3104Δ*acrAB* strains, suggesting decreased drug efflux activities in these strains compared to the wild-type strain (Figure 1). Identical difference in rhodamine 6G accumulation between MC4100 and MC4100Δ*hfq* was also observed (data not shown).

The results described above indicate that the drug efflux activity of *E. coli* may be impaired by *hfq* deletion. In a previous study, we revealed that at least 20 intrinsic drug efflux systems are encoded in the *E. coli* chromosome. Among these, the AcrAB efflux system plays major roles in both intrinsic and elevated resistance of *E. coli* to a wide range of noxious compounds. In order to determine whether the AcrAB multidrug efflux system contributes to Hfq-regulated drug resistance level of *E. coli*, we investigated the effect of *hfq* deletion on the drug susceptibilities of the *acrAB* deletion mutant (Table 2). The *hfq* deletion did not affect the drug susceptibilities of W3104Δ*acrAB* or MC4100Δ*acrAB* against chloramphenicol, acriflavine, crystal violet, rhodamine 6G, benzalkonium, oxacillin, cefamandole, or nalidixic acid, whereas it results in increased drug susceptibilities in W3104 and MC4100 (Table 2). When the Δ*acrAB*Δ*hfq* strains were transformed with p*acrAB* and p*hfq*, the transformants behaved like the wild type (Table 2). These results indicate that the AcrAB efflux system contributes to the Hfq-controlled drug resistance in *E. coli*.

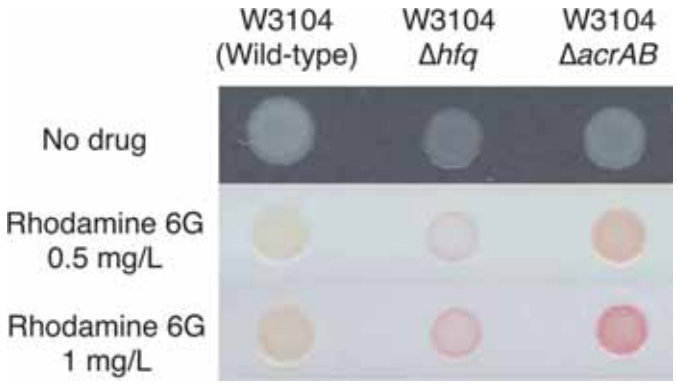

Fig. 1. Hfq affects drug accumulation in *E. coli* (1). Strains W3104 (wild-type), NKE461 (W3104Δ*hfq*) and NKE19 (W3104Δ*acrAB*) were spotted onto LB agar plates containing rhodamine 6G 0.5 or 1 mg/L. After incubation at 37°C for 20 h, *E. coli* colonies were observed under visible white light (1).

The results above suggest the possibility that the AcrAB efflux system is regulated by Hfq. To determine whether Hfq affects AcrAB expression on the transcriptional level, the promoter region of the *acrAB* operon was cloned in front of the *lacZ* reporter gene in a single-copy pNN387 vector, and the promoter activity was determined as ß-galactosidase activity. The promoter activity of the *tolC* outer membrane channel was also measured. As shown in Figure 2, there are no significant changes in the promoter activities of *acrAB* and *tolC* in MC4100Δ*hfq* compared to those in MC4100. Thus, Hfq does not affect *acrAB* and *tolC* transcription.

To test whether Hfq affects AcrB production, we examined the production level of the AcrB protein in MC4100 and MC4100Δ*hfq* using western blot analysis. As shown in Figure 3, production level of AcrB in MC4100Δ*hfq* was lower than that in MC4100. Quantification with Image Gauge software (Fujifilm, Tokyo, Japan) identified that the production of AcrB in the *hfq* mutant is 53% compared to that in the MC4100 strain. These data indicate that Hfq affects AcrB expression on the post-transcriptional level.

In this study, we found that Hfq acts as a regulator of drug resistance in *E. coli* (1). Hfq positively regulates the production of the AcrB drug efflux protein; thus, deletion of the *hfq* gene resulted in the decreased

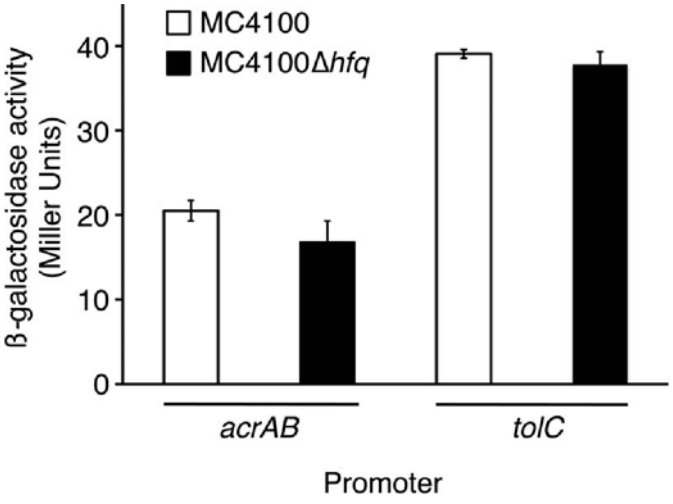

Fig. 2. Effect of Hfq on the promoter activity of the AcrAB-TolC drug efflux system (1). Effect of *hfq* deletion on the promoter activities of the *acrAB* operon and the *tolC* gene were determined using strains NKE621, NKE736, NKE641, and NKE1282 as described in Materials and methods (1). The data correspond to mean values of three independent experiments. Error bars correspond to the standard deviation.

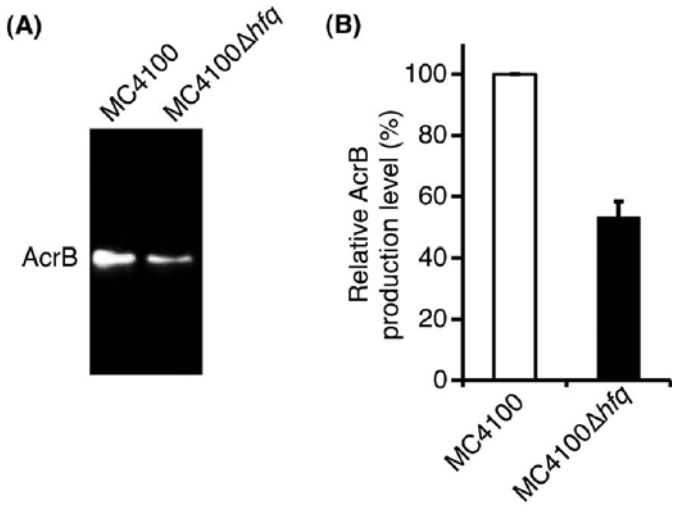

Fig. 3. Hfq affects the production level of the AcrB multidrug efflux protein (1). (A) Cell membrane fractions were prepared from the strains MC4100 and NKE610 (MC4100Δ*hfq*) then standardized to 15 μg of protein. The production of AcrB was detected by western blotting using polyclonal anti-AcrB antibodies, as described in Materials and methods. (B) The relative amount of AcrB production was calculated by western blotting analysis using Science Lab 2001 Image Gauge Ver. 4.0 software. The data correspond to mean values of three independent experiments. Error bars correspond to the standard deviation.

production of AcrB, and the *hfq* mutant became more susceptible to multiple drugs compared to the wild-type strain. Hfq affects the protein level of AcrB; however, it does not change the promoter activity of the *acrAB* operon, indicating that Hfq controls AcrB at the post-transcriptional level. The bacterial Sm-like protein Hfq facilitates RNA-RNA interaction involved in post-transcriptional regulation of the stress response. Specifically, Hfq helps pair noncoding RNAs (ncRNAs) with complementary regions of target mRNAs. *E. coli* Hfq mutants show disrupted signaling in stress response pathways arising from the need for Hfq to mediate base-pairing between regulatory ncRNAs and their mRNA targets. Examples of these partnerships include DsrA-*rpoS,* OxyS-*fhlA,* OxyS-*rpoS,* RprA-*rpoS,* RyhB-*sodB,* and Spot42-*gal*ETKM.

We considered the possibility that overproduction of Hfq from the expression vector may enhance the drug resistance level of *E. coli*; however, it was not observed (data not shown). This is probably because the Hfq protein is constitutively expressed (55,000 molecules/cell) and it is enough to maintain the intrinsic drug resistance of *E. coli* cells. In addition to the roles of Hfq in bacterial virulence, we found a previously uncharacterized Hfq role in multidrug resistance based on regulating the AcrB drug efflux system. However, the results still leave open the possibility that Hfq may also influence multidrug resistance by regulation of systems in addition to AcrAB, such as other efflux systems and/or outer membrane channels, because Hfq has been shown to affect membrane composition particularly the outer membrane proteins.

Expression of multidrug efflux genes is often regulated in a complex manner, as described above. Therefore, we screened the genomic library of *E. coli* for genes that decreased drug susceptibility in this organism. We screened a host strain lacking a functional *acrB* gene in order to identify regulatory elements involved in the expression of other multidrug

Table 3. Susceptibility of *Escherichia coli* strains to toxic compounds

Strain	MIC (mg/L)				
	OXA	CLOX	ERM	R6G	NOV
WT	256	>512	128	>512	256
Δ*acrB*	0.5	1	4	2	2
Δ*acrB*/vector	0.5	1	4	2	2
Δ*acrB*/p*dsrA*	**4**	**4**	**16**	**16**	**8**
Δ*acrB tolC*	0.5	0.25	2	2	0.5
Δ*acrB tolC*/vector	0.5	0.25	2	2	0.5
Δ*acrB tolC*/p*dsrA*	0.5	0.25	2	2	0.5
Δ*acrB mdtEF*	0.5	1	4	2	2
Δ*acrB mdtEF*/vector	0.5	1	4	2	2
Δ*acrB mdtEF*/p*dsrA*	0.5	1	4	2	2
Δ*acrB rpoS*	0.5	1	4	2	2
Δ*acrB rpoS*/vector	0.5	1	4	2	2
Δ*acrB rpoS*/p*dsrA*	0.5	1	4	2	2
Δ*acrB hns*	128	128	32	256	128

OXA, oxacillin; CLOX, cloxacillin; ERM, erythromycin; R6G, rhodamine 6G; NOV, novobiocin.

Values in boldface are larger than those of a corresponding parental strain haboring the pHSG398 vector.

MIC determinations were repeated at least three times.

resistance systems. The library was developed from the chromosomal DNA of the MG1655 strain, and recombinant plasmids were then transformed into the Δ*acrB* strain NKE96. In one experiment, we found an eight-fold increase in oxacillin MIC over the transformant (data not shown). Introduction of the plasmid isolated from this strain into fresh Δ*acrB* cells resulted in the same oxacillin resistance phenotype; the MIC increased eight-fold over the recipient strain (data not shown).

Sequencing of the plasmid revealed an insertion containing the complete coding sequence of *dsrA* and a partial coding sequence of *yedP*. This suggests that in cells carrying this plasmid, overexpressed DsrA caused the transcriptional activation of genes involved in oxacillin susceptibility. Full-length wild-type *dsrA* was cloned in the pHSG398 vector to obtain p*dsrA* (Table 1). Oxacillin MIC for NKE96 cells harboring p*dsrA* was eight times higher (4.0 vs. 0.5 mg/L) than for cells harboring the pHSG398 vector (Table 3). This suggests that the DsrA produced by this plasmid decreased oxacillin susceptibility of *E. coli*. During screening, we also yielded the activators known to be involved in regulation of multidrug efflux pump genes, such as BaeR, EvgA, GadX, NlpE, and YdeO. We investigated the effect of *dsrA* overexpression on the susceptibility of *E. coli* to other toxic compounds. Various drugs were tested, including common substrates of multidrug efflux pumps, and we found that *dsrA* overexpression decreased the susceptibilities of the NKE96 strain to cloxacillin, erythromycin, rhodamine 6G, and novobiocin (Table 3). These results indicate that overexpression of DsrA induces multidrug resistance in *E. coli*.

A major mechanism of bacterial multidrug resistance is active drug efflux. Therefore, we investigated drug efflux activity in the *dsrA*-overexpressed strain, as previously described. NKE154 (Δ*acrB*/vector) and NKE197 (Δ*acrB*/p*dsrA*) cells were spotted on agar plates containing 1 mg/L of ethidium bromide, and plates were then incubated for 18 h. Accumulation of ethidium bromide in *E. coli* cells was observed from

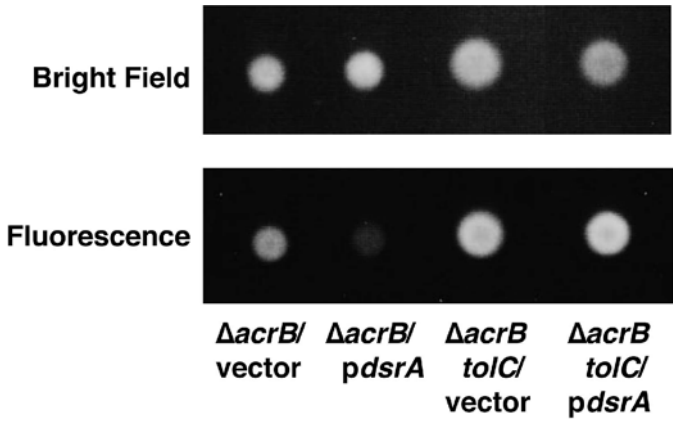

Fig. 4. Effect of *dsrA* overexpression on drug accumulation in *Escherichia coli* cells (2). Strains NKE154 (Δ*acrB*/vector), NKE197 (Δ*acrB*/p*dsrA*), NKE160 (Δ*acrB tolC*/vector), and NKE202 (Δ*acrB tolC*/p*dsrA*) were spotted on LB agar plates containing 1 mg/L of ethidium bromide at a final inoculum size of 10^5 CFU/spot. After incubation, *E. coli* colonies were observed under visible white light (bright field) and UV light (fluorescence) by use of an Electronic U.V. Transilluminator FAS-II (Toyobo, Osaka, Japan).

fluorescence of this compound under UV light (Fig. 1). As shown in Fig. 4, *dsrA* overexpression resulted in a drastic decrease in fluorescence despite the normal growth of NKE197 on the agar plate. The results show active efflux of ethidium bromide from NKE197 cells.

The results described above indicate that the expression of a multidrug efflux pump may be induced by *dsrA* overexpression. To determine whether the decreased multidrug susceptibilities mediated by DsrA also depend on the TolC-dependent drug efflux pump(s), we investigated the effect of *tolC* deletion on drug susceptibilities in cells overexpressing *dsrA*. The deletion was performed using the lambda Red system. Deletion of *tolC* from the strain Δ*acrB* increased susceptibility to cloxacillin and novobiocin (Table 3), which is in accordance with a previous reported study. The *tolC* deletion completely inhibited the decreased multidrug susceptibilities mediated by DsrA (Table 3) and also restored the accumulation of ethidium bromide in the *dsrA*-overexpressing strain (Fig. 4). These results indicate that the decreased multidrug susceptibilities mediated by DsrA can be attributed to an increase in the functioning of a TolC-dependent drug efflux pump.

To determine the drug efflux pump that shows increased expression when *dsrA* is overexpressed, we used qRT-PCR to investigate changes in the levels of drug efflux gene mRNAs dependent on *dsrA* overexpression. Expression changes of 20 drug efflux pump genes and *tolC* were measured and we found that expression of *mdtE* was significantly increased by *dsrA* overexpression (Fig. 5).

To determine whether the decreased multidrug susceptibilities mediated by *dsrA* overexpression is because of increased expression of *mdtEF*, we investigated the effects of deleting these genes (Table 3). In strain Δ*acrB mdtEF*, overexpression of *dsrA* did not change drug susceptibilities (Table 3), whereas it decreased multidrug susceptibilities of strain Δ*acrB*. Thus, these data indicate that the decreased multidrug susceptibilities mediated by DsrA is because of increased expression of the *mdtEF* multidrug efflux genes.

Because it has been reported that *mdtE* is RpoS-regulated and that DsrA regulates target gene expression by stimulating synthesis of RpoS, we constructed the *rpoS*-deleted mutant to investigate the effect of RpoS on the decreased multidrug susceptibilities and increased expression of *mdtE* modulated by DsrA. In the Δ*acrB rpoS* mutant overexpression of *dsrA* did not change the drug susceptibilities, whereas it decreased susceptibilities of the Δ*acrB* mutant (Table 3). When the expression level of *mdtE* in NKE1373 and NKE1374 was measured by qRT-PCR, there was no significant change in *mdtE* expression (1.6 ± 0.20 fold increase attributed to *dsrA* overexpression). These data indicate that DsrA affects drug susceptibilities via RpoS. Because it was also reported that DsrA binds *hns* mRNA by specific base-pairing interactions and blocks H-NS translation, we investigated the effect of *hns* deletion on drug susceptibilities of the Δ*acrB* strain (Table 3). The *hns* deletion decreased multidrug susceptibilities of the Δ*acrB* strain. This is in agreement with the results of a previous study. The effect of the *hns* deletion on the drug susceptibilities of the Δ*acrB* strain is larger than that of *dsrA* overexpression (Table 3). This difference is probably due to the increased expression of *acrEF*

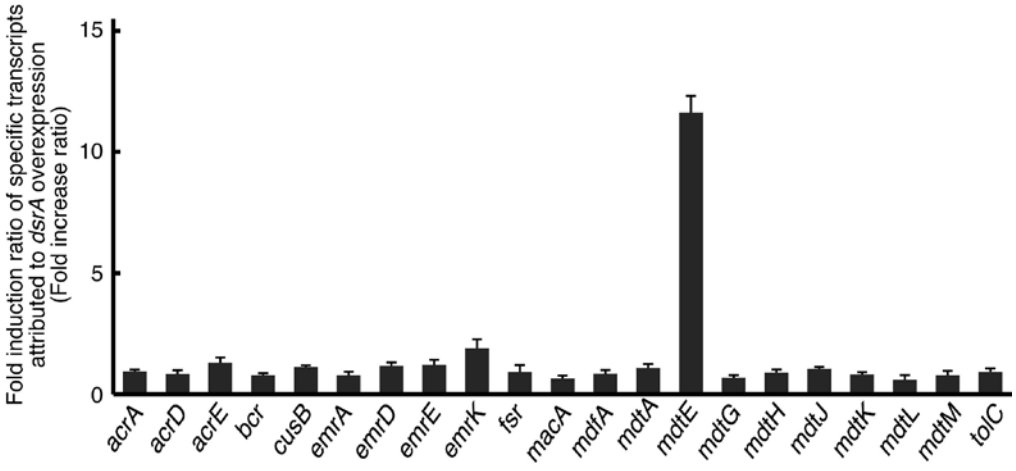

Fig. 5. Effect of DsrA on expression levels of drug efflux and outer membrane channel genes (2). The level of mRNA transcript was determined by qRT-PCR. The fold change ratio was calculated by dividing the expression level of the gene in strain NKE197 by that in strain NKE154. Experiments were performed in three biological replicates and data correspond to mean values. Error bars represent the standard deviation.

and *mdtEF* in the Δ*acrB hns* strain as we previously reported. Indeed, expression levels of *acrE* and *mdtE* in the Δ*acrB hns* strain are significantly higher than those in the Δ*acrB* strain (68 ± 3.5 and 65 ± 4.5 fold increase, respectively). Effect of *hns* deletion on the expression of *acrE* was much larger than that of *dsrA* overexpression. This suggests the possibility that overexpression of *dsrA* is not enough to derepress the *acrEF* because it is strongly repressed by H-NS. Taken together, these results indicate that effect of *dsrA* overexpression on *mdtEF* is mainly dependent on the RpoS pathway.

In this study, we performed a genome-wide search for a regulator of multidrug efflux in *E. coli* by random shotgun cloning. We found that DsrA decreases susceptibility to oxacillin, cloxacillin, erythromycin, rhodamine 6G, and novobiocin by upregulating *mdtEF*. It was previously reported that DsrA is a regulator of capsular polysaccharide synthesis and many pathogenicity factors, including acid resistance genes and genes within the LEE. In this study, it was determined that DsrA modulates multidrug susceptibilities through activation of genes encoding the MdtEF multidrug efflux pump in *E. coli*. Further investigation of the regulation of multidrug efflux systems in several natural environments such as those within hosts is needed to elucidate the biological significance of their regulatory networks.

Conclusions

Our results indicate that Hfq regulates the drug efflux system at the post-transcriptional level and reveals the previously uncharacterized role of Hfq in bacterial multidrug resistance. Furthermore, we found that DsrA modulates multidrug efflux through activation of genes encoding the MdtEF pump in *E. coli*.

Acknowledgments

This work was supported by the the Waksman Foundation of Japan Inc.

References

(1) Yamada, J., S. Yamasaki, H. Hirakawa, M. Hayashi-Nishino, A. Yamaguchi, and K. Nishino. (2010) Impact of RNA chaperone Hfq on multidrug resistance in *Escherichia coli*. *J. Antimicrob. Chemother.* **65**, 853-858.
(2) Nishino, K., S. Yamasaki, M. Hayashi-Nishino,

and A. Yamaguchi. (2011) Effect of overexpression of small non-coding DsrA RNA on multidrug efflux in *Escherichia coli*. *J. Antimicrob. Chemother.* **66**, 291-296.

Aberrant differentiation of dendritic cells in malaria infection

Tomohiko Tamura, Motohide Ichino

Department of Immunology, Yokohama City University Graduate School of Medicine, 3-9 Fukuura, Kanazawa-ku, Yokohama, Kanagawa 236-0004, JAPAN

Introduction

Infection with malaria parasites has long been known to be persistent and associated with suppressed immune responses to the parasite and to unrelated antigens. *Plasmodium* is a parasite well-adapted to its hosts, and its infection causes malaria, a serious cause of morbidity and mortality in millions of individuals each year. The parasite is able to evade the host immune response by antigenic diversity, clonal antigenic variation, and T cell antagonism. In addition to these evasion mechanisms, it has been indicated that malaria-induced immune suppression is associated with a higher incidence of other infectious diseases. Furthermore, malaria infections are associated with reduced immune responses to vaccination. Impaired cell-mediated immunity and altered macrophage responses in patients with acute blood-stage malaria infections have been reported (reviewed in (1)).

Dendritic cells (DCs) are the most powerful antigen-presenting cells that play a pivotal role in both innate and adaptive immune responses. Immature DCs in the periphery uptake antigens and migrate to lymphoid tissues to initiate immune responses. By increasing their surface expression of major histocompatibility complex (MHC) molecules and costimulatory molecules, DCs process antigens and mature to present antigen epitopes to T cells (reviewed in (2)). It has been reported that several pathogens suppress host immune responses by interfering with the maturation and migration of DCs. In particular, *Plasmodium falciparum*-infected erythrocytes modulate the maturation of DCs and their capacity to activate T cells *in vitro*, suggesting a role for DCs in malaria-induced immune suppression (3). Using a malaria mouse model, we and others previously found that upon *P. berghei* infection the splenic DCs showed reduced presenting ability of soluble ovalbumin (OVA) to OT-I T as well as OT-II T cells (4)(5).

Four DC subsets have been identified in the mouse spleen (2). Conventional $CD11c^{high}$ DCs (cDCs) are divided into 3 subsets: $CD4^+$ $CD8\alpha^-$ $CD11b^{high}$ DCs ($CD4^+$ DCs), $CD4^-$ $CD8\alpha^+$ $CD11b^{low}$ DCs ($CD8\alpha^+$ DCs), and $CD4^-$ $CD8\alpha^-$ $CD11b^{high}$ DCs (double negative (DN) DCs). The spleen also contains $CD11c^{int}$ $B220^+$ $CD11b^-$ plasmacytoid DCs (PDCs), which can produce large amounts of type I interferons. We have shown that structurally related, hematopoietic-specific transcription factors Interferon Regulatory Factor-8 (IRF8) and IRF4 are differentially expressed in DC subsets (6). $CD8\alpha^+$ DCs and PDCs express high levels of IRF8, but low to no IRF4. Conversely, IRF4 expression is high in $CD4^+$ DCs and DN DCs whereas IRF8 expression is low. Analysis of IRF8/IRF4 single knock-out and double knock-out mice revealed that the above pattern of IRF8/IRF4 expression correlates with their requirement for DC subset development (6). Thus, IRF4 and IRF8 are the essential transcription factors that direct the generation of multiple DC subsets and their functional diversity.

In this study, by using a mouse model of malaria parasite infection, we found that malaria impairs the development of DC subsets *in vivo* and *in vitro*, rather than simply the maturation of DCs. Furthermore, we demonstrate that the expression of IRF4 and

IRF8 is severely impaired by malaria. This raises the possibility that *Plasmodium* targets the transcription factors critical for the development and function of DCs in early stages of DC differentiation to suppress host's immune responses.

Materials and Methods

Parasites and mice

Blood-stage of malaria parasite, *Plasmodium berghei* ANKA, was maintained in C57BL/6 mice (B6 mice). pRBC were collected from infected mice by orbital puncture. Female B6 mice (haplotype H-2^b) were purchased from CLEA Japan Inc. (Tokyo, Japan). Both OT-I and OT-II transgenic C57BL/6 mice (OT-I mice and OT-II mice, respectively) were bred in specific pathogen-free conditions in the animal facilities at the Yokohama City University School of Medicine (Yokohama, Japan). OT-I mice possess naive CD8α^+ T cells expressing T cell receptors (TCR) specific for OVA and OT-II mice possess naive CD4$^+$ T cells expressing TCR specific for OVA. Six-to-eight-week-old mice were used for the study. All mice were maintained according to institutional guidelines under approved protocols in the Institute of Laboratory Animal Science (Yokohama City University School of Medicine). Heparinized blood from *P. berghei*-infected mice was collected to enrich pRBC containing ring forms, schizonts and trophozoites. Passage of blood through a CF11 cellulose column (Whatman, Maidstone, England) removed white cells from parasitized blood. The blood was layered onto 65% Percoll (GE Healthcare, Uppsala, Sweden) and centrifuged at 400 *g* at 4°C. pRBC at the interphase were removed and preparations of >80% pRBC were obtained. The cells passing through the CF11 cellulose column from uninfected mice were used as uninfected RBC.

Administration of infected erythrocytes

pRBC were obtained from *P. berghei*-infected B6 mice with >5% parasitemia by orbital puncture. To induce blood-stage infection, 1×10^6 pRBC in phosphate-buffered saline (PBS) in a total volume of 0.2 mL were injected intraperitoneally into each B6 mouse. Parasitemia was monitored by thin blood smears stained with Giemsa solution (Merck, Darmstadt, Germany).

Cell preparation and culture

CD11c$^+$ DCs from spleens were prepared as previously described (6). Briefly, the spleens of 1-5 mice were incubated in PBS containing 1.67 Wünsch U/mL Liberase DL (Roche Diagnostics GmbH, Mannheim, Germany) and 50 μg/mL DNase I (Roche) at 37°C for 30 min. Undigested material was removed by filtration and RBC were lysed with 0.83 M ammonium chloride tris (hydroxymethyl) aminomethane buffer. Culture medium was RPMI1640 (Gibco BRL, Rockville, MD) supplemented with 10% fetal calf serum (FCS), 200 U/mL penicillin (Banyu Pharmaceutical, Tokyo, Japan), 200 μg/mL streptomycin sulphate (Meiji Seika, Tokyo, Japan), 2 mM L-glutamine (Wako Pure Chemical Industries, Osaka, Japan), and 10 mM *N*-2-hydroxyethylpiperazine-*N*'-2-ethanesulphonic acid (HEPES; Dojindo Laboratories, Kumamoto, Japan). Cells were washed once with RPMI1640 medium and the cells were resuspended in running buffer for autoMACS (Miltenyi Biotec, Auburn, CA). Mononuclear cells from the spleens were incubated with anti-mouse CD11c magnetic beads (Miltenyi Biotec) and then subjected to selection by autoMACS. Cells selected based on CD11c expression routinely demonstrated >90% viable CD11c$^+$ DCs. The cells examined were all prepared from mice 5 days after infection with 1×10^6 pRBC unless otherwise stated. Bone marrow cells were collected from the tibia and femur of uninfected mice and cultured in the presence of recombinant human Flt3 ligand (Flt3L) (Invitrogen, Tokyo, Japan) for 8 days. In some cases, pRBC or uninfected RBC were added to the culture (1:50 DC to erythrocytes ratio).

Monoclonal antibodies (mAb) and flow cytometry

Spleen cells were analyzed as previously described (6) with the following antibodies: fluorescein

isothiocyanate (FITC)-conjugated anti-CD11c, biotin-conjugated anti-CD11c (HL3; BD Biosciences, San Diego, CA), allophycocyanin (APC)-conjugated anti-CD11c (N418; BioLegend, San Diego, CA), phycoerythrin (PE)-conjugated anti-CD4 (RM4-5; BioLegend), allophycocyanin with cyanin-7 (APC-Cy7)-conjugated anti-CD8α (53-6.7; BioLegend), phycoerythrin with cyanin-7 (PE-Cy7)-conjugated anti-I-Ab (AF6-120.1; BioLegend), PE anti-I-Ab (AF6-120.1; BioLegend), PE anti-B220 (RA3-6B2; BioLegend), APC-Cy7 anti-CD11b (M1/70; BioLegend), PE-Cy7 anti-CD24 (M1/69; BioLegend), APC anti-PDCA-1 (927; BioLegend), FITC anti-PDCA-1 (927; BioLegend), PE anti-CD40 (1C10; BioLegend), PE anti-CD80 (16-10A1; BioLegend), and FITC anti-CD86 (GL1; eBioscience, San Diego, CA). Anti-CD16/CD32 (Fc III/II receptor, 2.4G2; BioLegend) was used to prevent the antibodies from binding Fc receptors. For detection of intracellular IRF4 and IRF8, surface marker stained cells were fixed with 2% paraformaldehyde in PBS, permeabilized with 0.5% saponin (Sigma-Aldrich, Tokyo, Japan), blocked with 5% normal donkey serum and stained with goat anti-IRF4 (M-17), anti-IRF8 (C-19) Ab (Santa Cruz Biotechnology, Santa Cruz, CA), or control normal goat IgG, followed by incubation with FITC-conjugated donkey anti-goat Ab (Jackson ImmunoResearch Laboratories, West Grove, PA). Fluorescence staining was analyzed with a FACSCanto II flow cytometer (BD Biosciences) and data were analyzed using FlowJo Software (TreeStar, Ashland, OR).

Results

The aberrant profile of splenic DC populations in P. berghei-infected in mice

We first examined the subset profiles and the maturation status of *in vivo* CD11c$^+$ DCs of *P. berghei*-infected mice. *P. berghei* ANKA is a lethal strain and infected B6 mice die within 10 days after infection. Splenic CD11c$^+$ DCs were purified from the mice on days from 3–6 after infection with pRBC or from the mice cohort on the same days. Flow cytometric analysis revealed that DC subset profiles of infected mice are distinct from those of uninfected mice (Fig.1). The percentages of CD4$^+$ DCs, CD8α^+ DCs, and CD11c^{int} PDCA-1$^+$ B220$^+$ CD11b$^-$ PDCs were decreased in infected mice as compared to uninfected mice. In contrast, the percentages of DN DCs were increased. These changes of the DC populations appeared on day 3 after infection. The absolute numbers of the cells in each DC subset changed in a manner similar to that of each subset's percentage (data not shown). The levels of MHC class II expression on CD11c$^+$ DCs of infected mice were comparable to those of uninfected mice (Fig.1). The expression levels of the costimulatory molecules, CD40, CD80, and CD86, on splenic CD11c$^+$ DCs were slightly upregulated in infected mice as compared to uninfected mice (data not shown).

These results indicate that splenic CD11c$^+$ DCs in infected mice express substantial amount of MHC class II and costimulatory molecules, however the antigen-presenting ability of the cells is severely impaired. One possible explanation would be that malaria infection selectively inhibits DC subsets that have high capability of antigen presentation, such as CD4$^+$ DCs and/or CD8α^+ DCs.

Aberrant expression of IRF4 and IRF8 in CD11c$^+$ DCs of infected mice

It has been well established that IRF4 and IRF8 regulate subset development and functional diversity of DCs (6). Therefore we next examined the expression of IRF4 and IRF8 in splenic CD11c$^+$ DCs of infected mice. Intracellular immunostains of IRFs in CD11c$^+$ DCs from uninfected mice confirmed the previous results (6). In CD4$^+$ DC subset, IRF4 was expressed and IRF8 was almost undetectable. Conversely, in CD8α^+ DCs IRF8 was abundantly expressed, but IRF4 was almost absent. DN DCs expressed IRF4, with a subpopulation expressing IRF8. PDCs expressed both IRF8 and IRF4. In infected mice, however, the levels of IRF4 and IRF8 expression were much lower than those in uninfected mice were (Fig. 2). While the numbers of CD4$^+$ DCs of parasite-infected mice were severely diminished relative to those of uninfected mice, the remaining CD4$^+$ DCs of infected mice expressed only

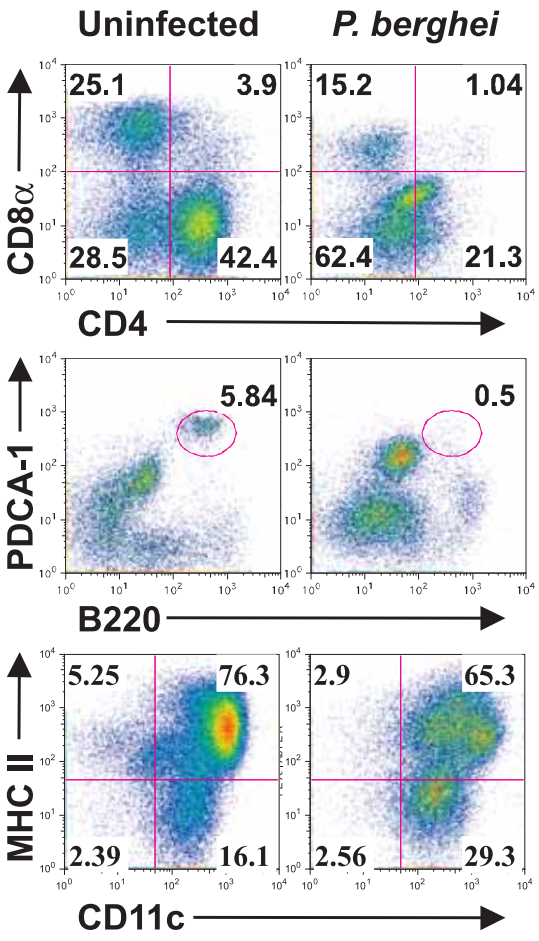

Fig. 1. Impaired development of splenic DC subsets in *P. berghei* infection
Representative flow cytometry profiles of the DC subsets in *P. berghei*-infected mice on day 5 after infection (*P. berghei*) and uninfected mice (uninfected) are analyzed. The profiles of cDCs, PDCs, and CD11c$^+$ MHC class II$^+$ DCs are illustrated in the top, middle, and bottom panels, respectively. Numbers in the quadrants and circles refer to the percentages of the cells. Data are representative of 2 experiments.

low levels of IRF4 compared with those of uninfected mice (data not shown). Similarly, the expression of IRF8 in the residual CD8α^+ DCs and PDCs of infected mice was lower than that in uninfected mice. DN DCs of the infected mice also displayed lower levels of both IRF4 and IRF8 than the cells of uninfected mice.

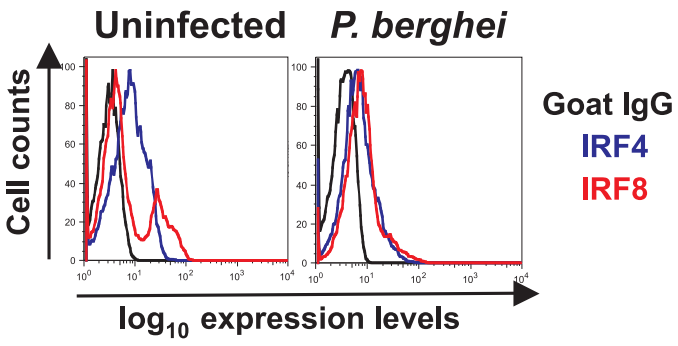

Fig. 2. Impaired IRF4 and IRF8 expression in splenic CD11c$^+$ DCs from *P. berghei*-infected mice
Splenic CD11c$^+$ DCs from infected mice on day 5 after infection or uninfected mice were stained for IRF4 and IRF8 as described in Materials and Methods. The representative profiles of 3 experiments are displayed.

Next we carried out reverse transcription followed by quantitative PCR and found that the mRNA expression levels of *Irf4* and *Irf8* were reduced 2-fold and 5-fold, respectively, in CD11c$^+$ DCs from infected mice as compared with uninfected mice (data not shown). Together, these data indicate that malaria infection compromises *Irf4* and *Irf8* gene expression in splenic CD11c$^+$ DCs, which may be the reason why DC subset development is severely impaired.

Decreased expression of IRF4 and IRF8 and impaired DC differentiation in the presence of pRBC in vitro

Because the changes of DC populations occurred progressively after infection (data not shown), we assumed that pRBC may target DC progenitors or differentiating DCs, rather than already differentiated DCs. To begin addressing this, we examined whether pRBC affect DC development and the expression of IRF4 and IRF8 *in vitro*. pRBC or normal RBC were added to the BM culture supplemented with Flt3L from day 0. CD24 was used as a CD8α^+ marker, because CD8α and CD4 are not expressed on the surface of DCs cultured *in vitro*. Flt3L is a cytokine known to support the development of multiple mouse DC subsets, especially CD24$^+$ DCs (equivalent to CD8α^+ DCs) and PDCs. Uninfected RBC did not affect *in vitro* DC development (Fig. 3). On the other hand, the addition

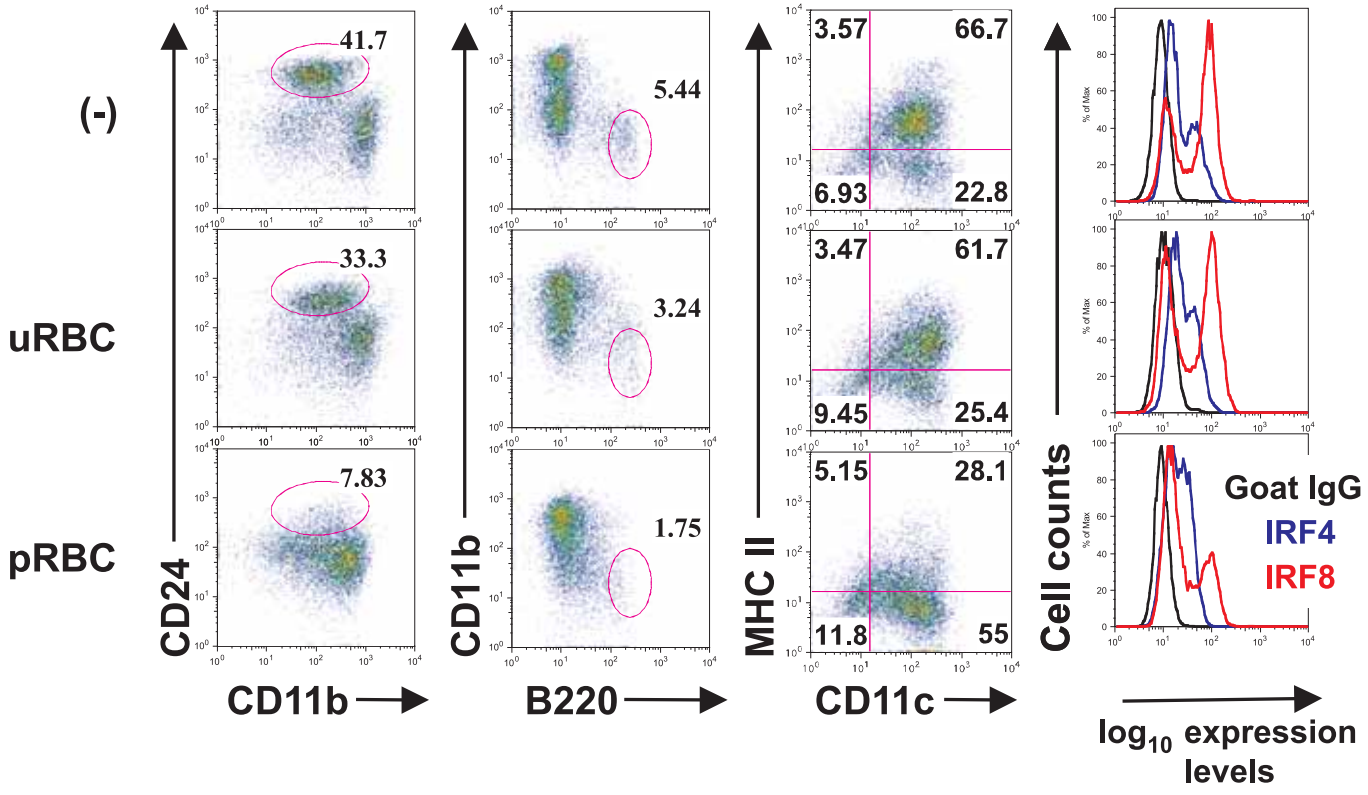

Fig. 3. Impairment of DC subset development by *P. berghei*-infected RBC *in vitro*
Bone marrow cells were cultured for 8 days in different conditions to develop BMDCs; in the presence of Flt3L alone (-), Flt3L with pRBC (pRBC), and Flt3L with uninfected RBC (uRBC). Numbers in the quadrants and circles refer to the percentages of the cells. Data are representative of 2 experiments.

of pRBC severely diminished the generation of $CD24^+$ DCs and PDCs (Fig. 3). Cell viability at day 8 in each culture was comparable, suggesting that cell death of specific DC populations is unlikely to be the reason for the aberrant DC populations.

Intracellular staining of IRF4 and IRF8 in the BMDCs revealed that pRBC inhibited IRF4 and IRF8 expression. These results suggest that pRBC affect DC progenitors and/or DCs at early stages of differentiation to compromise the expression of the IRFs and the development of functional DCs.

Discussion

In this study, we have demonstrated that splenic $CD11c^+$ DCs of *P. berghei*-infected mice display aberrant profiles of DC subsets concomitant with the reduced expression of transcription factors IRF4 and IRF8, known to be essential for DC development (6). Notably, among cDCs, the generation of subsets known to have high antigen-presenting ability, i.e. $CD4^+$ DCs and $CD8\alpha^+$ DCs, was selectively impaired. PDC numbers were also reduced. In contrast, the numbers of DN DCs was increased by *P. berghei* infection. Using *in vitro* DC differentiation culture, we have further shown that pRBC are responsible for targeting DC progenitor cells or differentiating DCs, causing reduced expression of IRF4 and IRF8 and the failure of DC subset development.

We and others have previously found that splenic $CD11c^+$ DCs of parasite-infected mice are defective in antigen presentation; both MHC class I (including cross-presentation) and II pathways are compromised in accordance with the disease progression (4)(5). A recent study has reported that $CD4^+$ and $CD8\alpha^+$ DC subtypes in the spleen were responsible for presenting antigens from *P. berghei* to $CD4^+$ T cells, whereas DN DCs were not directly involved in T cell priming

(7). Together with our findings in this study that the percentages and numbers of $CD4^+$ and $CD8\alpha^+$ DCs were decreased while those of DN DCs were increased in infected mice, it is possible that malaria infection selectively impairs the differentiation of DC subsets with high capability of antigen presentation. Although PDCs have been considered poor antigen presenters of exogenous antigens (8), the impaired PDC differentiation may compromise the innate immune responses against other pathogens such as viruses.

It has been recently reported that a new population of infection-induced atypical progenitors is emerged after infection of mice with *P. chabaudi* (9). Although this observation indicated that malaria parasites are able to interact with not only residing splenic $CD11c^+$ DCs but also bone marrow progenitor cells, its impact on DC development remained unaddressed. Our present study have clearly demonstrated that pRBC inhibits DC differentiation. Furthermore, our preliminary data suggest that addition of pRBC to the BMDC culture at later time points (for example, on day 2 or 4) induced much lesser effects on the inhibition of DC differentiation. These results support the notion that pRBC affect DC progenitors or DCs at early stages of differentiation to compromise the development of functional DCs.

Another critical finding in this study is that the impaired DC differentiation found in malaria was accompanied by downregulation of IRF4 and IRF8, transcription factors essential for the generation of multiple DC subsets. Although whether this downregulation is the cause or the result of abnormal DC differentiation still remains to be determined, we infer that the former may be the case, because even in the residual splenic DCs of infected mice and BMDCs generated in the presence of pRBC, the expression of IRF4 and/or IRF8 is significantly decreased.

Together, our results suggest that malaria infection, through pRBC, may affect DC progenitor cells to inhibit DC subset development by reducing the levels of IRF4 and IFR8 expression. It will be of interest to test whether reintroduction of IRF8/IRF4 into progenitor cells restores DC development. Further studies to clarify the mechanisms by which malaria downregulates IRF4 and IRF8 expression and to identify the molecules involved in the interaction (either direct or indirect) between pRBC and DCs will help to understand the pathogenesis of malaria.

Conclusion

In this study, we have shown that splenic $CD11c^+$ DCs of *P. berghe*i-infected mice exhibit aberrant profiles of DC subsets concomitant with the decreased expression of transcription factors IRF4 and IRF8, known to be essential for DC development. Our findings indicate that blood-stage of malaria parasites evades host immunity through the impairment of DC differentiation by reducing IRF4 and IRF8 expression. Future studies will be required to clarify the molecular basis of the downregulation of IRF4 and IRF8 in malaria infection.

Acknowledgement

This study was supported by a research grant from the Waksman Foundation Japan.

References

(1) Lundie, RJ. Antigen presentation in immunity to murine malaria. Curr Opin Immunol 2011; **23**:119-123.
(2) Shortman, K, YJ Liu. Mouse and human dendritic cell subtypes. Nat Rev Immunol 2002; **2**:151-161.
(3) Urban, BC, DJ Ferguson, A Pain, N Willcox, M Plebanski, JM Austyn, DJ Roberts. Plasmodium falciparum-infected erythrocytes modulate the maturation of dendritic cells. Nature 1999; **400**:73-77.
(4) Ichino, M. Impaired antigen presenting ability of a splenic $CD11c^+$ dendritic cell subset during Plasmodium berghei infection. Keystone Symposium, Alpbach, Austria 2008.
(5) Lundie, RJ, LJ Young, GM Davey, JA Villadangos, FR Carbone, WR Heath, BS Crabb. Blood-stage Plasmodium berghei infection leads to short-lived parasite-associated antigen presentation by dendritic cells. Eur J Immunol 2010; **40**:1674-1681.

(6) Tamura, T, P Tailor, K Yamaoka, HJ Kong, H Tsujimura, JJ O'Shea, H Singh, K Ozato. IFN regulatory factor-4 and -8 govern dendritic cell subset development and their functional diversity. J Immunol 2005; **174**:2573-2581.

(7) Lundie, RJ, TF de Koning-Ward, GM Davey, CQ Nie, DS Hansen, LS Lau, JD Mintern, GT Belz, L Schofield, FR Carbone, JA Villadangos, BS Crabb, WR Heath. Blood-stage Plasmodium infection induces $CD8^+$ T lymphocytes to parasite-expressed antigens, largely regulated by $CD8alpha^+$ dendritic cells. Proc Natl Acad Sci U S A 2008; **105**:14509-14514.

(8) Voisine, C, B Mastelic, AM Sponaas, J Langhorne. Classical $CD11c^+$ dendritic cells, not plasmacytoid dendritic cells, induce T cell responses to Plasmodium chabaudi malaria. Int J Parasitol 2010; **40**:711-719.

(9) Belyaev, NN, DE Brown, AI Diaz, A Rae, W Jarra, J Thompson, J Langhorne, AJ Potocnik. Induction of an IL7-R(+)c-Kit(hi) myelolymphoid progenitor critically dependent on IFN-gamma signaling during acute malaria. Nat Immunol 2010; **11**:477-485.

Listeria monocytogenes ActA-mediated escape from autophagic recognition

Michinaga Ogawa

Department of Microbiology and Immunology, The Institute of Medical Science, The University of Tokyo, 4-6-1, Shirokanedai, Minato-Ku, Tokyo 108-8639, Japan

ABSTRACT Autophagy degrades unnecessary organelles and misfolded protein aggregates, as well as cytoplasm invading bacteria. Nevertheless, *Listeria monocytogenes* efficiently escape autophagy. We show here that the recruitment of Arp2/3 complex and Ena/VASP via the bacterial ActA protein onto the bacterial surface disguises it from autophagic recognition, an activity that is independent of its ability to mediate bacterial motility. *L. monocytogenes* expressing ActA mutants lacking the ability to recruit the host proteins initially underwent ubiquitination, followed by recruitment of p62/SQSTM1 and LC3, before finally being entrapped by autophagy. The fundamental biomimetic ability of ActA was further demonstrated by creating aggregate-prone GFP-ActA-Q79C and GFP-ActA-170* chimeras, consisting of GFP, the ActA protein, and segments of polyQ or Golgi membrane protein GCP170. GFP-ActA-Q79C and GFP-ActA-170* formed aggregates in the host cell cytoplasm, however these ActA-containing aggregates are not targeted for association with ubiquitin and p62. Our findings indicate that ActA-mediated host protein recruitment is a unique bacterial disguising tactic to escape from autophagy.

Introduction

Autophagy is a ubiquitous degradation system in eukaryotic cells, and plays a crucial role in the cellular response to starvation and stress, the removal of damaged or surplus organelles, and the degradation of misfolded protein aggregates. Autophagy is a highly conserved process during which a double-layered isolation membrane wraps around undesirable cytoplasmic constituents and degrades them by fusion with a lysosome. Autophagy is also a pivotal innate defense system for eliminating invading cytoplasmic microbes. For example, Group A *Streptococcus* can invade epithelial cells; however, it is targeted and eventually destroyed by autophagy. *Mycobacterium tuberculosis* can be targeted by autophagy at an early stage of infection as long as the innate immune response of the host is intact. Some intracellular pathogens, such as *Legionella pneumophila*, *Coxiella burnetti*, and *Porphyromonas gingivalis* are enclosed in vacuoles, which they can modify to resist fusion with lysosomes, allowing survival and multiplication, unless autophagy is stimulated. In contrast, *Listeria monocytogenes* (and *Shigella*), which are motile within the host cell cytoplasm via the ability of their surface-expressed proteins to recruit actin, can escape autophagic recognition. Multiple mechanisms to avoid autophagic destruction have been described for *L. monocytogenes*; nevertheless, studies regarding the *L. monocytogenes* factors involved in escape from autophagy are controversial.

To elucidate the tactics of *L. monocytogenes* to evade autophagy, we focused on the role of the ActA protein, since the protein is distributed on the surface of the bacteria and plays the central role in mediating the bacterial actin-based motility. The ActA protein is composed of several functional domains; The N-terminal ActA domain binds to and activates the Arp2/3 complex, which directly catalyzes actin nucleation, and

binds monomeric actin. The central domain, which includes four proline-rich repeats, recruits members of the Ena/VASP family, that control the efficiency of bacterial motility. The C-terminal ActA protein possesses a transmembrane anchoring domain and a spacer required for interacting with bacterial cell wall.

Materials and Methods

Bacterial strains and plasmids.

Wild-type *L. monocytogenes* EGD (WT) and its derivatives were cultured as described previously. To visualize living bacteria, pMV158-GFP was transformed into WT and its derivatives. *p62* cDNAs were amplified by RT-PCR from total RNA of HeLa cells. The *p62* gene was cloned into pcDNA3.1-3xMyc and pMX-puro-Myc. The *mjd1a* gene covering the entire coding sequence with 79 repeats of CAG (*Q79C*) was amplified by PCR from pCMX-HA-Q79C. The *act*A-*Q79C* fusion gene was cloned into pEGFP (Invitrogen). The *act*A gene was cloned into pcDNA3.1-3xMyc and pGFP-170*.

Cell cultures and transfections.

MDCK cells stably expressing GFP-LC3 (MDCK/pGFP-LC3) and mCherry-LC3 (MDCK/pmCherry-LC3) were maintained in Dulbecco's modified Eagle's medium (DMEM; Sigma) containing 10% fetal calf serum (FCS; GIBCO) and 1 mg/ml G418 (Sigma). *atg5*$^{+/+}$, *atg5*$^{-/-}$, and *p62*$^{-/-}$ mouse embryonic fibroblast (MEF) cells and COS-7 cells were maintained in DMEM containing 10% FCS. To construct MDCK cells stably expressing GFP-LC3 and p62-3xMyc, the MDCK cells were co-transfected with pEGFP-LC3 and pcDNA3.1-p62-3xMyc using Lipofectamine 2000 (Invitrogen), and maintained in DMEM containing 10% FCS and 1 mg/ml G418. COS-7 cells and HeLa cells were transfected with FuGENE6 transfection reagent (Roche). At 14-18h after transfection, COS-7 cells were fixed with 4% paraformaldehyde in Phosphate-buffered saline (PBS) for immunofluorescence microscopy. HeLa cells were treated with or without Bafilomycin A1 (Sigma) for 8 h and washed with PBS three times and lysed with 100 μl of 3x SDS sample buffer per well directly for western blot analysis.

Antibodies and reagents.

Rabbit polyclonal antibodies against *L. monocytogenes* O-antigen I/II (DENKA SEIKEN), LC3 (PM036; MBL), GFP (598; MBL), Myc (A-14; Santa Cruz), Atg5 (A0731; Sigma) and Ubiquitin (UG9510; BIOMOL and Z0458; Dako), and mouse monoclonal antibodies against multiubiquitin (FK2; MBL), Myc (9B11; Cell signaling), Arp2 (FMS96; Abcam), VASP (610447; BD transduction Laboratories), p62 (610832; BD transduction Laboratories), and Actin (MAB1501; Millipore) were used as primary antibodies. Cy5, TRITC, FITC, HRP, or ALP conjugated anti-rabbit or mouse IgG antibodies were used as secondary antibodies. Rhodamine phalloidin (Sigma) was used to stain F-actin, and DAPI (Molecular Probes) was used to stain DNA. Earle's balanced salt solution (EBSS) medium (Sigma) and 100 μg/ml Rapamycin (Sigma) were used to induce autophagy.

Retroviral infection.

To construct *atg5*$^{+/+}$, *atg5*$^{-/-}$ MEF cells stably expressing GFP-LC3 and *p62*$^{-/-}$ MEF cells stably expressing wild-type (WT), ΔLIR, ΔUBA, ΔLIR-ΔUBA, or K7AD69A p62-3xMyc and GFP-LC3, cDNAs encoding these proteins were subcloned into pMX-puro expression vectors. The obtained vectors were transfected into Plat-E cells to generate recombinant mouse retroviruses. MEF cells were infected with the recombinant mouse retroviruses and selected in DMEM containing 10% FCS and 2 μg/ml puromycin (Sigma).

Infection with L. monocytogenes.

MDCK/pGFP-LC3 cells were seeded at 4 x 10^4 cells/ml on glass cover slips in 6-well plates and cultured for 4 days at 37°C. MEF cells were seeded at 5 x 10^4 cells/ml in 6-well plates. WT or Δ*act*A mutant strains were cultured in brain heart infusion

(BHI) broth (BD) overnight at 30°C prior to infection. Bacterial suspensions (Δ*act*A2: 10 μl, WT and other Δ*act*A mutants: 5 μl) were diluted in 1.5 ml fresh cell culture medium without antibiotics and added to each well, and then centrifuged at 700 x g for 10 min. Cells were incubated for 1 h at 37°C, washed with PBS three times, and DMEM supplemented with 10% FCS and 100 μg/ml gentamycin was added to each well to kill any extracellular bacteria. After incubation for indicated periods at 37°C, the cells were fixed with 4% paraformaldehyde in PBS. Fixed cells were quenched with 50 mM NH_4Cl in PBS, permeabilized with 0.2% Triton X-100 in PBS, and blocked with 2% BSA in TBS. After staining using indicated antibodies, the specimens were analyzed by LSM510 (Carl Zeiss). Fluorescence intensity was measured with LSM510 version 3.2 software (Carl Zeiss). For western blot analysis, the cell were washed with PBS three times and lysed with 100 μl of 3x SDS sample buffer per well directly. The equal volume of lysates were separated by SDS-PAGE and transferred to a PVDF membrane. For arresting bacterial motility, bacteria inoculated cells after incubation for 1 h at 37°C were washed with PBS three times and cultured in DMEM supplemented with 10% FCS, 100 μg/ml gentamycin and 2 μM Phalloidin Oleate (Sigma) for 1 h. And then the cells were changed medium to DMEM supplemented with 10% FCS, 100 μg/ml gentamycin, 1 μM Phalloidin Oleate and 10 μg/ml Cytochalasin D (Sigma) for 1 h and fixed with 4% paraformaldehyde in PBS.

Intracellular bacterial multiplication assay.

MDCK cells or MEF cells seeded into 24-well plates were infected with WT or Δ*act*A2 as described above. At each time point, the cells were washed and lysed with 0.5% Triton X-100 in PBS. The lysates were diluted with PBS and plated onto BHI-agar plates, and the number of intracellular bacteria was counted as CFU.

Electron microscopy and immunoelectron microscopy.

MDCK cells seeded in 35 mm dishes were infected with WT or Δ*act*A2 for 2 or 4 h as described above. Cells were fixed with 2% glutaraldehyde in PBS, post-fixed in 2% OsO_4, and embedded in epoxy resin. Ultra-thin sections were doubly stained with uranyl acetate and lead citrate. The number of bacteria associated with autophagosomes was determined by visual counting under transmission electron microscopy. About 30 independent bacteria from sections obtained by the 3 blocks were examined in triplicate, for each experimental condition. For immunoelectron microscopy, the post-embedding immunogold method was performed. Infected cells were fixed with 0.1% glutaraldehyde and 4% paraformaldehyde in PBS, embedded in LR-White resin, stained with antibody against GFP or against ubiquitin, and stained with anti-mouse IgG conjugated with gold colloidal particles (10 nm diameter; EY laboratory) or anti-rabbit IgG conjugated with gold colloidal particles (5 nm diameter; EY laboratory).

Results

L. monocytogenes ΔactA2 mutant is recognized by autophagy

MDCK/pGFP-LC3 [Madine-Darby canine kidney (MDCK) cells stably expressing GFP-LC3] cells were infected with wild-type *L. monocytogenes* (WT) or Δ*act*A2 (lacking amino acid residues 20-602), and the colocalization of GFP-LC3 with the bacteria was investigated. At 2 or 4 h following infection, GFP-LC3 was associated more frequently with Δ*act*A2 (58% and 60%) than WT (5.1% and 5.3%) (Fig. 1a, b). The level of LC3-II, the active form of LC3, increased in MDCK cells infected with Δ*act*A2 for 4 h, but no significant change was observed in WT infected cells (Fig. 1c). Upon treatment of MDCK/pGFP-LC3 cells with 3-methyladenine (3-MA), an autophagy inhibitor, the population of LC3-positive Δ*act*A2 declined from 70% (without 3-MA) to 29% (with 3-MA) (Fig. 1d). The intracellular survival of Δ*act*A2 after 4 h of infection was significantly less than that of WT (Fig. 1e, f). In MDCK cells treated with 3-MA or *atg5*$^{-/-}$MEF cells, the intracellular survival of Δ*act*A2 after 4 h of infection was increased to the same level

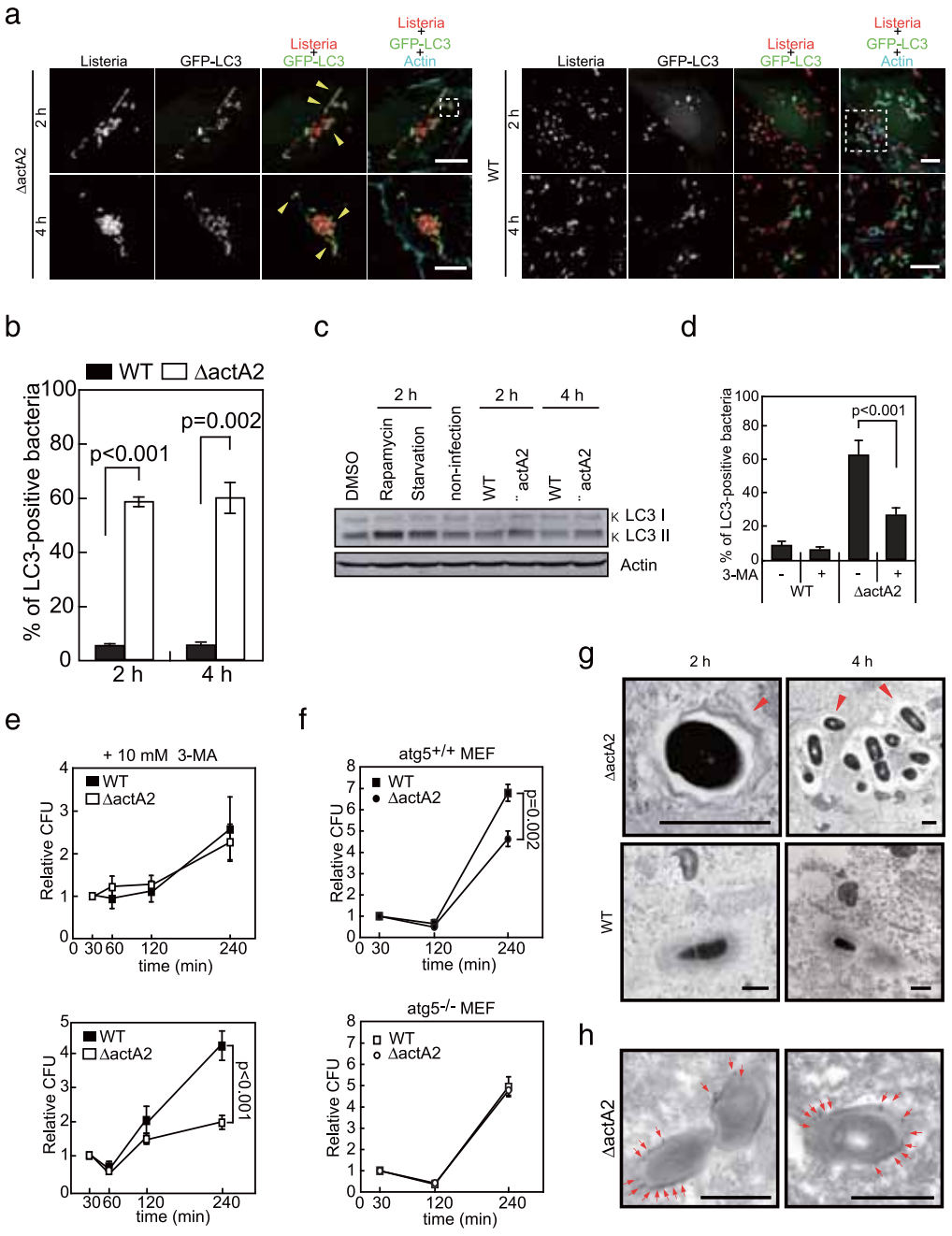

Fig. 1. *L. monocytogenes* lacking ActA is a target of autophagy.
(a) MDCK/pGFP-LC3 cells infected with WT or Δ*act*A2 were stained with anti-*Listeria* antibody (red) and rhodamine-phalloidin (light-blue). Scale bars, 10 μm. Arrowheads indicate GFP-LC3-positive bacteria. (b) Quantification of the number of GFP-LC3-positive bacteria shown in (a). Data are presented as means ± s.e.m. At least 500 bacteria were counted in each experiment ($n \geq 6$). (c) LC3 levels in infected MDCK cells. MDCK cells were infected with WT or Δ*act*A2 for the indicated times. EBSS and 100 μg/ml Rapamycin were used as controls. (d) Quantification of the number of GFP-LC3-positive bacteria in MDCK/pGFP-LC3 cells treated with or without 10 mM 3-MA. Data are presented as means ± s.e.m. At least 500 bacteria were counted in each experiment ($n = 8$). (e) Intracellular survival of WT or Δ*act*A2 in MDCK cells in the presence or absence of 10 mM 3-MA. Data are presented as means ± s.e.m. ($n \geq 3$). (f) Intracellular survival of WT or Δ*act*A2 in *atg5*$^{+/+}$ MEF cells. Data are presented as means ± s.e.m. ($n \geq 3$). (g) Electron micrograph of infected MDCK cells. Cells were infected with Δ*act*A2 or WT. Some Δ*act*A2 were trapped in multi-layered membranes (arrowhead). Scale bars, 0.5 μm. (h) MDCK/pGFP-LC3 cells infected with Δ*act*A2 for 4 h. Gold particles (arrow) indicate GFP-LC3. Scale bars, 0.5 μm.

of WT (Fig. 1e, f). Electron microscopic (EM) analysis confirmed that while WT was often surrounded by actin clouds, Δ*act*A2 was frequently enclosed in lamellar membranes (Fig. 1g). The lamellar membranous structure surrounding Δ*act*A2 in MDCK/pGFP-LC3 cells was specifically reactive to immunogold coated with anti-GFP antibody (Fig. 1h), indicating that the presence of ActA is important for escape from autophagy.

The relationship between the autophagic recognition and the ability of ActA to mediate actin polymerization

We next infected MDCK/pGFP-LC3 cells with a series of chromosomally deleted *act*A in-frame truncations, and investigated the relationship between the autophagic recognition and the ability of ActA to mediate actin polymerization. The results showed that Δ*act*A3, -9, -14, and -16, which lack the Arp2/3 complex binding domain, Δ*act*A5 and -17, which lack the VASP binding domain or its C-terminal region, and Δ*act*A13, which lacks the actin binding region, were all LC3-negative regardless of their respective capacities for intracellular motility. In contrast, the mutants Δ*act*A2 and -21, which lack all of these binding domains, were LC3-positive (Fig. 2a-e). These results suggested that as long as the ability of ActA to recruit host proteins was retained, such as for either the Arp2/3 complex, VASP, or Actin, bacteria were protected from autophagic recognition.

ActA enables the bacterium to evade ubiquitination

The accumulation of misfolded protein aggregates in the cytoplasm induces their degradation by polyubiquitination followed by autophagic degradation. When MDCK/pGFP-LC3 cells infected with WT or Δ*act*A2 were observed by immunofluorescence staining with an anti-multiubiquitin (Ub) antibody 1 h after infection, neither WT nor Δ*act*A2 was Ub-positive, although some LC3-positive puncta were observed in the cellular cytoplasm (Fig. 3a, c). At 2 h after infection, 59% of Δ*act*A2 were Ub-positive and 57% were LC3-positive, whereas only 7% of WT were Ub-positive and 8% were LC3-positive. 78% of Ub-positive Δ*act*A2 were also LC3-positive (Fig. 3b, c). Consistent with this, when MDCK/pGFP-LC3 cells were infected with Δ*act*A2 for 2 h and analyzed by immunogold EM with antibodies against Ub and GFP, the bacterial surface was highly labeled with both anti-Ub and anti-GFP antibodies (Fig. 3d). We next infected MDCK/pGFP-LC3 cells with a series of chromosomally deleted *act*A in-frame truncations, and investigated the localization of ubiquitin signal around bacteria. Infection of MDCK/pGFP-LC3 cells with Δ*act*A3,-5,-9,-13,-14, -16, and -17 for 2 h resulted in lower Ub signals on the bacteria than observed for Δ*act*A2, and -21 (Fig. 4a, b). These data support the idea that the ability of ActA to interact with host proteins enables the bacterium to evade ubiquitination.

Ubiquitination of Δact A2 occurs prior to autophagy induction

To examine whether ubiquitination or autophagy occurs first around cytoplasmic bacteria, we investigated LC3- and Ub-positive bacterial populations at early time points following infection. 30 min after infection, bacteria were mostly free from endocytic vacuoles, and about 20% of Δ*act*A2 and WT were LC3- and Ub-positive. At 2 h, 10% of WT were Ub- and LC3-positive, while up to 60% of Δ*act*A2 were LC3-positive. The increase in Ub-positive Δ*act*A2 was followed by an increase in LC3-positivity (Fig. 3c). To further investigate whether ubiquitination occurs before LC3 association, the number of Ub-positive bacteria was analyzed under conditions that suppress autophagy. Treatment with 3-MA reduced the number of LC3-positive Δ*act*A2, but did not significantly affect the number of Ub-positive Δ*act*A2 (Fig. 5a, c). We next corroborated these results using *atg5*$^{-/-}$MEF cells. In *atg5*$^{+/+}$MEF cells, the number of Ub- or LC3-positive Δ*act*A2 was greater than the number of Ub- or LC3-positive WT (data not shown), and no significant differences were observed in the number of Ub-positive Δ*act*A2 in *atg5*$^{+/+}$or *atg5*$^{-/-}$MEF cells (Fig. 5b, d).

Involvement of p62 in autophagy targeting L. monocytogenes

Recent studies have indicated that the

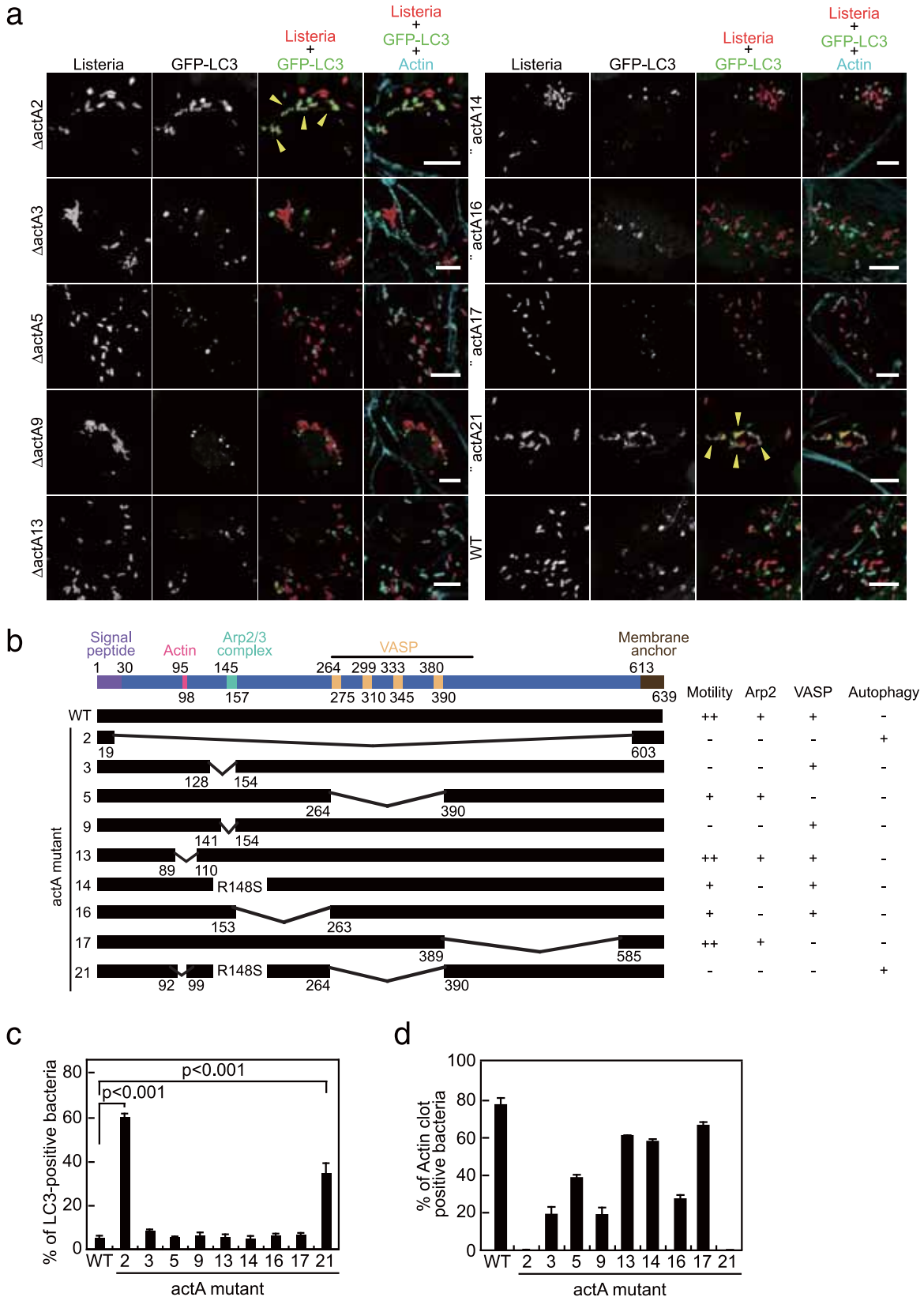
a
Listeria
GFP-LC3
Listeria + GFP-LC3
Listeria + GFP-LC3 + Actin
ΔactA2
ΔactA3
ΔactA5
ΔactA9
ΔactA13
ΔactA14
ΔactA16
ΔactA17
ΔactA21
WT
b
Signal peptide
Actin
Arp2/3 complex
VASP
Membrane anchor
1 30 95 145 264 299 333 380 613
98 157 275 310 345 390 639
Motility
Arp2
VASP
Autophagy
WT ++ + + -
2 - - - +
3 - - + -
5 + + - -
9 - - + -
13 ++ + + -
14 + - + -
16 + - + -
17 ++ + - -
21 - - - +
actA mutant
c
% of LC3-positive bacteria
p<0.001
p<0.001
WT 2 3 5 9 13 14 16 17 21
actA mutant
d
% of Actin clot positive bacteria
WT 2 3 5 9 13 14 16 17 21
actA mutant

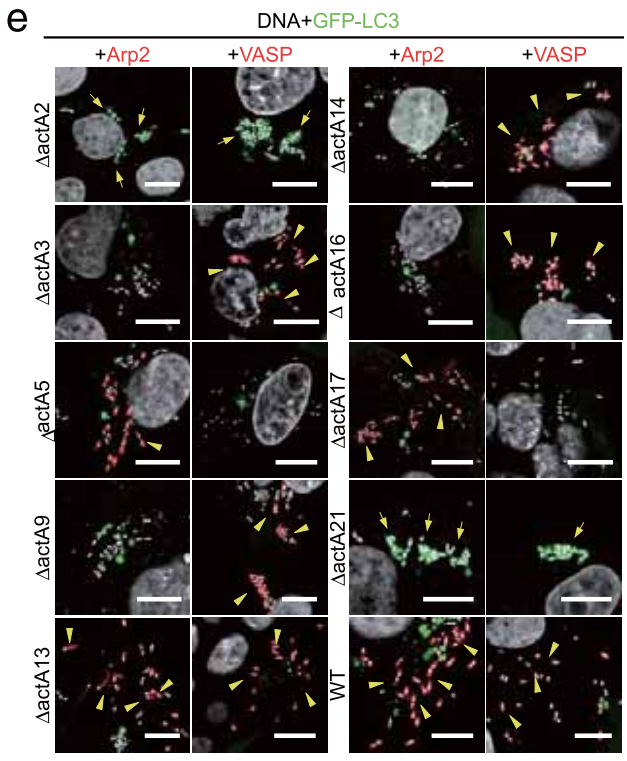

Fig. 2. The ability of ActA to mediate bacterial intracellular motility is not relevant to the ability of *L. monocytogenes* to escape autophagy.
(a) MDCK/pGFP-LC3 cells were infected with WT or a series of *act*A mutant strains for 2 h, and stained with anti-Listeria antibody (red) and rhodamine-phalloidin (light-blue). Scale bars, 10 μm. Arrowheads indicate GFP-LC3-positive bacteria. (b) Schematic diagram of the domain of ActA involved in actin nucleation. The signal peptide, the membrane anchor, the proline-rich repeats, the putative actin-binding motif, and the Arp2/3 complex-recruiting motif are shown in violet, brown, yellow, pink, and light-blue, respectively. The deleted amino acid regions of Δ*act*A3, -5, -9, -13, -16 and -17 are 129-153, 265-389, 142-153, 90-109, 154-262 and 390-584 respectively. Δ*act*A14 is a single amino acid substituted ActA protein (R148S). Δ*act*A21 harbours deletions of amino acids 93-98, 265-389 as well the substitution R148S. (c and d) Quantification of the number of GFP-LC3-positive bacteria (c), actin accumulating bacteria (d). Data are presented as means ± s.e.m. At least 500 bacteria were counted in each experiment ($n = 3$). (e) MDCK/pGFP-LC3 cells were infected with WT or a series of *act*A mutant strains for 2 h and stained with anti-Arp2 antibody or anti-VASP antibody (red) and DAPI (white). Scale bars, 10 μm. Arrowheads indicate Arp2 or VASP-positive bacteria and arrows indicate GFP-LC3-positive bacteria.

p62/SQSTM1 (p62) protein serves as a link between LC3 and polyubiquitinated substrates, and functions to induce autophagy of these substrates. We therefore infected MDCK cells that were stably expressing GFP-LC3 and p62-3xMyc (MDCK/pGFP-LC3/pp62-3xMyc) with Δ*act*A2 to investigate the involvement of p62 in bacterial ubiquitination. After 2 h of infection, p62 colocalized with Ub and GFP-LC3 around Δ*act*A2 (Fig. 6a, b). *p62*$^{-/-}$MEF cells stably expressing GFP-LC3 (*p62*$^{-/-}$) were infected with and Δ*act*A2 for 2 h. The amount of Ub associated with Δ*act*A2 in *p62*$^{-/-}$cells was similar to that in *p62*$^{-/-}$MEF cells stably expressing GFP-LC3 and p62-3xMyc (*p62*$^{-/-}$/p62); however, the amount of LC3 associated with Δ*act*A2 in *p62*$^{-/-}$cells was less than half that in *p62*$^{-/-}$/p62 cells (Fig. 6c, d). The rate of intracellular survival of Δ*act*A2 compared with WT in *p62*$^{-/-}$/p62 cells was significantly lower (Fig. 6d).

Domain analysis of p62 in autophagy targeting L. monocytogenes

p62 contains a LC3 interacting region (LIR) domain that interacts with LC3 and an ubiquitin associated (UBA) domain that interacts with Ub. We created a series of p62-3xMyc deletions lacking the LIR, UBA, both LIR and UBA domains (ΔLIR-ΔUBA), or containing two amino acid substitutions

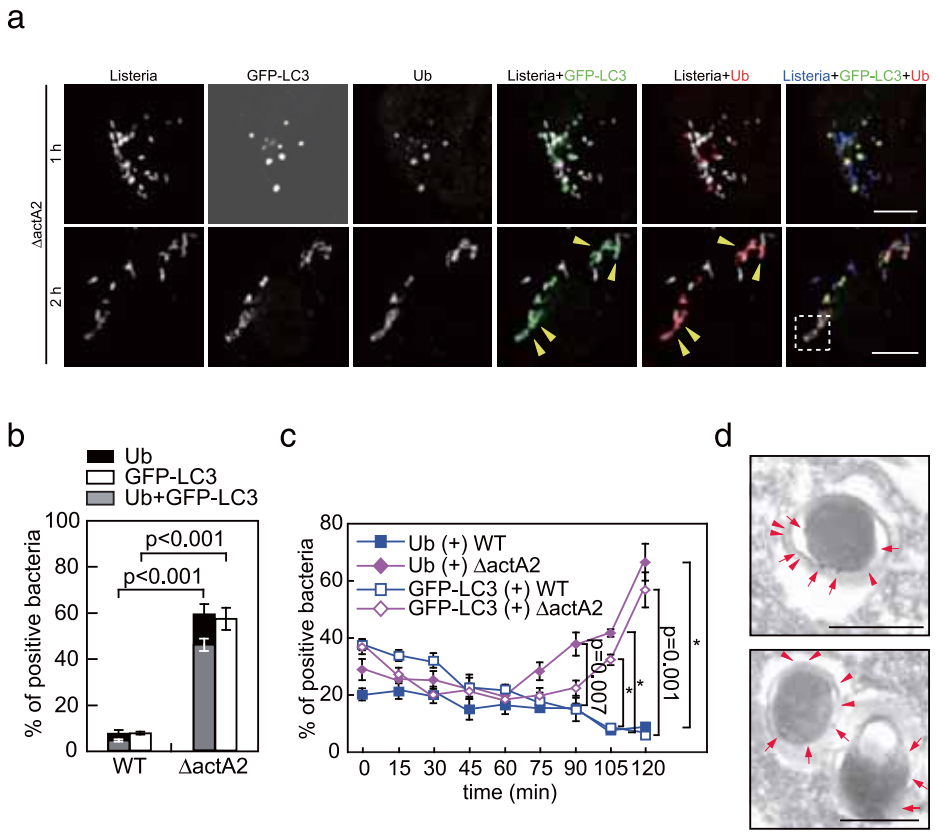

Fig. 3. The localization of ubiquitin around *L. monocytogenes* occurs before autophagy induction
(a) Colocalization of ubiquitin with Δ*act*A2. MDCK/pGFP-LC3 cells infected with Δ*act*A2 were stained with anti-*Listeria* antibody (blue) and anti-Ub antibody (red). Scale bars, 10 μm. Arrowheads indicate GFP-LC3-positive and Ub-positive bacteria. (b) Quantification of the number of GFP-LC3-positive, Ub-positive, or GFP-LC3-positive of the whole Ub-positive bacteria. Data are presented as means ± s.e.m. At least 500 bacteria were counted in each experiment ($n = 3$). (c) Kinetics of the appearance of GFP-LC3-positive and Ub-positive bacteria. Data are presented as means ± s.e.m. At least 500 bacteria were counted in each experiment ($n = 3$). *, $p < 0.001$. (d) Immunogold electron micrograph of MDCK/pGFP-LC3 cells infected with Δ*act*A2.5 nm gold particles (arrowhead) indicate GFP-LC3, while 10 nm gold particles (arrow) indicate Ub. Scale bars, 0.5 μm.

(K7A/D69A) that cause a defect in p62 multimerization (Fig. 7a). These proteins were expressed in *p62*$^{-/-}$cells (Fig. 7b) and the association of LC3 with Δ*act*A2 was examined. Although 43% of Δ*act*A2 in *p62*$^{-/-}$/p62 cells were LC3-positive, significantly lower numbers were observed in the other *p62*$^{-/-}$strains (Fig. 7c, d), indicating that ubiquitinated Δ*act*A2 recruits LC3 via p62.

The ability of ActA to recruit Arp2/3 complex and VASP is essential for the inhibition of Ub- or p62-mediated aggregate formation

Finally, we demonstrated the functional relationship between the intrinsic ability of ActA to recruit Arp2/3 complex and VASP and its ability to inhibit Ub and p62 accumulation by creating aggregate-prone constructs based on poly-Q (Q79C) and GFP-170*. COS-7 cells expressing GFP-Q79C, GFP-ActAFL-Q79C (comprising of GFP, full-length ActA, and Q79C), GFP-ActAN-Q79C (consisting of GFP, the N-terminal 30-389 ActA residues, and Q79C), or GFP-ActAC-Q79C (consisting of GFP, the C-terminal 390-612 ActA residues, and Q79C) were investigated for the ability to recruit Ub, p62, Arp2/3 complex, and VASP by immunofluorescence staining (Fig. 8a). Expression of GFP-Q79C or GFP-ActAC-Q79C in COS-7 cells, induced the formation of Ub- and p62-positive aggregates (Fig. 8b). However, upon expression of GFP-ActAFL-Q79C or GFP-ActAN-Q79C in COS-7 cells, neither Ub

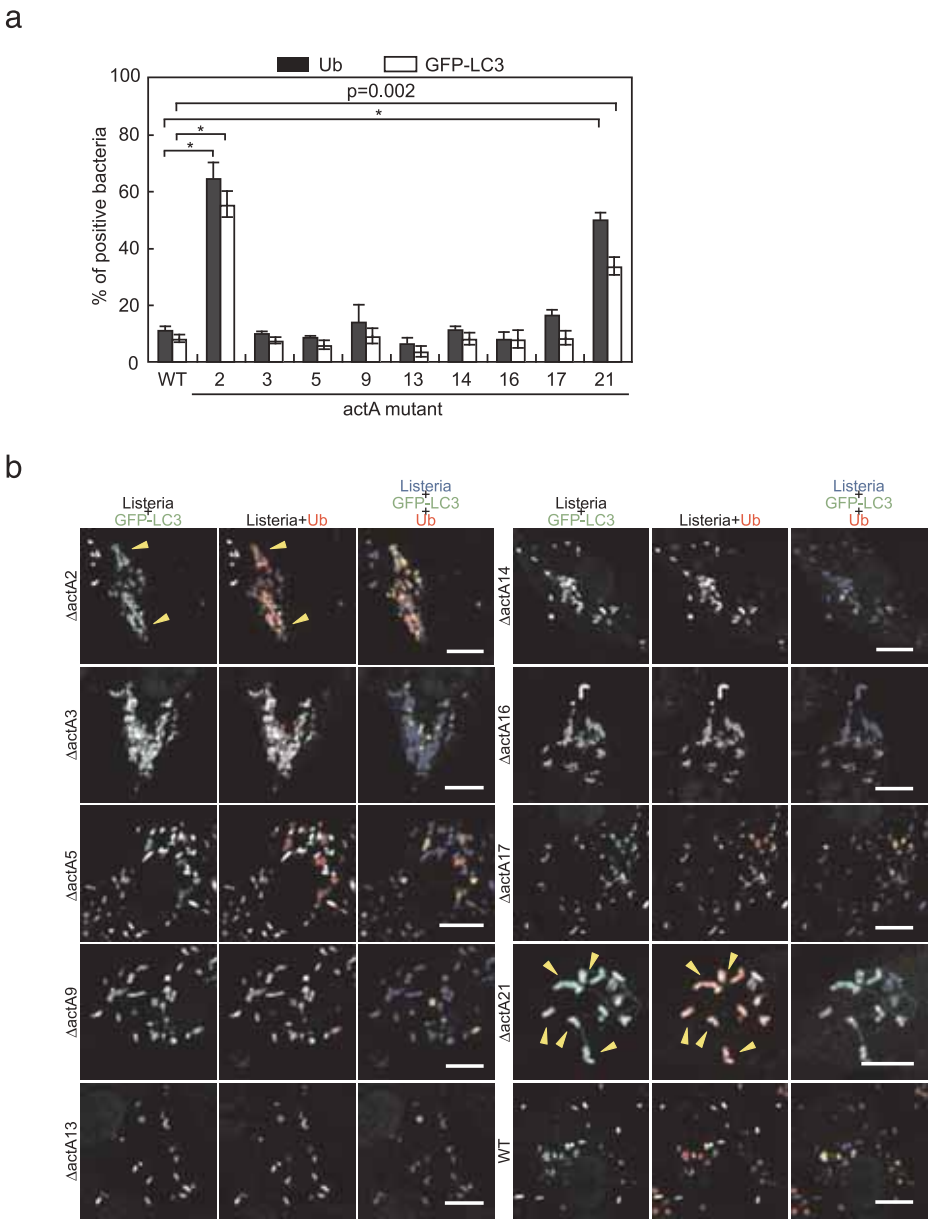

Fig. 4. The localization of GFP-LC3 around *L. monocytogenes* correlates with the ubiquitin (Ub) signal around the bacteria.
(a) Quantification of the number of Ub-positive or GFP-LC3-positive bacteria. MDCK/pGFP-LC3 cells were infected with WT or a series of *act*A mutant strain for 2 h. Data are presented as means ± s.e.m. At least 500 bacteria were counted in each experiment ($n = 3$). *, $p < 0.001$. (b) MDCK/pGFP-LC3 cells were stained with anti-Listeria antibody (blue) and anti-Ub antibody (red). Scale bars, 10 μm. Arrowheads indicate GFP-LC3- and Ub-positive bacteria.

nor p62 was found to colocalize with the GFP signal. We exploited another aggregate-prone construct with GFP-170*, a nonpoly-Q protein, which contains GFP fused to an internal segment of the Golgi Complex Protein 170, that was also previously used as a model substrate for aggregate formation (Fig. 9a). Upon expression in COS-7 cells, GFP170* and GFP-ActAC-170* (consisting of GFP, the C-terminal 390-612 ActA residues, and 170*) in the cytoplasm formed puncta, to which Ub and p62 colocalized (Fig. 9b). However, upon expression of GFP-ActAFL-170* (comprising GFP, full-length ActA, and 170*) in COS-7 cells, or

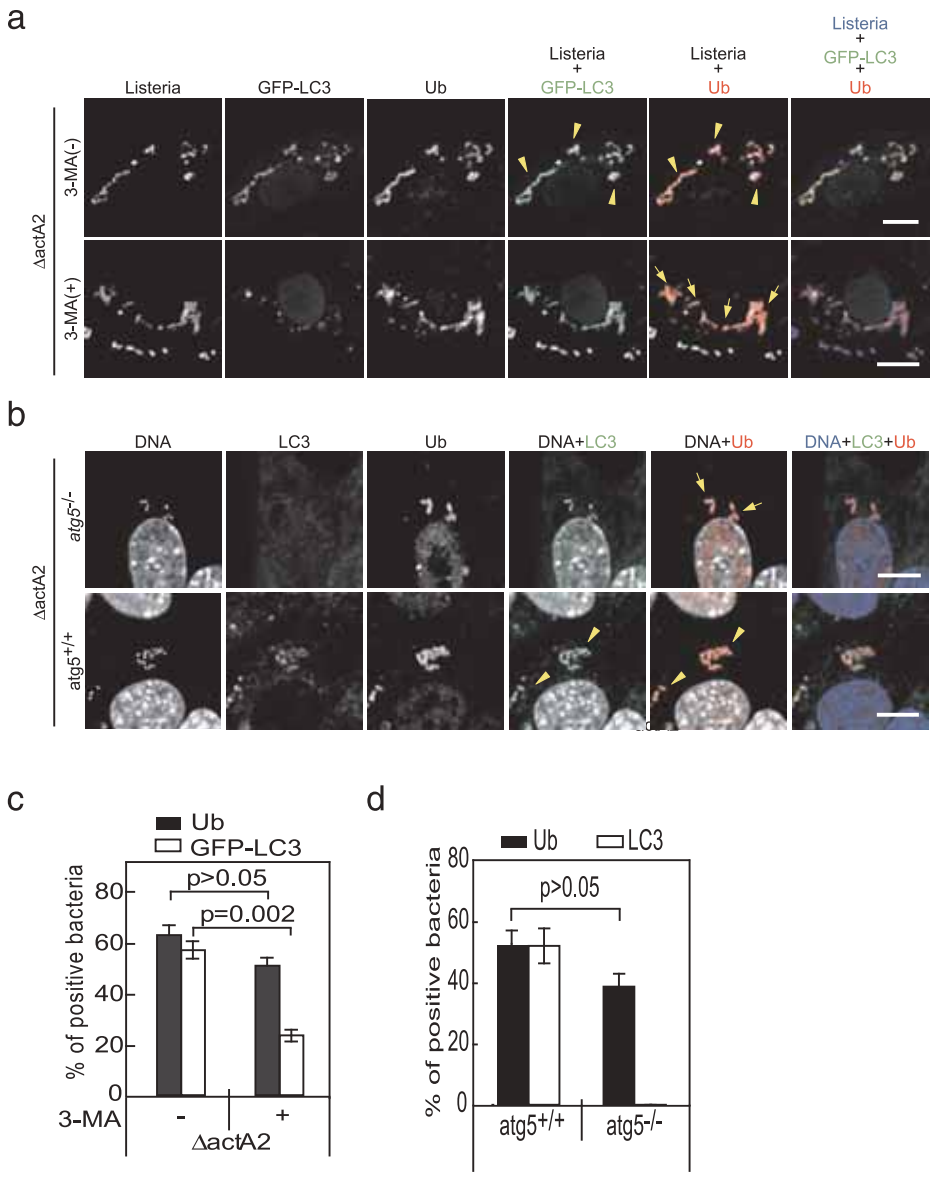

Fig. 5. Ubiquitination of Δ*act*A2 occurs prior to autophagy induction
(a) MDCK/pGFP-LC3 cells were infected with Δ*act*A2 for 2h and treated with or without 10 mM 3-MA. Cells were stained with anti-Listeria antibody (blue) and anti-Ub antibody (red). Scale bars, 10 μm. Arrows indicate Ub-positive bacteria. Arrowheads indicate GFP-LC3- and Ub-positive bacteria. (b) MEF cells were stained with anti-LC3 antibody (green), anti-Ub antibody (red) and DAPI (blue). Scale bars, 10 μm. Arrows indicate Ub-positive bacteria. Arrowheads indicate LC3- and Ub-positive bacteria. (c) Quantification of the number of Ub-positive and GFP-LC3-positive bacteria. MDCK/pGFP-LC3 cells infected with WT or Δ*act*A2 were treated with or without 10 mM 3-MA. Data are presented as means ± s.e.m. At least 500 bacteria were counted in each experiment ($n \geq 3$). (d) Quantification of the number of Ub-positive or LC3-positive bacteria. *atg5*$^{+/+}$ or *atg5*$^{-/-}$ MEF cells were infected with Δ*act*A2 for 2 h. Data are presented as means ± s.e.m. At least 500 bacteria were counted in each experiment ($n = 4$).

GFP-ActAN-170* (consisting of GFP, the N-terminal 30-389 ActA residues, and 170*), in COS-7 cells under the same conditions, neither Ub nor p62 was found to colocalize with the GFP signal. Thus we concluded that the ability of ActA to interact with Arp2/3 complex and VASP plays an important role for *L. monocytogenes* in interfering with autophagy (Fig. 10).

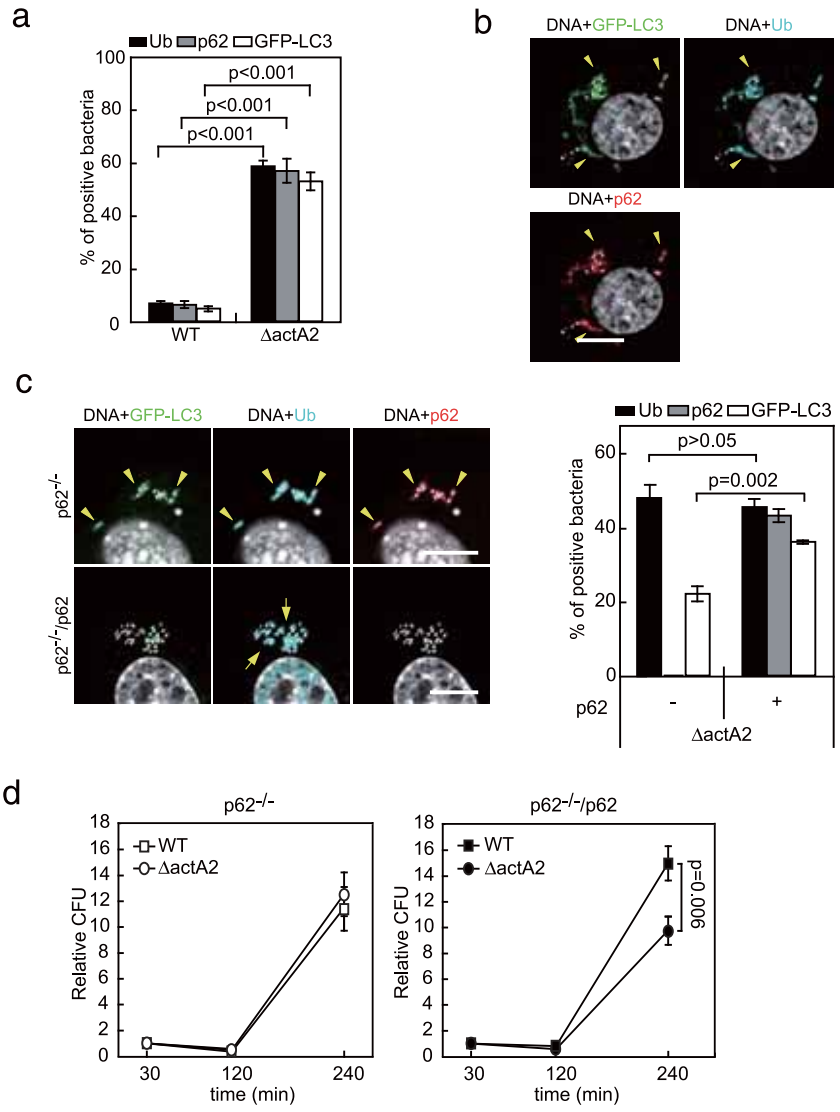

Fig. 6. p62 facilitates autophagy of ubiquitinated Δ*act*A2.
(a) Quantification of the number of Ub-positive, p62-positive, GFP-LC3-positive bacteria. MDCK/pGFP-LC3/pp62-3xMyc cells were infected with WT or Δ*act*A2 for 2h. Data are presented as means ± s.e.m. At least 500 bacteria were counted in each experiment (n= 6). (b) Colocalization of p62 with Δ*act*A2. MDCK/pGFP-LC3/pp62-3xMyc cells were stained with anti-Ub antibody (light-blue), anti-Myc antibody (red) and DAPI (white). Scale bars, 10 μm. Arrowheads indicate GFP-LC3-, Ub- and p62-positive bacteria. (c) *p62*$^{-/-}$ or *p62*$^{-/-}$/p62 cells were infected with WT or Δ*act*A2 for 2 h, and stained with anti-Ub antibody (blue), anti-Myc antibody (red) and DAPI (white), and the number of Ub-positive, p62-positive, GFP-LC3-positive bacteria was quantified . Scale bars, 10 μm. Arrows indicate Ub-positive bacteria. Arrowheads indicate GFP-LC3-, Ub- and p62-positive bacteria. Data are presented as means ± s.e.m. At least 500 bacteria were counted in each experiment ($n \geq 3$). (d) Intracellular survival of WT or Δ*act*A2 in *p62*$^{-/-}$ cells or *p62*$^{-/-}$/p62 cells. Data are presented as means ± s.e.m. ($n \geq 4$).

Discussion

Previous studies have suggested *L. monocytogenes* possesses multiple mechanisms to avoid autophagic destruction. An early study using macrophages indicated that chloramphenicol-induced metabolic arrest of *L. monocytogenes* resulted in bacteria being trapped in autophagosomes, with subsequent lysosomal degradation, suggesting a requirement for *de novo* protein synthesis in escaping autophagy in macrophages. A later study using MEF cells

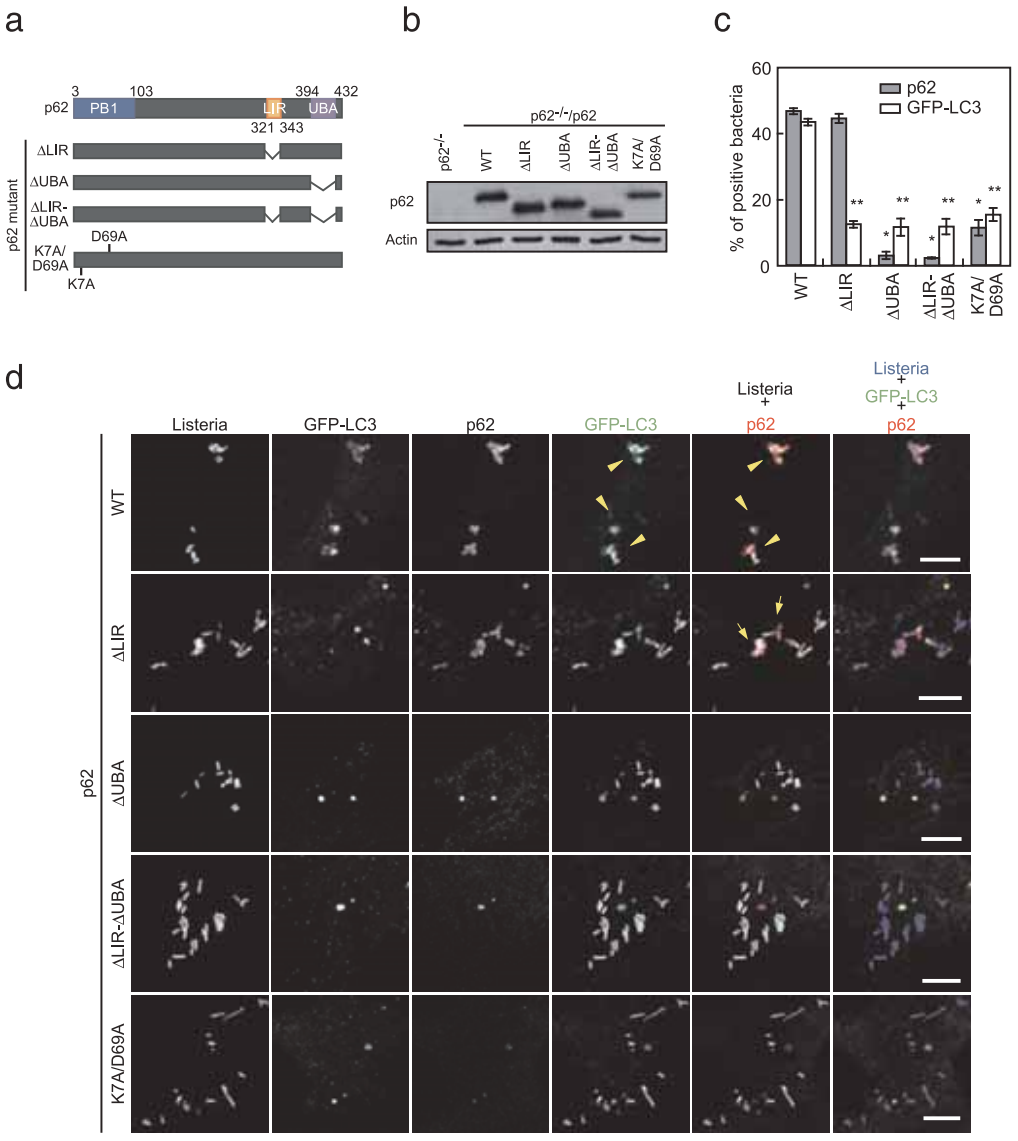

Fig. 7. p62 LIR and UBA domains play pivotal roles in autophagic recognition of Δ*act*A2.
(a) Schematic representation of p62 mutants. The deleted amino acid regions of ΔLIR and ΔUBA are 321-342 and 394-431 respectively. ΔLIR-ΔUBA is deleted 321-342 and 394-431 amino acid regions. K7AD69A is a double amino acid substituted p62 protein. (b) Production of p62-3xMyc mutants in *p62*$^{-/-}$ cells. (c and d) *p62*$^{-/-}$/p62 [wild-type (WT), ΔLIR, ΔUBA, ΔLIR-ΔUBA or K7A/D69A] cells were infected with Δ*act*A2 for 2 h, and stained with anti-Listeria antibody (blue) and anti-Myc antibody (red), and the number of p62-positive or GFP-LC3-positive bacteria was quantified. Data are presented as means ± s.e.m. At least 500 bacteria were counted in each experiment ($n = 3$). *, $p < 0.001$ versus p62-positive, **, $p < 0.001$ versus GFP-LC3-positive bacteria in *p62*$^{-/-}$/p62 (WT) cells, respectively. Scale bars, 10 μm. Arrows indicate p62-positive bacteria. Arrowheads indicate GFP-LC3- and p62-positive bacteria.

reported that autophagy targeted *L. monocytogenes* during primary infection by limiting the onset of early bacterial growth following listeriolysin-dependent vacuole perforation, but preceding active multiplication in the cytosol. Also, it was reported that a *L. monocytogenes* Δ*plcA*Δ*plcB* mutant (deficient in production of the phospholipases, PlcA and PlcB) was targeted more frequently for autophagy, in particular at later time points, i.e. at 2-10 h post infection. Previous studies have shown that the absence of phospholipases from *L. monocytogenes* renders them defective for entry and spread into

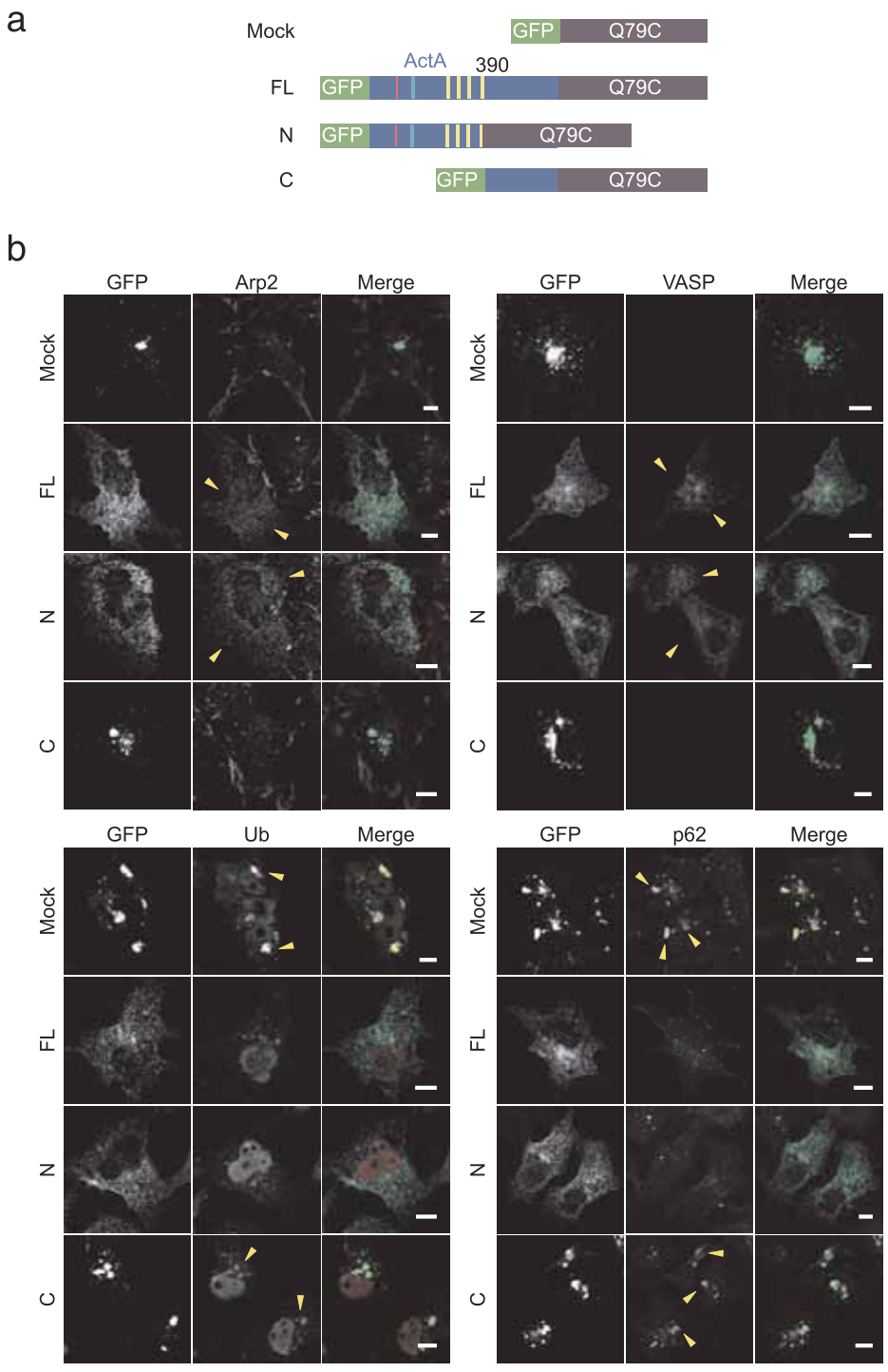

Fig. 8. Biomimetic properties of ActA for GFP-polyQ aggregation.
(a) Schematic representation of the GFP-ActA-Q79C series. FL, N, and C comprise ActA residues 30-612, 30-389, and 390-612, respectively. (b) The series of pEGFP-ActA-Q79C constructs were transfected into COS-7 cells. Cells were fixed with 4% Paraformaldehyde after 18h and stained with anti-Arp2 antibody, anti-VASP antibody, anti-Ub antibody, or anti-p62 antibody (red). Scale bars, 10 μm. Arrowheads indicate Arp2-, VASP-, Ub- or p62-positive.

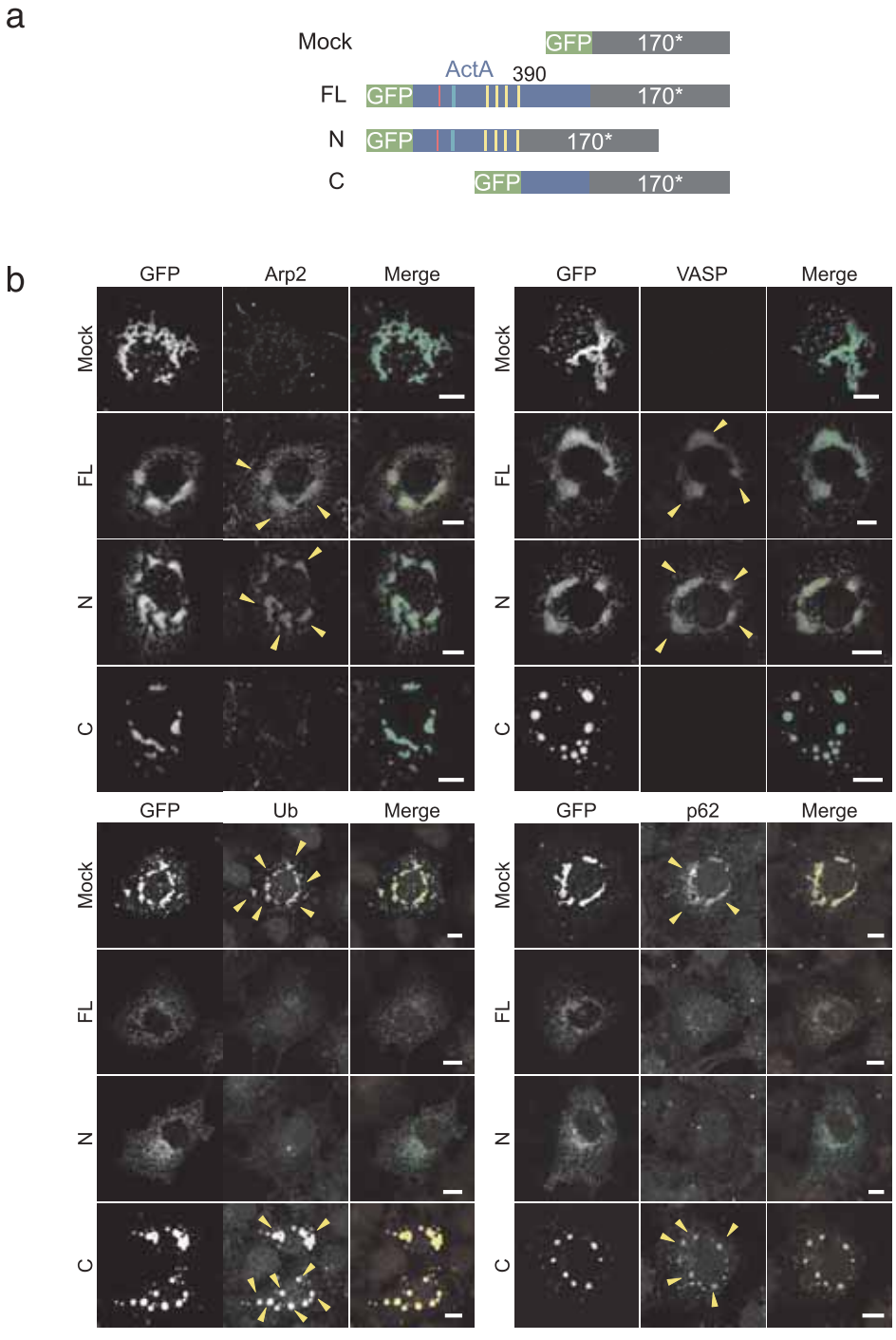

Fig. 9. Biomimetic properties of ActA for GFP-170* aggregation.
(a) Schematic representation of the GFP-ActA-170* series. FL, N, and C comprise ActA residues 30-612, 30-389, and 390-612, respectively. (b) The series of pEGFP-ActA-170* constructs were transfected into COS-7 cells. Cells were fixed with 4% Paraformaldehyde after 14h and stained with anti-Arp2 antibody, anti-VASP antibody), anti-Ub antibody, or anti-p62 antibody (red). Scale bars, 10 μm. Arrowheads indicate Arp2-, VASP-, Ub- or p62-positive.

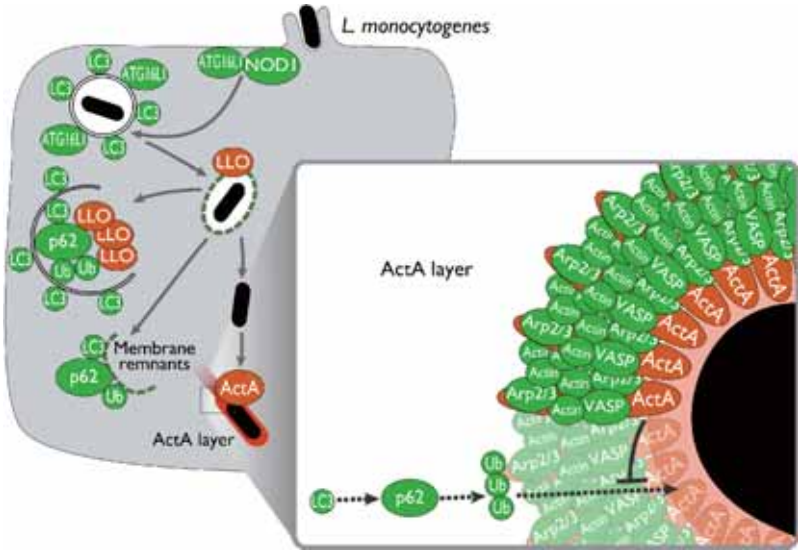

Fig. 10. A model for autophagic recognition of *L. monocytogenes* lacking ActA.
A model for recognition of *L. monocytogenes* infection by host innate immune systems. Infection of host cells by *L. monocytogenes* is recognized by autophagic pathways. The NOD1-ATG16L1-LC3 pathway can sense the bacterial entry site, and vacuolar membrane remnants created by LLO secreted from *L. monocytogenes*. LLO (or LLO-mediated membrane damage) in macrophages can be recognized by the Ub-p62-LC3 pathway, by which LLO may be aggregated and entrapped by autophagosomes. However, wild-type *L. monocytogenes* cannot be recognized by autophagy, because expression of ActA over the bacterial surface recruits the Arp2/3 complex, VASP and actin, and disguises the pathogen from autophagic recognition.

neighboring cells. The abortive transfer of these bacteria from one cell to another leaves them trapped in a double membrane vacuole comprising membranes from donor and recipient host cells, thus increasing their frequency of being autophagocytosed. A recent study described the presence of a subpopulation of variant *L. monocytogenes* forms with lowered listeriolysin O (LLO) activity residing in Spacious *Listeria*-containing Phagosomes (SLAPs), which are autophagosomes-like compartments that do not mature. The authors concluded that SLAPs may represent a stalemate between bacterial LLO action and the host autophagy system, resulting in persistent infection. Thus, autophagy targets *L. monocytogenes* at all phases of its intracellular growth: from its presence in LLO-damaged phagosomes, at early times following escape into the cytosol, and later during PlcB-dependent cell-to-cell spread where the bacterium must exit a multi-layered membrane compartment comprising of components of the previously- and newly- infected cell membranes. Because during primary infection autophagy targets *L. monocytogenes* to limit the onset of early bacterial growth, here we have specifically addressed the mechanism by which the bacterium avoids autophagic recognition at this stage. Thus ActA-dependent interference with autophagic recognition is the key to subsequent active bacterial multiplication in the cytosol. In the present study, we have provided evidence for a novel stratagem whereby cytoplasmic invading *L. monocytogenes* avoids autophagic recognition. The mechanism is disarmingly intuitive: by the simple expedient of exploiting ActA's ability to recruit host cell cytoskeletal proteins, the bacterium disguises itself as a host cell organelle allowing it to survive (Fig. 10). Recent evidence indicates that ActA is a natively unfolded protein that is very densely packed on the bacterial surface. Experimental data derived from cross-linking experiments and calibrated immunofluorescence studies predict that because of this crowding, there is just enough space around a single ActA molecule to engage only one copy of the Arp2/3 complex, one VASP tetramer with four profilactin complexes and the elongation filament to comprise a core motility machinery. Detailed proteome analysis of protein complexes recruited by ActA has revealed

that this core motility machinery is supplemented by additional actin binding proteins, their regulators and potential scaffolding proteins (e.g 14-3-3 proteins) to form even larger macromolecular complexes. Also, recent data from studies with *Drosophila* has pinpointed diaminopimelic acid-type peptidoglycans of *Listeria* as stimulators of the autophagic pathway. As we show here, the biomimetic properties of ActA provides a unique example of an intracellular bacterial survive stratagem to overcome such host innate defense systems.

Conclusion

We have examined current knowledge of the ability of the innate defense system to target *L. monocytogenes* to autophagy, and highlighted bacterial countermeasures against autophagy. Host cells utilize multiple pathways to defeat intruding *L. monocytogenes*, including recognition of PAMPs and DAMPs by NOD1, NALP3, NLRC4 and AIM2 inflammasomes, as well as Ub-p62- LC3-mediated autophagy. In response, *L. monocytogenes* has developed a unique system involving ActA to counteract and escape host innate defense systems. To our knowledge, the use of listerial ActA in two essential intracellular bacterial survival activities, for intracellular motility and intercellular spreading, and the evasion of autophagy, is unique and represents an extension of the fine art of molecular mimicry. Understanding the intricacies of this interaction in a spatio-temporal dimension is likely to generate new information as to how hosts and pathogens sense and translate information for survival.

APOBEC3 deaminates the E2 gene of human papillomavirus-16

Zhe Wang, Kouichi Kitamura, Miki Koura, Satoru Kondo, Tomokazu Yoshizaki, and Masamichi Muramatsu

Department of Molecular Genetics, Division of Otolaryngology, Kanazawa University Graduate School of Medical Science 13-1 Takara-machi, Kanazawa 920-8640, Japan

Introduction

Apolipoprotein B mRNA editing catalytic polypeptide-1 (APOBEC-1) is the founding member of the APOBEC family and an RNA editing deaminase that is responsible for ApoB100 RNA editing. Previously, we identified activation-induced cytidine deaminase (AID) as an APOBEC-1 homolog (1). We further elucidated that AID initiates immunoglobulin class switch recombination and somatic hypermutation by deaminating immunoglobulin genes (2, 3). After the discovery of AID, the size of the APOBEC family rapidly increased, and currently, 11 APOBEC proteins have been identified in the human genome (AID, APOBEC1, 2, A3A, A3B, A3C, A3DE, A3F, A3G, and A3H, APOBEC4). These enzymes catalyze the deamination of cytidine to uracil in DNA and RNA. Experimental evidence accumulated over several years indicates that APOBEC3 proteins not only induce hypermutation in viral genomes such as genomes of HIV-1 and Hepatitis B viruses but also suppress viral replication (4). Despite extensive efforts, both the viral specificity of APOBEC3 and the viral molecules that influence the target specificity of APOBEC3 remain unknown. In vitro studies suggested that APOBEC3 protein preferentially targets single-stranded DNA. Indeed, viruses that rely on reverse transcription for replication such as retroviruses and hepatitis B viruses are good targets for APOBEC3 proteins because they form single-stranded DNA upon reverse transcription. Conversely, other reports suggested that APOBEC3 proteins could affect other viruses as well. Moreover, foreign episomal DNA transfected into cells can be targeted by nuclear-type APOBEC3 proteins (A3A, A3C, and A3H) (5, 6). Human papillomavirus (HPV) is a small DNA virus, and its genomic DNA is maintained as an episome in basal cells of stratified epithelium. Among HPVs, HPV-16 along with HPV-18 is the major causative pathogens of cervical cancer (7). The HPV-16 genome encodes at least eight genes (E6, 7, 1, 2, 4, 5, L1, and 2). E6 and E7 are well-characterized viral oncoproteins that target p53 and retinoblastoma proteins, respectively. Thus, the expression of E6 and E7 proteins may explain how cervical cancer develops after infection. However, it has not been clarified how infected cells continuously express E6 and E7 proteins and finally become transformed. Here, we asked whether APOBEC3 protein could target HPV-16 DNA in an artificial HPV replicon system.

Materials and Methods

Plasmid constructs

p1203, a plasmid that contains one copy of the HPV-16 genome, was purchased from ADDGENE. To eliminate DNA which is not required for HPV-16 early gene expression, a DNA fragment between the *Sal*I and *Stu*I sites was deleted from p1203, and then entire early genes flanked by *Bam*HI and *Sal*I sites were transferred in the *Bam*HI-*Xho*I sites of pcDNA6.2-GW/EmGFP-

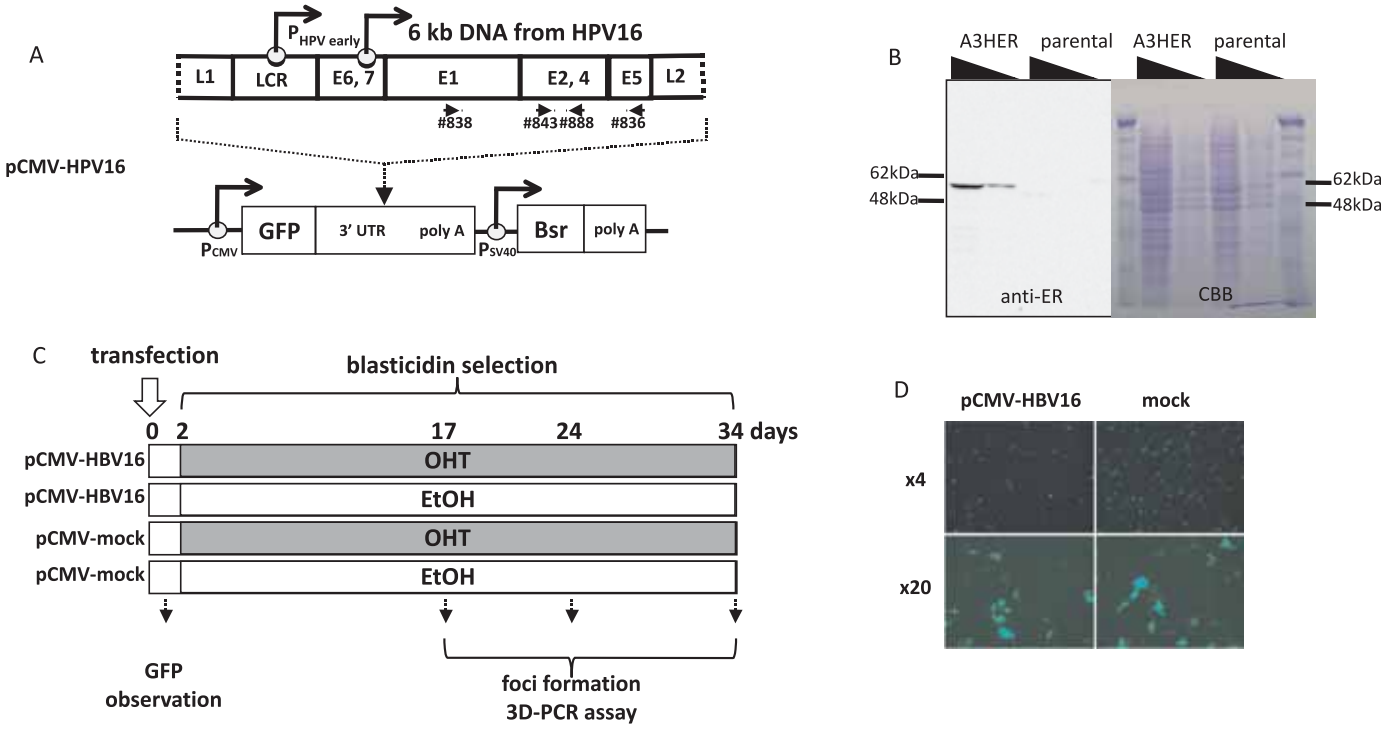

Fig. 1. Experimental design.
(A) Design of the HPV-16 replicon plasmid. The HPV-16 replicon (pCMV-HBV-16) contains the early gene expression cassette that spans from the C-terminus of L1 gene to the N-terminus of L2 gene in the middle of 3′-untranslated region of GFP gene. Blasticidin resistance gene in pCMV HBV-16 can be used as a genetic marker in cells that possess the pCMV HPV-16 replicon. The positions of primers for Fig. 2B and 3D-PCR are also indicated.
(B) Expression of the human APOBEC3H (A3H)-ER fusion protein. A3H-ER gene was transfected retrovirally into Huh7 human hepatocellular carcinoma cells. After puromycin selection, A3H-ER protein expression was confirmed by western blotting using an anti-ER antibody. Coomassie brilliant blue staining was also used to estimate the amount of protein per lane. Parental Huh7 cells were used as a negative control.
(C) Experimental scheme is shown. Two days after transfecting either pCMV-HPV-16 or pCMV-mock, blasticidin was added in combination of 1 μM OHT or EtOH. The retention of HPV DNA was estimated by the survival of cells in blasticidin-containing medium. The presence of hypermutated HPV DNA was assessed in the samples from days 17, 24, and 34.
(D) GFP expression 1 day after transfection. GFP expression with similar frequency between experimental groups was observed.

miR (Invitrogen). The plasmid was named pCMV HPV-16. An APOBEC3H-ER–expressing retroviral vector was constructed by exchanging an open reading frame of AID in pFBmAIDERpuro (8) with one for human APOBEC3H.

The establishment of A3HER-expressing cells by retroviral transfection was performed as described previously (8, 9). The expression of A3HER was confirmed by western blotting with an anti-ER antibody (Santa Cruz, sc-543). Cells were maintained in DMEM containing 10% FBS and supplemented with 100 U/ml penicillin and 100 μg/ml streptomycin.

Extraction of DNA and detection of hypermutation by 3D-PCR

Episomal DNA was extracted by Hirt extraction with a minor modification (10). 3D-PCR was performed by a modification of a previously published method (11, 12). The HPV-16 genomic DNA sequence

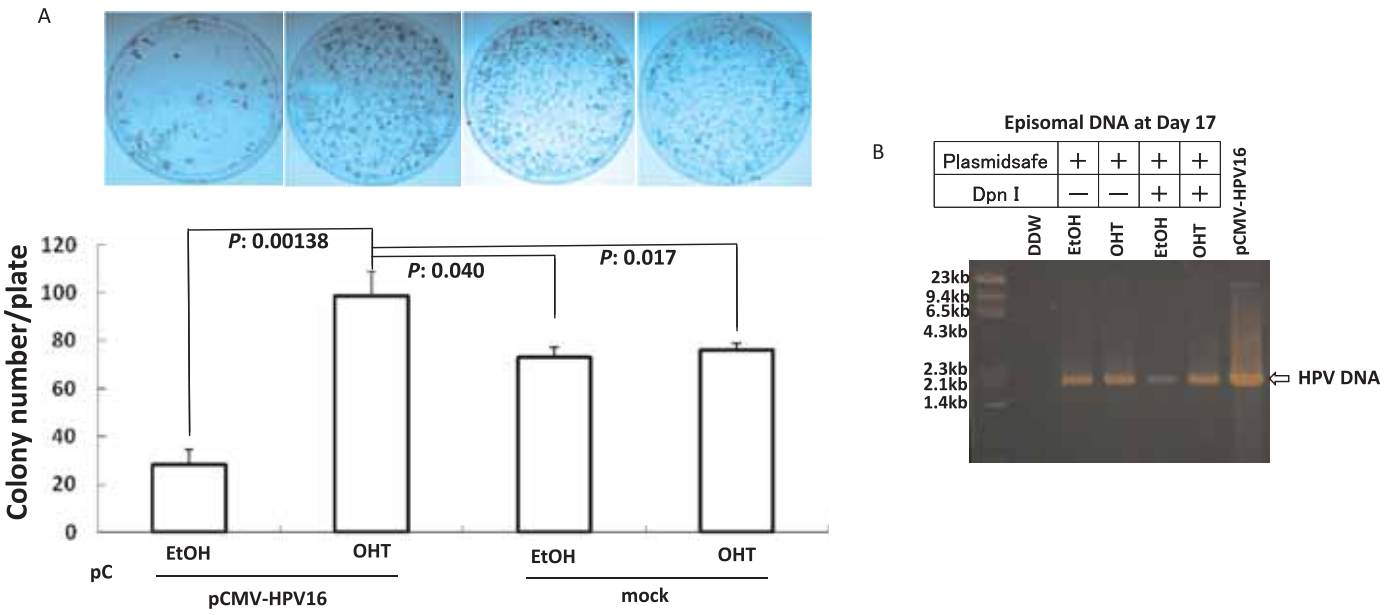

Fig. 2. Replication of pCMV HPV-16

(A) Survival rate of cells transfected by pCMV-HPV-16

Cells depicted in Fig. 1C were cultured in medium containing blasticidin. A3HER cells (0.6×10^6) were transfected with the indicated plasmids. Two days after transfection, cells were divided into three 10-cm dishes. Surviving colonies on day 34 were stained with Giemsa (top). The number of surviving colonies per dish was counted (bottom).

(B) On day 17, the replication of episomal DNA was assessed by PCR. Episomal DNA was extracted by Hirt extraction and double-digested by *Dpn*I, a methyl DNA specific restriction enzyme, and Plasmidsafe, a DNA-end specific exonuclease. After *Dpn*I and Plasmidsafe digestion, the replicating episomal DNA of pCMV HPV-16 was detected by PCR. Non-treated pCMV-HPV-16 plasmid was used as a positive control for PCR (extreme right lane).

NC_001526 was used as a reference sequence. The primers used here were as follows: #838, CAGACA CTAATAGTAATGCAAG; #888, CGTCCTTTGTGT GAGCTGTTAAAT; #843, TCCTGAAATTATTAGG CAGCACTT; and #836, AGCGGACGTATTAATAG GCAGA.

Results and Discussion

Because no small animal models or in vitro culture systems have been established to study the replication of HPV excluding some exceptional experimental protocols, we attempted to observe a relationship between APOBEC3 and HPV-16 by introducing an artificial HPV plasmid into APOBEC3H (A3H)-expressing cells. A3H was chosen as a representative nuclear-type APOBEC3 protein that potentially affects episomal viral DNA. We previously demonstrated that AID, a nuclear-type APOBEC protein, may mutate cellular genomic gene loci such as c-myc gene (13). It is possible that continuous overexpression of nuclear APOBEC3H affects general cellular homeostasis. To avoid such potential harmful effects of A3H overexpression, we applied a tamoxifen (OHT)-inducible system in which the ligand-binding domain of the estrogen receptor and A3H was fused in frame, and the fusion protein of A3H-ER was expressed as an inactive form. In this system, the A3H-ER fusion protein can be activated by the addition of OHT to the culture medium (9). A3HER protein expression was confirmed by western blotting (Fig. 1B)

The expression of two HPV oncoproteins, E6 and E7, is essential to understand HPV-induced tumorigenesis, and the HPV early promoter has a primary role in regulating E6 and E7 gene expression. Thus, the entire early expression cassette of HPV-

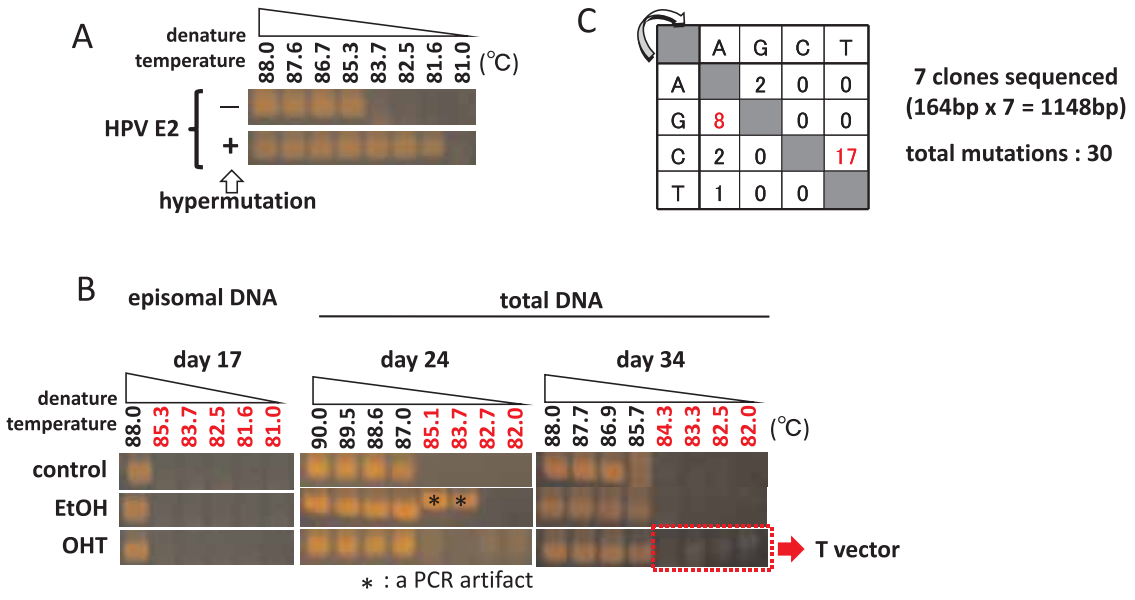

Fig. 3. Detection of hypermutated DNA from HPV-16 DNA

(A) Calibration of 3D-PCR for HPV-16 E2 gene. 3D-PCR was performed with authentic HPV E2 DNA containing four C-to-T mutations (indicated by +) or no mutations (indicated by -). The results indicated that the 3D-PCR protocol could differentially amplify hypermutated HPV-16 E2 DNA if the target DNA contained more than four C-to-T mutations.

(B) Detection of hypermutation in A3H-activated cells. Episomal and total DNA were extracted from A3H-ER-transfected cells that were cultivated in the medium containing blasticidin and OHT (or EtOH) for the indicated periods. 3D-PCR was performed to detect hypermutated HPV DNA.

Hypermutated DNA detected by 3D-PCR (highlighted with a dotted box) was purified and cloned into a T vector, and seven clones were sequenced. The results are summarized in C and D. DNA sequencing revealed signals that migrated slower (star symbols) to be PCR artifacts. C, Mutation preference was demonstrated. DNA for signals highlighted by a red box was subcloned into a T vector, and seven recombinant clones were sequenced. Overall, 30 point mutations were detected.

16, which spans from the HPV early promoter to the poly A signal, was inserted into the 3′-untranslated region of GFP gene (Fig. 1A). The plasmid was designated pCMV HPV-16. pCMV HPV-16 is expected to express at least two types of HPV-16 transcripts: one from the CMV promoter and one from the HPV early promoter. As entire genes that support early viral replication are included, pCMV HPV-16 may partially mimic the early replication of HPV-16. pCMV HPV-16 and its mock vector were transfected into A3HER-expressing cells, and after the confirmation of GFP expression in transfected cells (Fig. 1D), blasticidin was added to eliminate nontransfected cells in the presence or absence of OHT for the indicated periods in Fig. 1C. In this system, the survival rate under blasticidin selection is directly correlated with the retention of the blasticidin resistance gene that is tandemly located in the vector (Fig. 1A). On day 32 after blasticidin addition, surviving colonies were counted (Fig. 2A). Survival was slightly higher in OHT-stimulated and pCMV-HPV-16 transfected cells than in control cells. Unexpectedly, mock-transfected cells also produced significant numbers of surviving colonies. No colonies developed from nontransfected cells (data not shown). The data suggest that blasticidin resistance partially depends on both A3H activity and HPV DNA, and the transfection of a mock plasmid containing blasticidin resistance gene is sufficient to confer blasticidin resistance. To determine the physical status of episomal HPV DNA, episomal DNA on day 17 was extracted by a standard method. The episomal DNA fraction may contain residual plasmids used

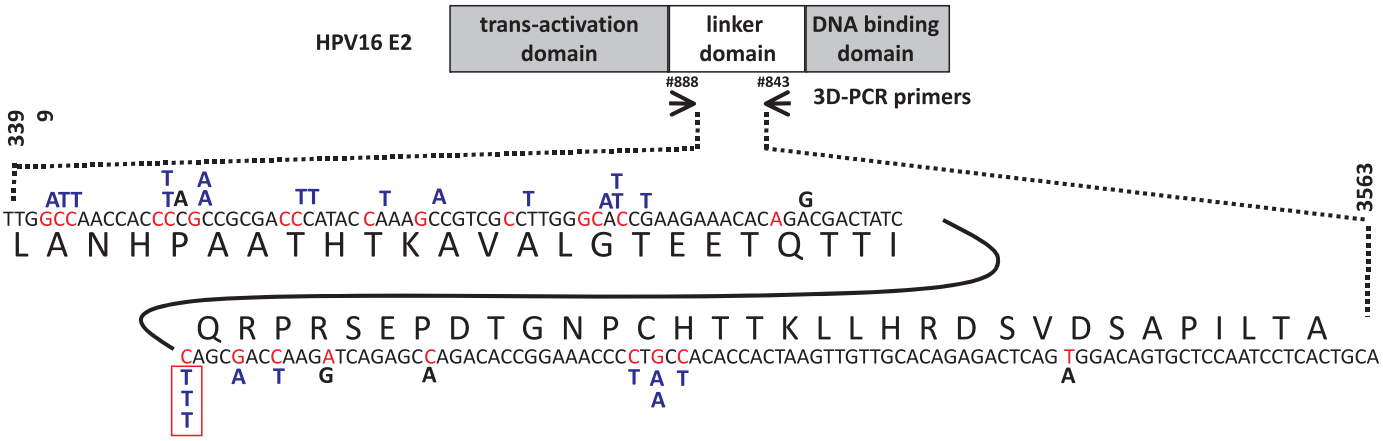

Fig. 4. Structure of HPV-16 E2 and the positions of mutations. E2 is functionally divided into three domains as indicated. The target DNA region for 3D-PCR is enlarged below. All of the mutations of the seven clones were plotted against the reference sequence. Mutations that create a premature stop codon in an open reading frame of E2 gene are indicated by a red box.

for transfection, and thus, we treated the episomal DNA fraction with *Dpn*I endonuclease to eliminate contaminating plasmids. The episomal DNA fraction was further treated with Plasmidsafe, a linear DNA-specific exonuclease that eliminates DNA fragments digested by *Dpn*I. Even after double digestion with *Dpn*I and Plasmidsafe, a 2.2-kb HPV-16 E2 gene was clearly amplified from the episomal DNA fraction by PCR, indicating that pCMV HPV-16 replication does occur in A3H-ER-transfected cells at least until day 17 (Fig. 2B).

The accumulation of C-to-T (and G-to-A) mutations in HPV DNA was assessed by 3D-PCR. 3D-PCR is a powerful method to detect G-to-A and C-to-T hypermutation. As hypermutation increases AT content in a given DNA sequence, the hypermutated DNA melts at a lower denaturation temperature than wild-type DNA, and therefore, the hypermutated DNA is consequently detected by PCR even if the PCR protocol uses a lower temperature such as 82°C for the denaturing step. We used E2 gene as a target DNA sequence for 3D-PCR because it contains more G and C nucleotides than any other region of the early expression genes of HPV-16. To verify the sensitivity of 3D-PCR to detect hypermutated DNA in E2 gene, wild-type and hypermutated E2 DNA were amplified simultaneously by 3D-PCR. Figure 3A shows that hypermutated DNA containing four C-to-T mutations was amplified using denaturation temperatures as low as at 81.6°C, whereas a temperature of 85.3°C was required to amplify wild-type E2 DNA. HPV DNA from three experimental conditions (days 17, 24, and 34) was assessed by 3D-PCR. Signals were observed using HPV DNA from cells treated with OHT for 24 and 34 days with denaturation temperatures as low as 82°C, suggesting hypermutation in HPV DNA induced by A3H protein. The episomal DNA recovered on day 17 did not exhibit hypermutated signals. The DNAs amplified at the lower denaturation temperature on days 24 and 34 were excised and cloned into a T vector. Seven clones were randomly chosen for DNA sequencing. All seven clones contained at least two C-to-T or G-to-A mutations, and the average C-to-T and G-to-A mutation load per clone was 3.5; this cannot be explained by DNA polymerase errors during PCR amplification because polymerase errors occur much less frequently and relatively randomly. Regarding total DNA samples harvested on days 24 and 34, both types of DNA, episomal and integrated DNA, may be present in the host genome. This idea is supported by experiments in which integrated loci were easily identified from those total DNA samples by inverted PCR (14) (data not shown). This study was unable to discriminate the types of HPV DNA that contain hypermutated E2 genes. In total, 23 out of 30 mutations were either missense or nonsense mutations (Fig. 4),

suggesting mild bias to mutations that may reduce E2 gene function.

Conclusions

In this study, we transfected A3H-expressing cells with an artificial HPV replicon plasmid that mimics HPV early replication. Hypermutation frequencies were compared in the presence and absence of A3H activity. The 3D-PCR assay revealed A3H-dependent hypermutation on E2 gene, which is frequently used during the integration of HPV DNA into host genomes upon oncogenesis. It has been proposed that deamination by APOBEC in DNA creates uracil bases, and then the base excision repair pathway generates DNA strand breaks in the process of repairing mutated DNA. DNA stand breaks may potentially trigger recombination between HPV DNA and host genomic DNA. Most APOBEC3s are reported to be transcriptionally upregulated during viral infection. Therefore, we propose that nuclear-type APOBEC3 proteins facilitate HPV DNA integration. Further investigation is needed to clarify the roles of APOBECs in HPV pathogenesis.

References

(1) Muramatsu, M., Sankaranand, V. S., Anant, S., Sugai, M., Kinoshita, K., Davidson, N. O., and Honjo, T. (1999) *J Biol Chem* **274**, 18470-18476.

(2) Muramatsu, M., Kinoshita, K., Fagarasan, S., Yamada, S., Shinkai, Y., and Honjo, T. (2000) *Cell* **102**, 553-563.

(3) Muramatsu, M., Nagaoka, H., Shinkura, R., Begum, N. A., and Honjo, T. (2007) *Adv Immunol* **94**, 1-36.

(4) Strebel, K., Luban, J., and Jeang, K. T. (2009) *BMC Med* **7**, 48.

(5) Vartanian, J. P., Guetard, D., Henry, M., and Wain-Hobson, S. (2008) *Science* **320**, 230-233.

(6) Stenglein, M. D., Burns, M. B., Li, M., Lengyel, J., and Harris, R. S. (2010) *Nat Struct Mol Biol* **17**, 222-229.

(7) Stanley, M. A., Pett, M. R., and Coleman, N. (2007) *Biochem Soc Trans* **35**, 1456-1460.

(8) Nagaoka, H., Ito, S., Muramatsu, M., Nakata, M., and Honjo, T. (2005) *Proc Natl Acad Sci U S A* **102**, 2022-2027.

(9) Doi, T., Kinoshita, K., Ikegawa, M., Muramatsu, M., and Honjo, T. (2003) *Proc Natl Acad Sci U S A* **100**, 2634-2638.

(10) Hirt, B. (1967) *J Mol Biol* **26**, 365-369.

(11) Suspene, R., Guetard, D., Henry, M., Sommer, P., Wain-Hobson, S., and Vartanian, J. P. (2005) *Proc Natl Acad Sci U S A* **102**, 8321-8326.

(12) Bonvin, M., Achermann, F., Greeve, I., Stroka, D., Keogh, A., Inderbitzin, D., Candinas, D., Sommer, P., Wain-Hobson, S., Vartanian, J. P., and Greeve, J. (2006) *Hepatology* **43**, 1364-1374.

(13) Okazaki, I. M., Hiai, H., Kakazu, N., Yamada, S., Muramatsu, M., Kinoshita, K., and Honjo, T. (2003) *J Exp Med* **197**, 1173-1181.

(14) Kalantari, M., Chase, D. M., Tewari, K. S., and Bernard, H. U. (2010) *J Med Virol* **82**, 311-320.

Preparation of amphotericin B nanoparticles for deep mycosis and the formulation optimization based on physicochemical and biodistributional characterization

Kunikazu Moribe

Department of Pharmaceutical Technology, Graduate School of Pharmaceutical Sciences, Chiba University, Chiba 260-8675, Japan

Introduction

Nano-sized drug carriers have been developed as drug delivery systems. Liposomes, micelles, and nanospheres have been widely investigated for the selective accumulation at the target site. Encapsulation of an active pharmaceutical ingredient (API) can be a hurdle when formulating nanoparticles. In the case of polymeric micelles or nanospheres, selecting appropriate excipients is important for miscibility or specific interaction with the API. An antioxidant is usually loaded to a nanoparticle formulation to prevent oxidation of the API as well as of carrier components. Ascorbic acid is a widely used hydrophilic antioxidant. However, since ascorbic acid is unstable in water, many ascorbic-acid derivatives have been synthesized (1-3). Ascorbic acid 2-glucoside (AA-2G), which is a newly approved food additive, can be used to solubilize APIs (4). A variety of alkyl chains that linked with ascorbic acid can be used to improve surface activity. Ascorbyl monoalkylated derivatives, such as ascorbyl palmitate, can be used to develop micelles, microemulsions, and liposomal formulations. l-Ascorbyl 2,6-dipalmitate (ASC-DP) is a fatty ester derivative of ascorbic acid, with extremely low water solubility. The antioxidant has been used in cosmetics (5). Compared with ascorbyl palmitate, ASC-DP cannot form micelles or liposomal structures on its own. However, the ASC-DP/distearoylphosphatidylethanolamine polyethylene glycol 2000 (DSPE-PEG) complex forms stable nanoparticles. In this study, drug-containing ASC-DP/DSPE-PEG nanoparticles were prepared. Amphotericin B (AmB), a polyene macrolide antibiotic drug used for systemic invasive fungal infection, specifically interacts with DSPE-PEG (6). The intermolecular interaction is believed to contribute to effective AmB incorporation into the ASC-DP/DSPE-PEG nanoparticles. Stability, toxicity, and blood residence of the AmB/ASC-DP/DSPE-PEG nanoparticles, as well as the structural evaluation were investigated for formulation optimization based on physicochemical and biodistributional characterization.

Materials and Methods

Materials

ASC-DP was obtained from Tokyo Chemical Industry, Co. Ltd., Japan. DSPE-PEG was purchased from NOF corporation (Japan). AmB were obtained from Wako Pure Chemicals (Japan). The chemical structures are shown in Fig. 1. Other chemicals were of reagent grade and used without further purification.

Preparation of ASC-DP/DSPE-PEG or AmB/ASC-DP/DSPE-PEG nanoparticles

ASC-DP and DSPE-PEG dissolved in chloroform were mixed at the molar ratio of 1:1. To prepare AmB-incorporated samples, AmB dissolved in methanol was added to the chloroform solution. The solvent

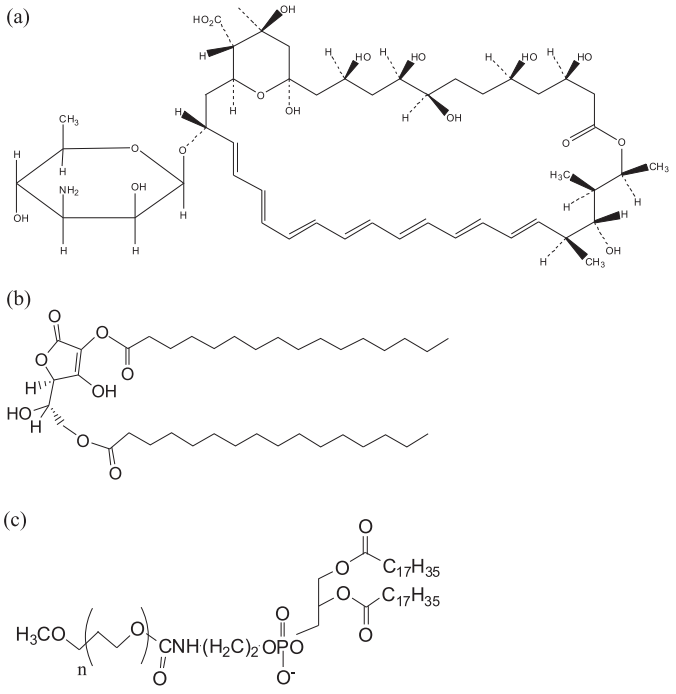

Fig. 1. Chemical structure of (a) amphotericin B (AmB), (b) ascorbyl 2,6-dipalmitate (ASC-DP), and (c) distearoylphosphatidylethanolamine polyethylene glycol 2000 (DSPE-PEG).

was evaporated with a rotary evaporator and further removed by drying in a desiccator under reduced pressure for 12 h. The film that formed on the pear-shaped flask was hydrated with water to prepare nanosuspensions.

Particle size analysis

The mean particle size of the nanoparticles was determined with the dynamic light-scattering method, using Microtrac UPA® (Nikkiso, Japan; measurement range: 0.003–6μm).

Stability study

Stability studies of sample solutions were conducted during the particle size analysis after the storage at 25°C for a definite time period.

Zeta potential measurement

A zeta potential for each suspension was determined using NICOMP 380ZLS® (Agilent Technologies Inc., USA). The measurements were repeated 3 times, and average values were calculated.

Experimental animals

For the in vivo toxicity experiment, male ddY mice (11–12 weeks old) were obtained from Japan SLC, Inc. (Japan). Male ddY mice (7 weeks old) were used for blood concentration measurement. The mice were fed and given water ad libitum prior to the experiments.

Acute toxicity

The AmB/DSPE-PEG micelle solution and AmB/ASC-DP/DSPE-PEG nanoparticle suspension were prepared according to the hydration method mentioned above, except that sample films were hydrated with 9% sucrose solution to keep the isotonic condition and prevent AmB precipitation (6). Sample solutions including Fungizone® were intravenously administered from mice tail vein in increasing doses of AmB (0.5, 1, 2, 3, 4, 8, 10, and 12 mg/kg). To determine the minimum lethal dose (MLD), which was defined as the minimum dose that produces death in all mice, survival was checked for 3 h after injection.

Blood residence in vivo

Fungizone® and the AmB/ASC-DP/DSPE-PEG nanoparticle suspension were intravenously injected to the mice via the tail vain at a dose of 1.0mg AmB/kg body weight. At desired time intervals, blood samples were collected from the anesthetized mice by cardiac puncture, and serum samples were separated by centrifugation. The serum sample (500 μL) was mixed with an extracting reagent (10-mM phosphate buffer, pH 7.4, 1 mL), an internal standard solution (4-nitro-1-naphthylamine, 10 μg/mL, 1.0 mL), and methanol (3.0 mL). Serum proteins were separated by centrifugation. The AmB in the serum was extracted from the supernatant using C18 BOND-ELUT® (Varian, CA, USA), eluted with 1.0mL of acetonitrile-2.5 mM Na2EDTA (60/40,

v/v), and measured by means of high-pressure liquid chromatography. A Wakosil C18 column (4.6 mm × 150 mm, Wako Pure Chemicals, Japan) was used, and the mobile phase was acetonitrile—10 mM AcOH (pH 4.0) (11/17, v/v) with a flow rate of 0.7 mL/min. AmB and the internal standard had retention times of 6.0 and 9.0 min, respectively. The absorbance of the column effluent was measured at 385 nm. The area under the plasma concentration–time curve (AUC) value (0–4 h) of the plasma profiles was calculated using logarithmic and linear trapezoidal rules. P values were calculated using the F-test ($p = 0.023$) and t-test ($p = 0.036$), and values less than 0.05 were considered significant.

Atomic force microscopy (AFM)

Atomic force microscope (MPF-3D, Asylum Research, USA) was used to observe morphology of colloidal probucol nanoparticles. A silanized mica was prepared by dropping 0.1% of 3-aminopropyltriethoxysilane (APTES) solution onto a mica surface. After storing it for 30 min at room temperature, excess amount of APTES was washed with water. The positively charged mica surface can easily immobilize the negatively charged drug nanoparticles. The sample suspensions were dropped onto the silanized mica to immobilize them onto the surface. Alternative contact mode atomic force microscopy was performed in the liquid environment. A silicon cantilever (BL-RC150VB-C1, OLYMPUS, Japan) was used for the observation. The AFM topography image, which reflects topographic features of the surface, was obtained from the amplitude change of the cantilever oscillation.

Freeze-fractured transmission electron microscopy (FF-TEM)

Particle shape and particle surface conditions in frozen media were observed by freeze-fractured transmission electron microscopy (JEM-1011, JEOL, Japan). Sample suspension was frozen by using slush nitrogen and fractured using the apparatus (JFD-9010, JEOL, Japan). After shadowing the fractured sample using platinum and the subsequent carbon vapor deposition, the sample replica was prepared by washing the specimen using chloroform and methanol.

Results and Discussion

Physicochemical properties of AmB/ASC-DP/DSPE-PEG nanoparticle

The mean particle size and zeta potential of AmB/ASC-DP/DSPE-PEG nanoparticles are shown in Table 1. Entrapment efficacy of AmB, which was evaluated by passing the sample solution through 0.8 μm filter, was more than 99% in each sample. Compared with the ASC-DP/DSPE-PEG nanoparticles, the mean particle size increased when AmB was incorporated. Particle size also increased with the amount of AmB incorporated. AmB-loaded nanoparticles were stable for at least 24 h. The zeta potential of the AmB-loaded nanoparticles remained negative. Surface charge of particle contributes to the electrostatic repulsion between particles dispersed in water. PEG aqueous layer formed on the particle surface avoids the contact between particles. It was speculated that the surface charges and PEG coverage may contribute to the stable nanoparticle formation.

Toxicity tests in animal models

The main adverse reactions to AmB formulations were hepatic and renal disorders. Acute toxicity was evaluated in terms of MLD. Table 2 shows the MLD of the AmB/ASC-DP/DSPE-PEG nanoparticles, AmB/DSPE-PEG micelle, and Fungizone® ($n = 3–5$). The MLD of the AmB (10 mol%)/ASC-DP/DSPE-PEG nanoparticles was 10 mg/kg, which was more than 3 times that of Fungizone® (3 mg/kg) and the AmB (10 mol%)/DSPE-PEG micelles (2 mg/kg). When an unstable micelle formulation is administered intravenously, it is degraded by dilution and the subsequent drug release, following which drug aggregation occurs. It was speculated that degradation of the unstable AmB/DSPE-PEG micelles and aggregation of the released AmB appeared to be why the AmB/DSPE-PEG micelles had the highest toxicity. AmB (10 mol%)/ASC-DP/DSPE-PEG

Table 1. Mean particle size and zeta potential of ASC-DP/DSPE-PEG and AmB/ASC-DP/DSPE-PEG nanoparticles.

Sample	Mean particle size[a] (nm)	Zeta potential[b] (mV)
ASC-DP/DSPE-PEG	113 ± 12	−39.0 ± 4.3
AmB (1 mol%)/ASC-DP/DSPE-PEG	122 ± 8	−37.2 ± 1.4
AmB (5 mol%)/ASC-DP/DSPE-PEG	157 ± 3	−32.6 ± 0.6
AmB (10 mol%)/ASC-DP/DSPE-PEG	163 ± 5	−33.9 ± 0.4

Entrapment efficacy of AmB, which was evaluated by passing the sample solution through 0.8-mm filter, was more than 99% in each samples.
[a] Samples were hydrated and stored for 24 h. Mean ± SD, n = 3.
[b] Mean ± SD, n = 5.

Table 2. The minimum lethal dose of AmB/ASC-DP/DSPE-PEG nanoparticles, AmB/DSPE-PEG micelle, and Fungizone® (n = 3 − 5).

	Injected dose(mg AmB/kg body)
AmB (10 mol%)/ASC-DP/DSPE-PEG	10.0
AmB (10 mol%)/DSPE-PEG	2.0
AmB (5 mol%)/ASC-DP/DSPE-PEG	4.0
Fungizone®	3.0

nanoparticles was expected to be stable after the injection, however, MLD of the AmB (5 mol%)/ASC-DP/DSPE-PEG nanoparticles (4 mg/kg) was apparently lower than that of AmB (10 mol%) nanoparticles. The unexpected results indicated that incorporation of AmB contributed to the stability of nanoparticle and the subsequent drug release.

Blood residence of AmB

Blood residence of AmB in nanoparticles and in Fungizone® was compared. Fig. 2 shows the plasma concentration–time profile of AmB after mice were intravenously administered the AmB/ASC-DP/DSPE-PEG nanoparticles or Fungizone® at the same dose of 1.0 mg/kg. As compared with the rapid disappearance of AmB after Fungizone® was administered, AmB administered in the form of AmB (10 mol%)/ASC-DP/DSPE-PEG nanoparticles was eliminated slowly from the plasma, with a half-life of 1.2 h. The plasma level of AmB with the AmB (10 mol%)/ASC-DP/DSPE-PEG nanoparticles was always higher than that with Fungizone® at the corresponding time. A significant increase in AUC was observed

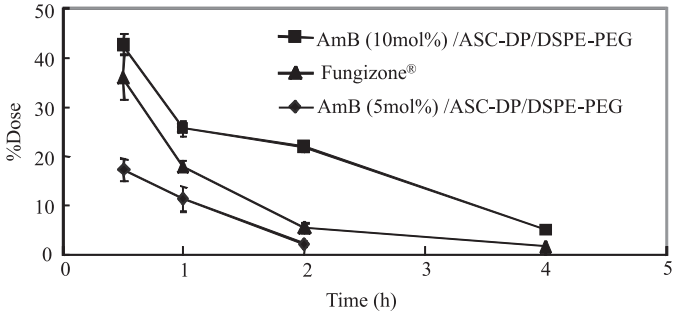

Fig. 2. Plasma concentration of AmB after intravenous administration of AmB/ASC-DP/DSPE-PEG nanoparticles or Fungizone® at a dose of 1.0mg/kg to mice.
Each point represents the mean ±S.D. (n=3∼5).

with the AmB/ASC-DP/DSPE-PEG nanoparticles as compared with Fungizone® ($p < 0.05$). These results suggest that the AmB (10 mol%)/ASC-DP/DSPE-PEG nanoparticles play a role in delaying the disappearance of AmB from tissues such as the liver and kidney. The presence of PEG on the surface of nanoparticles may contribute to the increased blood residence of the drug. On the basis of these results, the ASC-DP/DSPE-PEG nanoparticles appear to be a candidate of AmB carrier.

On the contrary, AmB administered in the form

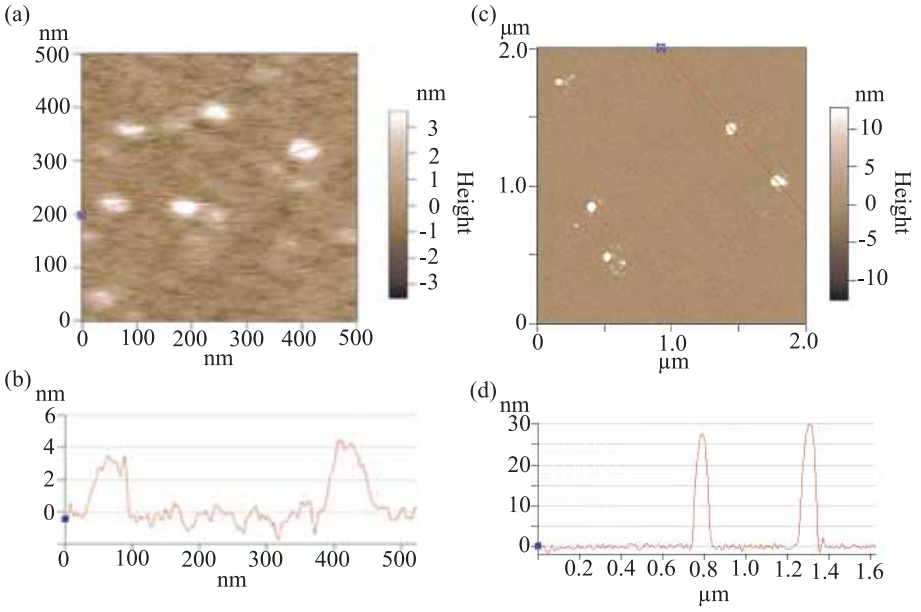

Fig. 3. AFM image (a, c) and cross section profile (b, d) of AmB (5 mol%: a, b)- and AmB (10 mol%: c, d)- loaded nanoparticles in aqueous environment.

of AmB (5 mol%)/ASC-DP/DSPE-PEG nanoparticles was eliminated rapidly from the plasma. The AUC was also lower than that of Fungizone®. Composition of the ternary components as well as intermolecular interactions among the components influenced the structure and stability of the nanoparticles. Combined with the results of MLD, AmB-content dependent structural difference of AmB nanoparticles was expected.

Physicochemical characterization of AmB/ASC-DP/DSPE-PEG nanoparticles

To investigate the reason why the significant differences of blood residence curves were observed, structure of nanoparticles was evaluated by AFM and FF-TEM. Figure 3 shows AFM images of AmB (5 mol%)- and AmB (10 mol%)- loaded nanoparticles. In AmB (5 mol%)- loaded nanoparticle, very thin disk- or lamellar-like structures were observed. The diameter was ca. 100 nm and the height was ca. 4 nm. The structure should be based on ASC-DP and DSPE-PEG complex. Though it is difficult to distinguish the location of AmB, it must be interacted with DSPE-PEG to form the stable complex. On the other hand, in AmB (10 mol%)-loaded nanoparticle, spherical particles with the size of ca. 30 nm were observed. From particle size measurements by DLS, nanoparticles with the size of ca 150 nm were observed. It was speculated that primary drug nanoparticles with the size of ca 30 nm were agglomerated to form secondary nanoparticles in aqueous media. Compared with the nanostructures between AmB (5 mol%)- and AmB (10 mol%)-loaded nanoparticles, excess amount of AmB in AmB (10 mol%)-loaded nanoparticles contribute to form stable primary nanoparticles.

Figure 4 shows FF-TEM images of AmB (5 mol%)- and AmB (10 mol%)- loaded nanoparticles. In AmB (5 mol%)-loaded nanoparticles, disk-like and worm-like structures were observed. Compared with particle sizes evaluated by dynamic light scattering, the worm-like structures observed by TEM were larger. The ternary components might be aggregated during process of freezing. These results suggested that AmB (5 mol%)-loaded nanoparticle demonstrated soft and flexible structures in water. In AmB (10 mol%)-loaded nanoparticles, spheres of more than 100nm were observed. It can be seen that each sphere is composed of agglomerated primary particles, which was observed by AFM shown in Fig. 3.

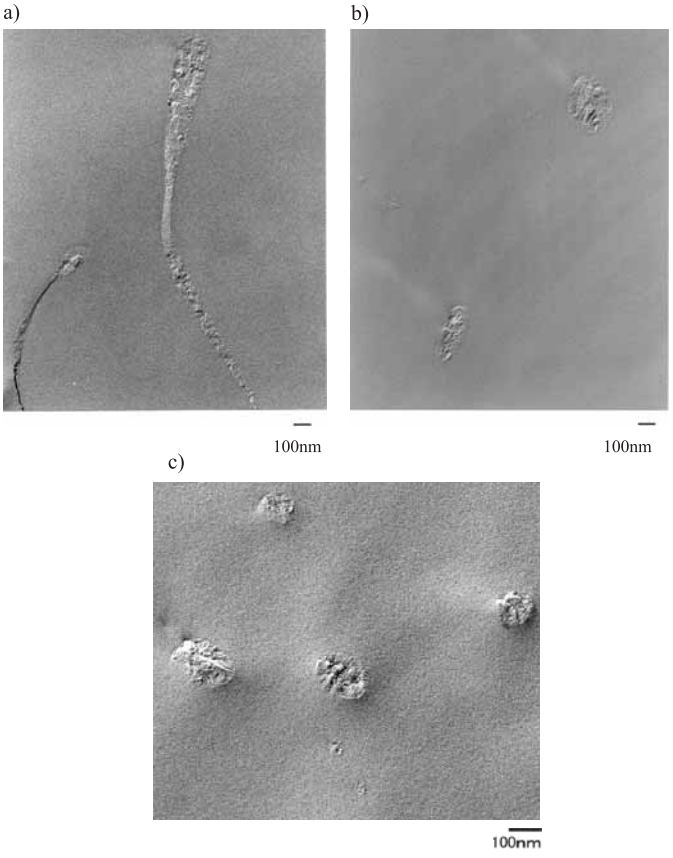

Fig. 4. Freeze fracture-TEM images of AmB (5 mol%: a,b)- and AmB (10 mol%: c)- loaded nanoparticles.

From these results, proposed structures of these nanoparticles are as follows: In AmB (5 mol%)-loaded nanoparticle, AmB, ASC-DP and DSPE-PEG interacted and formed bilayer or unilamellar structure. On the other hand, AmB (10 mol%)-loaded nanoparticles were consisted of spherical primary particles with the size of ca 0 nm. It was concluded that structural difference of AmB-loaded nanoparticles is likely to be the reason why the blood residence was different.

Conclusion

Combining ASC-DP and DSPE-PEG enabled stable nanoparticle formation. AmB was successfully loaded onto the optimized ASC-DP/DSPE-PEG nanoparticle system. Compared with Fungizone®, a solubilized AmB formulation with sodium deoxycholate, the toxicity and blood residence of AmB (10 mol%)-loaded nanoparticles was significantly better when administered intravenously to mice. However, toxicity and blood residence of AmB (5 mol%)-loaded nanoparticles was pretty worse because of the structural differences evaluated by AFM and FF-TEM. ASC-DP incorporation is believed to contribute not only to stabilization of the nanoparticles but also to the antioxidation property of the formulation. In conclusion, ASC-DP/DSPE-PEG nanoparticles combined and stabilized with drug appear to be a promising delivery system for hydrophobic drugs.

References

(1) LoNostro, P., Capuzzi, G., Pinelli, P., Mulinacci, N., Romani, A., Vincieri, F.F., 2000. Self-assembling and antioxidant activity of some vitamin C derivatives. Colloid. Surf. Physicochem. Eng. Aspect. **167**, 83–93.

(2) Teeranachaideekul, V., Junyaprasert, V.B., Souto, E.B., Müller, R.H., 2008. Development of ascorbyl palmitate nanocrystals applying the nanosuspension technology. Int. J. Pharm. **354**, 227–234.

(3) Moribe, K., Limwikrant, W., Higashi, K., Yamamoto, K., 2011. Drug nanoparticle formulation using ascorbic Acid derivatives. J Drug Deliv. 2011, 2011:138929.

(4) Inoue, Y., Yoshimura, S., Tozuka, Y., Moribe, K., Kumamoto, T., Ishikawa, T., Yamamoto, K., 2007. Application of ascorbic acid 2-glucoside as a solubilizing agent for clarithromycin: solubilization and nanoparticle formation. Int. J. Pharm. **331**, 38–45.

(5) Tanaka, H., Yamamoto, R., 1996. Pharmaceutical studies on ascorbic acid derivatives. Yakugakuzasshi **86**, 376–383.

(6) Moribe, K., Tanaka, E., Maruyama, K., Iwatsuru, M., 1998. Enhanced encapsulation of amphotericin B into liposomes by complex formation with polyethylene glycol derivatives. Pharm. Res. **15**, 1737–1742.

The Natural killer cell activation by Pam2 lipopeptides *in vitro* and *in vivo*

Tsukasa Seya

Department of Microbiology and Immunology, Hokkaido University Graduate School of Medicine, Kita-15, Nishi-7, Kita-ku, Sapporo 060-8638, Japan

ABSTRACT Natural killer (NK) cells play a pivotal role in selective elimination of tumor and virus-infected cells. NK cells are induced by stimulation with Toll-like receptor (TLR) 2 in myeloid dendritic cells (DC), along with activation of the MyD88 signal pathway. Bacterial lipoproteins, including Pam2Cys lipopeptides, act as TLR2 agonists and induce inflammatory cytokines via activation of macrophages (Mf)/dendritic cells (DC). Using synthetic chemical compounds, we identified the essential a.a. for expression of DC TLR2-mediated activation of NK cell. Their lipid moiety as well as peptide sequences appear to be indispensable to the Mf/DC-driven NK activation. This Pam2Cys/TLR2-mediated NK activation was largely abrogated in vivo, since IL-10 and regulatory T cells are induced along with DC maturation. Although NK cell-dependent suppression of tumor is minimal in *in vivo* syngenic tumor-bearing mice, TLR2 has NK-enhancing activity in addition to the MyD88-dependent cytokine production. Bacterial infection may modulate host protective immunity through TLR2 against cancer and other viral infectious diseases.

Introduction

Bacterial infections usually modify the host immune system and generate high potency of suppression against preformed cancer and secondary viral infections. It has been reported that pathogen-derived factors named PAMP alter the host immune system. *Staphylococcus aureus*, a versatile Gram-positive pathogen, is reported to activate NK cells during infection (1). *S. aureus* cell wall components contain innate pattern molecules including lipoproteins, and provoke the activation of host immune cells (2). Mice lacking TLR2 or the adaptor protein MyD88 are highly susceptible to *S. aureus* infection (3). Thus, the response to *S. aureus* cell wall pattern molecules involves TLR2 signaling. Since most myeloid cells including macrophages and dendritic cells express TLR2 on the cell-surface in human and mouse, signaling events of myeloid cells by TLR2 ligands are critical for NK cell activation (4).

The molecular basis by which *S. aureus* activates host immunity has been investigated, and TLR2/MyD88 determines the pathway for activation of macrophages/DC in mice (5). Lipoprotein also activates TLR2 in human cells (6,7). *In vitro* studies in both cases, inflammatory cytokines, IL-1β, IL-6, TNF-α and IL-12p40, and an inhibitory cytokine IL-10 but not type I interferon (IFN), are induced by DC/Mf through TLR2 stimuli (3,8). NK cells are poorly activated in an early phase of TLR2 stimulation or bacterial infection (9). Structural analysis and chemical synthesis of the *S. aureus* functional lipoproteins indicate that diacylated Pam2Cys lipopeptides are recognized by the complex of TLR2 and TLR6 on DC (7,8), and thus participate in DC-mediated NK activation *in vitro*. Some Pam2Cys lipopeptides with particular a.a. following the Cys, however, fail to induce NK activation as well as leading to induction of cytokines (4). Hence, TLR2 stimulation by Pam2Cys lipoprotein can signal the driv-

ing NK activation in Mf/DC and cytokine release only when the receptors recognize the distinct thirdly structural motifs.

Here, we review the structural-functional relationship of Pam2Cys lipopeptides with reference to the *in vivo* results of gene-disrupted mice (3,8). TLR2, in concert with TLR6, is involved in their recognition of bacterial lipoproteins (7,8) and engaged in IL-10 and Treg induction (10). The essential a.a. identified in the peptides for NK cell activation are also discussed.

Methods

Chemical compounds

The synthesized Pam2Cys compounds are listed in Table 1. The synthesis of lipopeptides was achieved with a combination of solution- and solid-phase methods (Fig. 1). Briefly, for the preparation of the Pam2Cys backbone, the protected cysteine (Fmoc-Cys-OtBu) and the iodide (3-iodopropane-1,2-diol) were coupled under basic condition by using Cs_2CO_3 to give Fmoc-Cys(2,3-dihydroxypropyl)-OtBu, and the subsequent acylation and cleavage of the tBu group gave Fmoc-Pam2Cys-OH (11). The peptide component, which included 16 different peptide sequences from 14 lipoproteins of *S. aureus* NCTC8325, was prepared by using solid-phase synthesis on Wang resin in a similar fashion to Jung's lipopeptide synthesis. Fmoc-Pam2Cys-OH (11,12) was then introduced to the N terminus of the peptides linked to the resin (Fig. 1). Subsequent cleavage of the Fmoc group, detachment from the resin, and deprotection of all protecting groups gave the lipopeptides Pam2Cys1–16, and also Pam2CSK4. Pam2CSK, Pam2CSK2 and other mutation-induced lipopeptides were synthesized in Biologica Co. Ltd. Commercial and our synthetic Pam2CSK4 are listed in Table 1.

Preparation of immune cells

Mouse bone marrow-derived DC (BMDC) were prepared as described previously (13). Spleen NK cells were positively isolated from spleens with DX5 Micro Beads (Miltenyi Biotech) (14). In experiments requiring high purity NK cells, Thy1.2 beads were

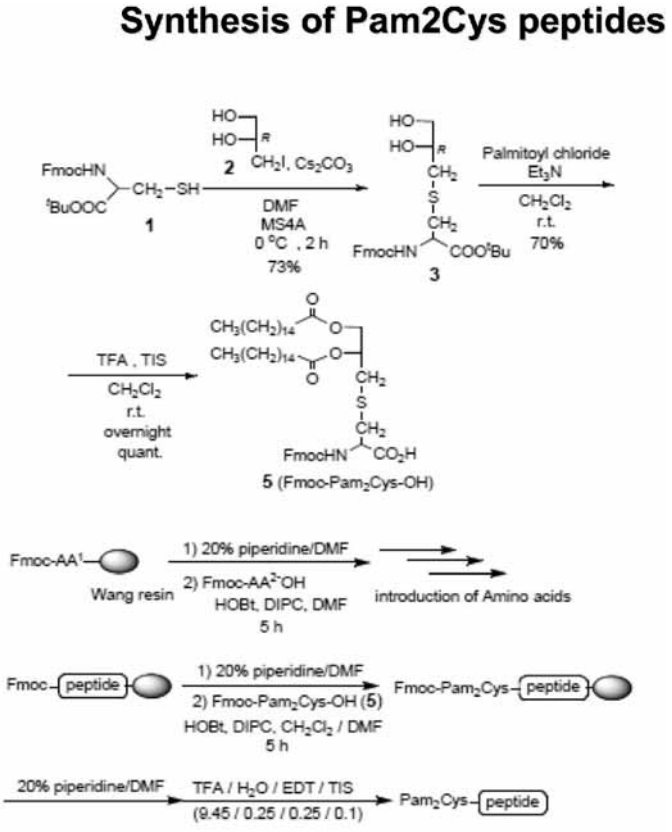

Scheme 1. Chemical synthesis of lipopeptides LPSA-01~LPSA14-2 and Pam_2CSK_4.

Fig. 1. Structural illustration of chemical compounds of lipopeptides.
Chemical synthesis of lipopeptides and Pam_2CSK_4 were performed as dscribed previously (see the text).

additionally used for negative selection according to the Miltenyi's protocol. The purity of NK cells ($DX5^+$ cells) was routinely about 70%. NKT cells might be an only trace constitution of our preparation. $DX5^+$ NK cells were used within 24 h.

The degrees of CD86 upregulation were examined with the these lipopeptides, and similar DC maturation was evaluated by flow cytometry. Although the levels of CD86 were increased in response to Pam2 peptides (100 nM), no significant difference was observed among the Pam2 peptides tested. At the dose of Pam2 where cytokine induction sufficiently occurs, CD86 expression inadequately takes place in BMDC, as reported previously (4).

Table 1. Pam2 lipopeptides used for this study

No.	Lipid	Amino acid sequence	TNF-α*
Pam2Cys1	Pam2	CANTRHSESDK	++
Pam2Cys2	Pam2	CGTGGKQSSDK	++
Pam2Cys3	Pam2	CGNGNKSGSDD	++
Pam2Cys4	Pam2	CSNIEIFNAKG	+/-
Pam2Cys5	Pam2	CTTDKKEIKAY	+++
Pam2Cys6	Pam2	CSFGGNHKLSS	++
Pam2Cys7	Pam2	CGSQNLAPLEE	+++
Pam2Cys8	Pam2	CGQDSDQQKDG	+++
Pam2Cys9	Pam2	CGNDDGKDKDG	+++
Pam2Cys10	Pam2	CGNNSSKDKEA	+++
Pam2Cys11	Pam2	CSLPGLGSKST	+++
Pam2Cys12	Pam2	CSTSEVIGEKI	++
Pam2Cys13	Pam2	CPFNCVGCYNK	+/-
Pam2Cys14	Pam2	CGSQNLAPLEEK	+/-
Pam2Cys15	Pam2	CLILIIASETL	+/-
Pam2Cys16	Pam2	CLILIIASETLFSFSHLTDVK	+/-
Pam2Cys17	Pam2	CSK	n.d.
Pam2Cys18	Pam2	CSKK	n.d.
Pam2Cys19	Pam2	CSKKKK	++

* 100 pg/ml of Pam2 peptides were used for stimulation of PBMC. TNF-alevels: +/ -; < 200, ++; 2,000-4,000, +++; 4,000-7,000 pg/ml. n.d., not dete rmined.

Table 2. Properties of synthetic Pam2 peptides

	Pam 1	2	3	4	5	6	7	8	9
CD80 maturation	△	△	○	○	○	○	○	○	○
CD86 maturation	○	△	△	△	△	○	○	○	○
IL-12p40 ELISA	++	++	++	+++	++	+++	++	++	++
IL-6 ELISA	++	++	++	+++	++	+++	++	++	++
DC-NK IFN-g ELISA	+	+	++	+	+	+	+	+	++
DC-CTL 3H									
TLR2-NF-kB	21	22	25	18	25	8.5	22	23	26
NK(IFN) TLR2-dep	○	×	○	○	×	○	○	×	×
	10	11	12	13	14	15	16	17	LPS
CD80 maturation	○	○	○	△	○	○	○	○	○
CD86 maturation	○	○	○	×	○	○	○	○	○
IL-12p40 ELISA	++	++	++	+	++	++	+	++	25000
IL-6 ELISA	++	++	++	+	++	++	+	++	22000
DC-NK IFN-g ELISA	+	+	+++	–	+	+ –	–	+++	+++
DC-CTL 3H									
TLR2-NF-kB	22	18	1.6	1.6	23	3.6	2.5	20	PGN: 16
NK(IFN) TLR2-dep	△	△	×	—	×	○	—	△	

IL-12p40 ELISA	+:4000～5000 pg/ml ++:9000～13000 pg/ml +++:18000～19000 pg/ml
IL-6 ELISA	+:1000～3000 pg/ml ++:4000～6000 pg/ml +++:8000～8500 pg/ml
DC-NK IFN-g ELISA	–:0～50 pg/ml +:200～400 pg/ml ++:400～500 pg/ml +++:600～700 pg/ml

Cytokines

IL-6 and IL-12p40 levels were determined by ELISA with the supernatant of the media where BMDC and each of the lipopeptides were co-cultured for 24 hrs. These cytokines were detected with high levels in the wells with Pam2Cys12, Pam2CSK4, MALP-2s and MALP-2f but not in Pam2CSK (Table 1, Table 2). These lipopeptides neither induced the mRNA of type I interferon (IFN), IL-15 and I-18 (data not shown) nor produced less than the detection limit (< 5 pg/ml) of IL-12p70 protein.

IL-6 and IL-12p40 levels were determined by ELISA using the supernatant of the media from bone marrow-derived DC (BMDC) culture with the lipopeptides for 24 h. The cytokines were detected at high levels in the cultures with lipopeptides, with the exception of Pam2Cys17, Pam2Cys13, and Pam2Cys16 (Table 2). The cytokine contents of wells with BMDCs stimulated with Pam2Cys13 and Pam2Cys16 were as low as the control Pam2Cys17.

In vitro NK cell activation

Previous reports suggested that TLR2 agonists can induce NK activation (15,16). To investigate whether the *S. aureus* lipoproteins had NK cell-activating activity, we added the Pam2Cys peptides at 100 nM to BMDC/NK cultures as described previously (4). Three markers for NK activation (17) were assessed: IFN-γ production, up-regulation of NK surface markers, and target B16D8 cell cytotoxicity by NK cells. IFN-γ was generated in the supernatants (sup) in response to the lipopeptides (Fig. 2A). Most of the lipopeptides induced DC-derived NK cell activation in a TLR2/MyD88-dependent manner judged by IFN-γ (Fig. 2A-C). However, Pam2Cys13, Pam2Cys15, and Pam2Cys16 showed significantly low potential for IFN-γ induction as comparable to Pam2Cys17 (Fig. 2A). Cytotoxic activity was evaluated using B16D8 cells as a target (13). Again, Pam2Cys13, 15 and 16 did not induce effective killing (Fig. 2D). The other *S. aureus* lipopeptides Pam2Cys12 and 19 had sufficient killing activity: two simultaneously generated examples are shown in Figure 2D.

The NK cell activation markers CD25 and CD69 were analyzed by flow cytometry after co-culturing NK cells with BMDC and Pam2Cys stimulants (Fig. 2E). Up-regulation of surface CD25 and CD69 was observed in NK cells incubated with BMDC and Pam2Cys18 or 19, while the levels of their up-regulation by Pam2Cys13, 15 or 16 were near those of the negative control Pam2Cys17, for stimulating NK cells co-cultured with BMDC. In contrast, no increase was observed for CD56, NKp46 and DNAM-1 (data not shown).

In vivo NK cell-mediated tumor regression

Mice were s.c. injected with 2-3x10^5 B16D8 on the back. B16D8 melanoma is NK sensitive B16 melanoma line, which we have previously established (18). The tumor growth was monitored twice a week. Sometimes mice were pre-treated wit 500 μg of anti-CD25mAb 3 days before tumor challenge. Ten nmol of Pam2 lipopeptides or control saline was s.c into footpad or i.p. twice a week. The both route of injection gave similar results.

Results

Participation of TLR2/MyD88 in Pam2Cys-mediated BMDC and NK activation

Activated NK cells are a major source of IFN-γ, which causes a variety of responses in the immune system. To examine whether direct stimulation of NK cells with Pam2Cys18 or Pam2Cys19 induced minimal secretion of IFN-γ, we measured the frequency of IFN-γ-secreting NK cells, at 24 h after incubation. By intracellular staining, IFN-γ-secreting NK cells were increased after direct Pam2Cys18 or 19 stimulation (data not shown). As shown in Figs. 2A-C, TLR2 ligands except Pam2Cys12, 18 and 19 barely increased the levels of IFN-γ of NK cells by co-culture with Pam2Cys-stimulated TLR2-/- or MyD88-/- BMDC. On the other hand, NK cells induce moderate levels of IFN-γ in response to BMDC stimulated with Pam2Cys12, 18 or 19 (open bars in Fig. 2A), although no

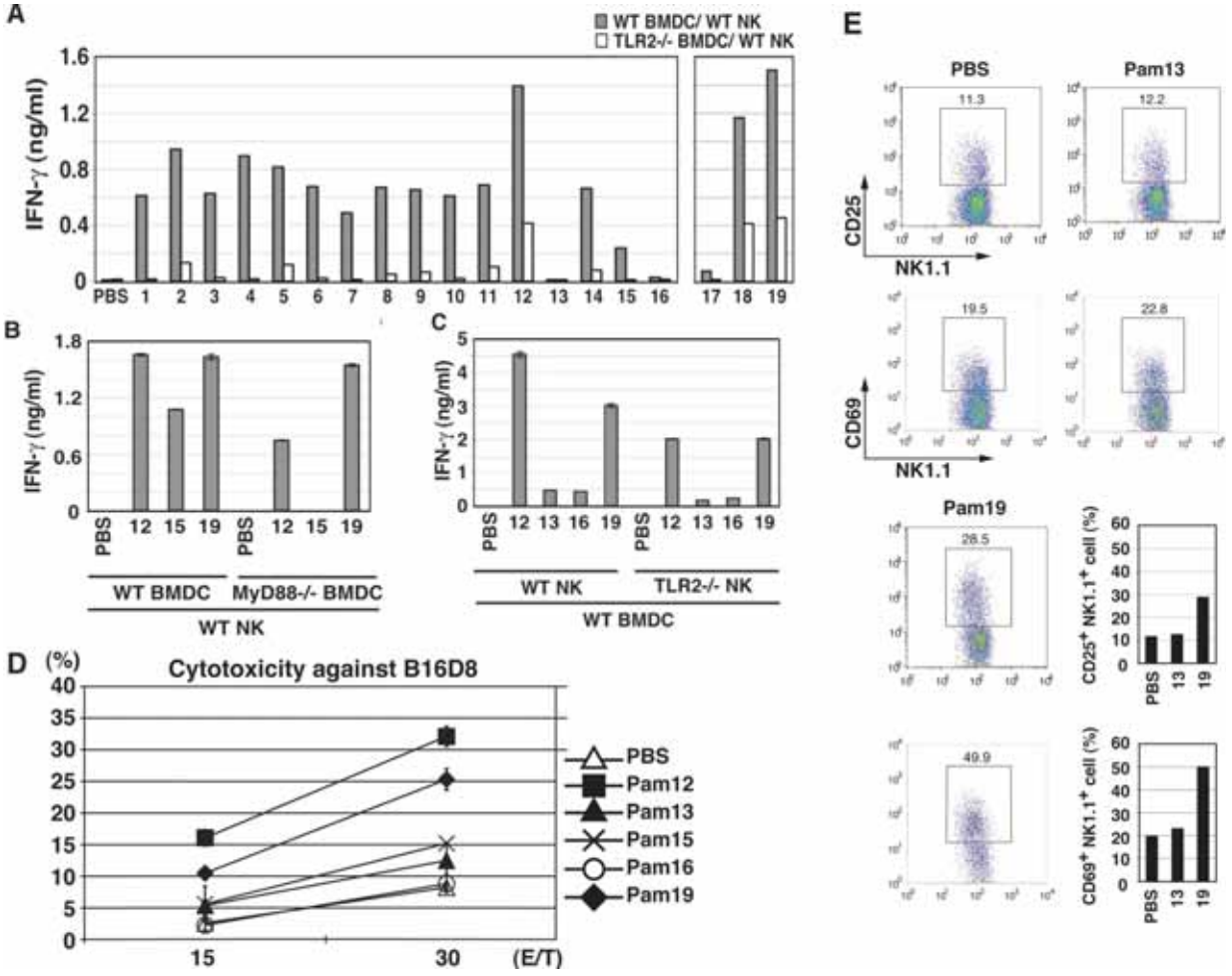

Fig. 2. TLR2 on BMDC mainly participate in Pam2Cys-mediated NK activation. (A) BMDC TLR2-independent NK activation by Pam2Cys12, 18 and 19. BMDC from wild-type (closed bars) or TLR2-/- (open bars) mice were stimulated with control PBS or 100 nM of indicated Pam2Cys peptides for 4 h. Cells were then co-cultured with wild-type NK cells at 1:2 ratio for 24 h. Then, the supernatants were collected and IFN-γ was measured by ELISA. (B) Pam2Cys12 and 19 induce NK activation in culture with MyD88-/- BMDC. NK cells were co-cultured with wild-type or MyD88-/- BMDC in the presence of the indicated Pam2Cys peptides (represented by the numbers) as in Panel A. 24 h after incubation, culture media were collected to determine cytokines by ELISA. (C) Pam2Cys12 and 19 induce TLR2-/- NK activation in culture with wild-type BMDC. Wild-type BMDC and NK cells with either wild-type or TLR2-/- phenotype were incubated at 1:2 ratio with the indicated Pam2Cys peptides (represented by the numbers) as in Fig. 2. 24 h after incubation, culture media were collected to determine cytokines by ELISA. One representative of the three similar experiments is shown. (D) NK cell cytotoxicity against B16D8 cells was measured by ^{51}Cr release assay at indicated E:T ratios as described in the Methods section. (C) Populations of CD25$^+$ and CD69$^+$ NK cells were measured by flow cytometry after stimulation of NK cells with BMDC treated with indicated Pam2Cys peptides. BMDC were stimulated with control PBS, 100 nM of Pam2Cys13 or Pam2Cys19 for 4 h. Then, BMDC were incubated with NK cells. After 24 h, cells were analyzed by flow cytometer using the markers for separation. %Positive cells are shown to the right. The data shown are representative of at least three independent experiments.

structural similarity was detected between Pam2Cys12 and Pam2Cys18 or 19.

We next examined whether lipopeptide-mediated cytokine secretion and NK activation were dependent on BMDC TLR2 and MyD88. IL-6 and IL-12p40 secretion were completely abrogated in TLR2-/- BMDC (data not shown). However, low amounts of IFN-γ were detected in co-cultures of TLR2-/- or MyD88-/- BMDC and wild-type (WT) NK cells in the presence of Pam2Cys12, 18, or 19 (Fig. 2B,C), and lesser extent of IFN-γ was still detected in co-cultures of WT BMDC and TLR2-/- NK cells in the presence of Pam2Cys12 or Pam2Cys19 (Fig. 2C). These results were reproduced with MyD88-/- BMDC (not shown).

In addition, there would be a direct NK cell activation pathway by Pam2Cys lipopeptides. Moderate IFN-γ was detected in the media containing TLR2-/- BMDC, WT NK and Pam2Cys12 or 19 (Fig. 2A), the IFN-γ levels being comparable to those of WT NK cells alone stimulated with Pam2Cys12 or 19. TLR2-/- NK cells still produced very low levels of IFN-γ when the TLR2-/- NK cells were co-cultured with WT BMDC (data not shown). However, No IFN-γ was detected in the media containing TLR2-/- NK and Pam2Cys12 or 19. Thus, all Pam2Cys peptides including Pam2Cys12, 18 and 19 act on BMDC to drive NK activation. Notably, WT NK cells alone produce minute IFN-γ in response to Pam2Cys12 or 19, which means that Pam2Cys12 and Pam2Cys19 additionally induce direct NK activation. The Pam2Cys receptors for this NK activation is through the NK cell TLR2 followed by the MyD88 pathway. However, minute activation by Pam2Cys12 or 18/19 appears to be left in TLR2-/- NK cells stimulated with Pam2Cys12/19-treated BMDC, which should be attributed not to TLR2 but to other unknown mechanisms.

Combinatorial recognition of Pam2Cys lipopeptide by TLR2 and TLR6

TLR2 recognizes diacyl lipopeptides in combination with TLR6 (8,19) while TLR2 recognizes triacyl lipopeptide with TLR1 (20). We found TLR2/6 cooperation in the recognition of *S. aureus* lipopeptides using HEK293 cells that express TLR2/6. Data on the use

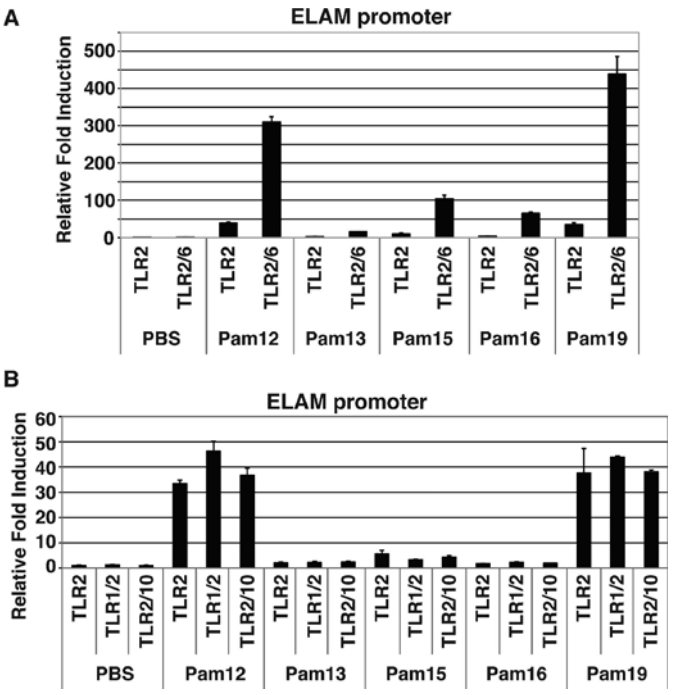

Fig. 3. TLR6 promotes TLR2 signaling in Pam2Cys peptides recognition. (A, B) HEK293 cells were transfected with plasmids encoding TLR2, TLR6, TLR1 or TLR10 and the ELAM-luciferase reporter. After 24 h, the cells were treated with indicated Pam2Cys peptides (100 nM) for 6 h and then luciferase activities were measured. The data shown are representative of at least three independent experiments.

of TLR2/6 by Pam2Cys12, Pam2Cys13, Pam2Cys15, Pam2Cys16, and Pam2Cys19 are shown in Figure 3. Single receptors of TLR1, TLR6, and TLR10 showed little activation of NF-κB by reporter assay, and only TLR2 exhibited $<$ 60-fold ELAM promoter activation (data not shown). Pam2Cys12 and Pam2Cys17 more efficiently activated the ELAM promoter ($>$ 300 fold over the control) with TLR2 and 6, than with TLR2 alone (Fig. 3A). TLR1 or TLR10 in combination with TLR2 did not amplify the signal (Fig. 3B). Pam2Cys13 only weakly enhanced the TLR2 potential with additional TLR6 expression in HEK cells (Fig. 3A), and only a slight increase was observed with Pam2Cys15 and Pam2Cys16 with simultaneous expression of TLR2 and TLR6 (Fig. 3A). Hence, TLR6 helped TLR2 to amplify the TLR2 signal from most Pam2Cys lipopeptides, but not with Pam2Cys13 or Pam2Cys15/16.

Critical a.a. in Pam2Cys lipopeptides for BMDC-mediated NK activation

Recent studies revealed an extensive cross-talk between NK cells and mDCs (21,22). We analyzed the structural background that supports NK activation using our synthetic diacyl lipopeptides. All NK-activating lipopeptides tested had Cys-Ser/Thr or Cys-Gly/Ala in their N-terminus (Table 1). However, the two lipopeptides with the lowest ability to activate NK cells had differences, with Cys-Pro in the N-terminus of Pam2Cys13, and Cys-Leu-Ile in Pam2Cys15/16. When the second Pro in Pam2Cys13 was replaced with Ser, and the Leu-Ile sequence of Pam2Cys16 was replaced with Ser-Asn, the newly synthesized peptides, Pam2Cys13(P-S) and Pam2Cys16(LI-SN), recovered their ELAM reporter activity (Fig. 4A).

We next tested whether BMDC mature to activate NK cells through BMDC's TLR2 activation by these modified Pam2Cys. Pam2Cys13(P-S) and Pam2Cys15(LI-SN) recovered NK-activating properties by the amino acid conversions judged by IFN-γ production (Fig. 4B) and cytotoxicity against B16D8 cells (Fig. 4C). Since Pam2Cys13(P-S) acts only on BMDC (not shown), this Pam2Cys activity is attributable to recovered BMDC maturation. Hence, Pam2Cys13(P-S) and Pam2Cys16(LI-SN) are NK activators via mDC TLR2. Hence, we conclude that the peptide sequence near the N-terminus is important for NK activation by diacyl lipopeptide.

Production of both IL-6 and IL-12p40 was dependent on BMDC TLR2 (Fig. 5A). Pam2Cys13 and Pam2Cys16 induced these cytokines at very low levels. When Pam2Cys13(P-S) or Pam2Cys16(LI-SN) replaced Pam2Cys13 or Pam2Cys16 in the same assay system, the cytokine levels recovered to levels similar to those of the other lipopeptides (Fig. 5B). These activities were almost completely abrogated in TLR2-/- BMDCs. Thus, the a.a. replacements allows BMDC to generate the TLR2 signal, irrespective of their artificial modifications.

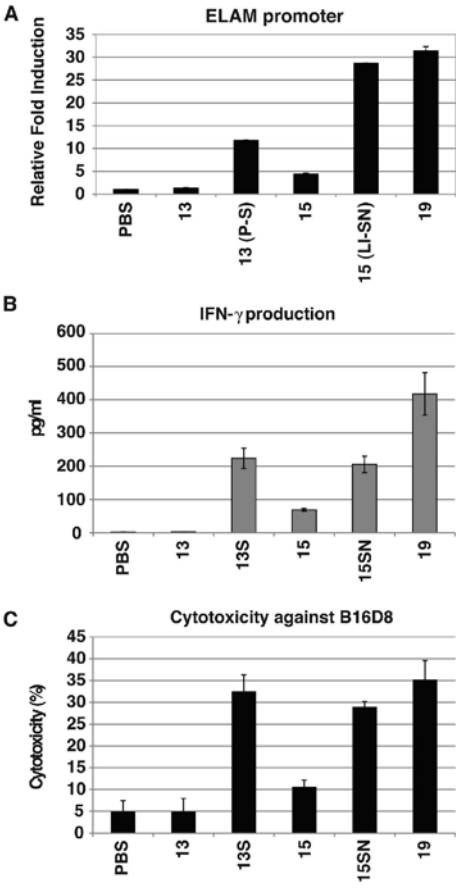

Fig. 4. Amino acids near the Pam2 lipid are critical for TLR2 recognition. (A) HEK293 cells were transfected with plasmids encoding TLR2 and the ELAM-luciferase reporter. After 24 h, the cells were treated with indicated Pam2Cys peptides (100 nM) for 8 h and then luciferase activities were measured. The numbers represent the Pam2Cys's numbers. 13(P-S), Pam2Cys13 with second Proline replaced with Serine; 15(LI-SN), Pam2Cys15 with second Leucine and third Isoleucine replaced with Serine and Asparagine. (B,C) BMDC-mediated NK cell activation occurs by stimulation with Pam2Cys13 (P-S) and Pam2Cys15 (LI-SN). BMDC and NK cells were prepared from wild-type mice. BMDC were stimulated with PBS or indicated Pam2Cys peptides for 4 h. Then, BMDC were incubated with wild-type NK cells for 24 h. IFN-γ production (A) and B16D8 cytotoxicity (E:T ratio=50:1) (B) were measured as in Figure 2. 13S and 15SN represent Pam2Cys13(P-S) and Pam2Cys15(LI-SN), respectively.

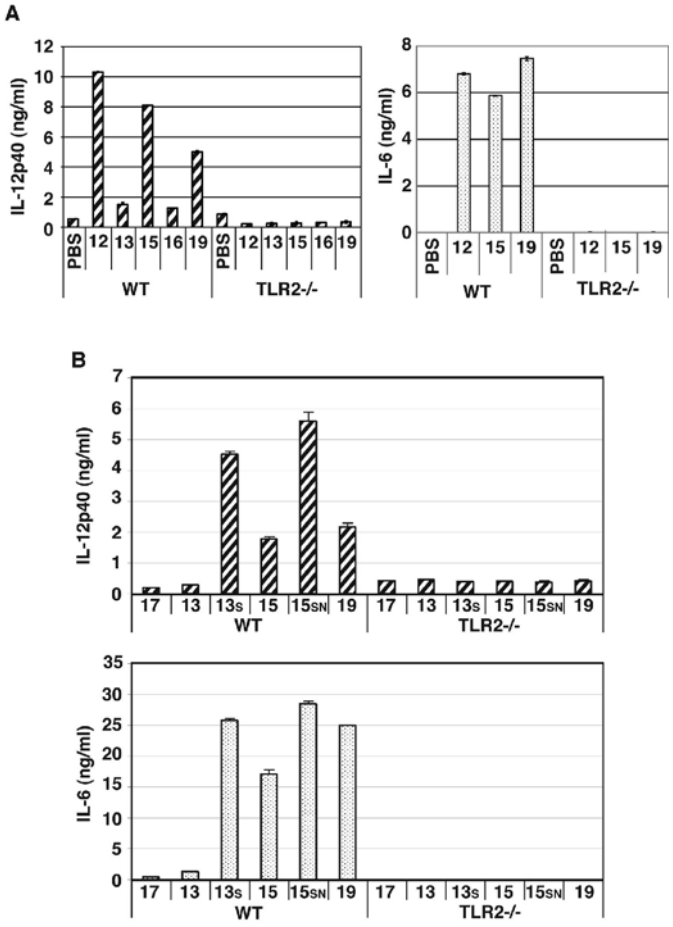

Fig. 5. TLR2 agonists in BMDC is crucial for IL-6 and IL-12 production. (A) IL-6 and IL-12p40 production by wild-type but not TLR2-/- BMDC by Pam2Cys stimulation. BMDC prepared from wild-type or TLR2-/- mice were treated with indicated Pam2Cys peptides (100 nM) for 24 h. IL-12p40 and IL-6 concentrations in the supernatants were determined by ELISA. (B) Pam2Cys13(P-S) but not Pam2Cys13 induces IL-6 and IL-12 from BMDC. BMDC prepared from wild-type mice were treated with indicated Pam2Cys peptides (100 nM) for 24 h as in panel A. Cytokines in the supernatants were determined by ELISA. 13S, Pam2Cys13(P-S); 15SN, Pam2Cys15(LI-SN).

BMDC-NK contact is indispensable for BMDC TLR2-mediated NK activation

Pam2Cys13(P-S) matured BMDC to activate NK cells without direct action on NK cells (Fig. 6A). First, we collected the sup of BMDC stimulated with Pam2Cys13 or Pam2Cys13(P-S). Surprisingly, Both of the sup failed to confer NK activating function on the mixture of naïve BMDC and NK cells (data not shown). The capacity of BMDC sup to induce IFN-γ-secretion by NK cells was further evaluated using a transwell system (Fig. 6A,B). No significant increase in IFN-γ-secreting NK cells was observed when lipopeptide-activated BMDCs and NK cells were separated by transwell (Fig. 6A,B). Frequency of IFN-γ-producing NK cells was high in co-culture with Pam2Cys13(P-S)-stimulated BMDC and NK cells (Fig. 6B upper panel) while the IFN-γ-producing NK cells were diminished in the transwell (Fig. 6B lower panel). In either case, IL-15 and IFN-α/β were barely increased in Pam2Cys-stimulated BMDCs by RT-PCR (data not shown). Thus, soluble factors barely participate in BMDC-mediated NK activation. BMDC-NK contact is essential for TLR2-mediated NK activation.

Pam2Cys-mediated tumor regression in vivo

Recent studies revealed that intratumoral or i.p. injection of the lipopeptide, MALP-2 (Pam2CGNNDESNISFKEK), supresses pancreatic carcinoma in a mouse model (23). Tumor suppression is also observed with Pam2Cys type lipopeptides in B16D8 (NK-sensitive) implant mice (24). The antitumor function by MALP-2 and MALP-2s (Pam2CGNNDE) are abrogated in MyD88-/- mice, suggesting that TLR2/MyD88 and following cell-mediated immunity play a major part of tumor suppression (24). We tested whether Pam2Cys lipopeptides injected s.c. induce growth retardation of the tumor (NK-target B16D8 cells) via NK activation using tumor-implanted mice (Fig. 7). Pam2CSK4 (i.e. Pam2Cys18) s.c. injected around tumor exhibited slight growth retardation of tumor (Fig. 7 right lower panel). This Pam2CSK4 activity was abrogated by injection of asialoGM-1 Ab (data not shown). In contrast, no tumor growth retardation was observed in this NK-sensitive tumor by s.c. injected MALP-2 or other lipopeptides, Pam2Cys13 and 15 (Fig. 7). Furthermore, only marginal tumor suppessing capacities were observed

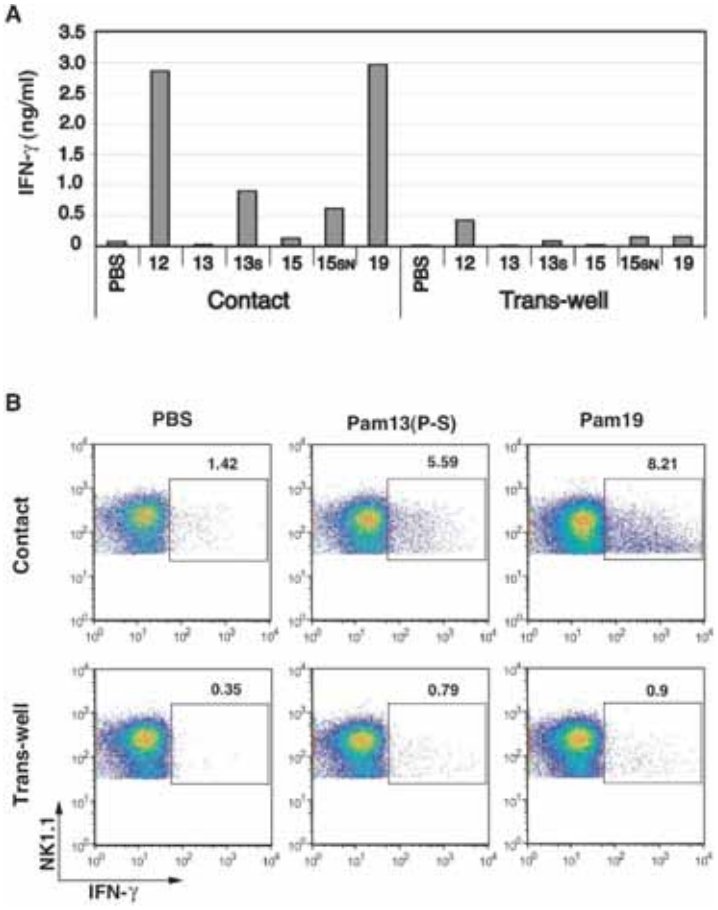

Fig. 6. BMDC-NK cell contact induces NK activation. (A) IFN-γ induction by NK cells requires BMDC-NK contact. BMDC prepared from wild-type mice were treated with indicated Pam2Cys peptides (100 nM) for 4 h. Then, BMDC were incubated with naïve NK cells for 24 h at the ratio of 1:2 (left hand bars in Contact). The level of IFN-γ was measured by ELISA. Of note, the sup of the stimulated BMDC was collected and added to cultures of unstimulated BMDC and naïve NK cells, but only a minute level of IFN-γ was detected in the sup (data not shown). The levels of IFN-γ in the same combinations are shown (right hand bars in Trans-well) when stimulated BMDC and NK cells were separated by trans-well. 13S, Pam2Cys13(P-S); 15SN, Pam2Cys15(LI-SN). (B) %IFN-γ-positive NK cells were determined by intracellular staining. Wild-type BMDC prepared from C57BL/6 mice were treated with Pam2Cys13(P-S) peptides (100 nM) for 4 h as in panel A. Then, wild-type NK cells were added to the wells. 20 h after co-culture, breferdin was added to the wells and incubation was continued further for 4 h. NK cell activation was determined by IFN-γ produced in NK cells. %IFN-γ-positive NK cells was determined by FACS.

in a similar system with Pam2Cys6 and Pam2Cys12. These results infer that most Pam2Cys lipopeptides exert only minimal potential if any, to activate NK cells through BMDC *in vivo*. Unlike BCG-CWS (25) or polyI:C (13,26), MALP-2 barely suppresses tumor growth in this mouse system.

Pam2 lipopeptides induce IL-10 in vitro and in vivo in a TLR2-dependent manner

To investigate why Pam2Cys lipopeptides could not induce effective anti-tumor responses against NK-sensitive tumors *in vivo*, we investigated whether Pam2Cys lipopeptides could activate suppressive factors, such as IL-10 and regulatory T cell (Treg)-

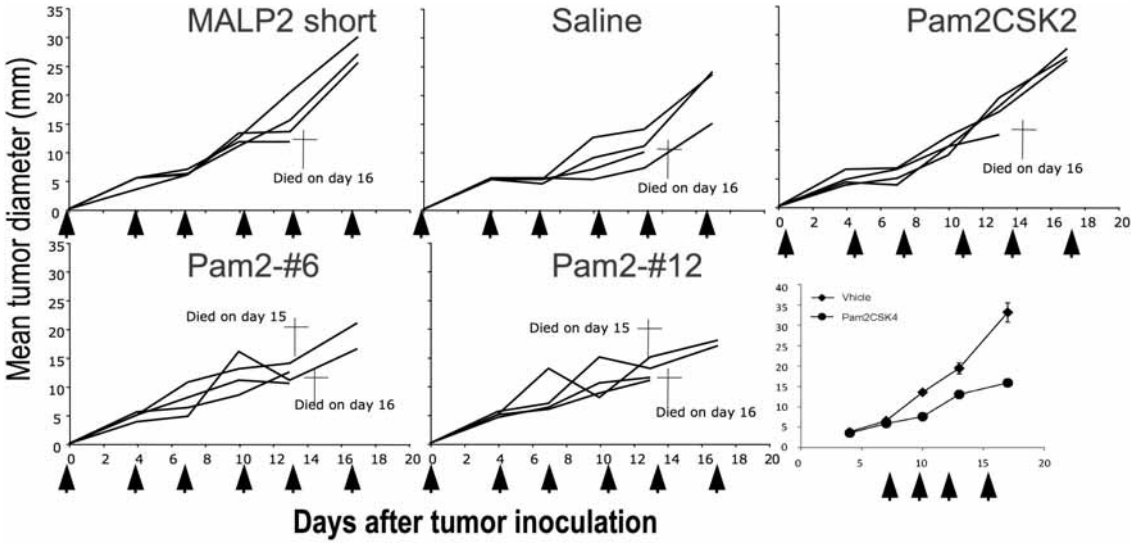

Fig. 7. Pam2Cys lipopeptides poorly induce antitumor NK activation *in vivo*.
Panel A: MALP-2 fails to inhibit tumor growth *in vivo*. B16D8 cells were transplanted subcutaneously into mice at day 0. Mice (16 week-old, female) were treated with Pam2CSK4 (upper panel) or MALP-2s (lower panel) at day 0, 3, 7, 9, 13, 17 as described in *Materials and Methods*. Each group consists of n=4. Surface diameters of the implanted tumors were measured. Mean $\pm$ SD are shown. Panel B: Pam2Cys lipopeptides do not induce effective anti-tumor immunity *in vivo*. Mice were injected with B16D8 melanoma cells ($2x10^5$) on back. The mice were injected s.c. into footpad with the indicated Pam2 lipopeptides (10 nmol) or saline twice a week as arrows started on day 0. Tumor growth was monitored in a blind manner. A cross indicates that one mouse is dead. One of 2 experiments is shown.

related molecules. For this experiment, we mainly used a representative Pam2 lipopeptide, Pam2CSK4, since Pam2CSK4 could activate DCs as well as other tested Pam2Cys lipopeptides *in vitro* (4).

When the mRNA levels from DCs stimulated with or without Pam2Cys lipopeptides were analyzed, they up-regulated retinoic acid dehydrogenase 2 (RALDH2) and IL-10. RALDH2 in DCs activates retinoic acid, which is an important cofactor for TGF-β1 to induce Foxp3 (27,28). However, Pam2 lipopeptides did not up-regulate the mRNA of TGF-β1 (Fig. 8A).

To confirm whether IL-10 protein is produced from DCs, we stimulated DCs with Pam2 lipopeptides *in vitro* for 24 hours and the concentration of IL-10 in the supernatants was measured by the ELISA. Bone-marrow derived DCs (BM-DCs) stimulated by Pam2 lipopeptides produced IL-10 (Fig. 8B). IL-10 was also produced by Pam2 lipopeptide-stimulated DCs from the spleen (data not shown). When DCs from TLR2- knockout (TLR2KO) mice were cultured with Pam2 lipopeptides, the production of IL-10 was not detected (Fig. 8B). Hence, IL-10 production was TLR2 dependent. Interestingly, we also found that Pam2 lipopeptides induced IL-10 production from NK cells (Fig. 8C).

To see if $CD4^+$ T cells produced IL-10 with Pam2 lipopeptides, OT II ovalbumin (OVA) transgenic $CD4^+$ T cells were cultured with DCs along with various doses of OVA peptide, with or without Pam2 lipopeptides (Fig. 8D). In the presence of Pam2 lipopeptides, more IL-10 was produced in the culture supernatants when OT II $CD4^+$ T cells were cultured with DCs and antigen (Fig. 8D). Importantly, the IL-10 production was increased in an antigen-dose dependent manner (Fig. 8D).

Next, we analyzed the concentration of IL-10 in the serum of Pam2 lipopeptide-treated mice (Fig.8E). When serum was taken at one day after Pam2CSK4 injection, significant amounts of IL-10 was detected (Fig. 8E), however, Th1, Th2 and Th17 cytokines were not detected (Fig. 8E). IL-10 production in serum was confirmed to be TLR2 dependent because we could

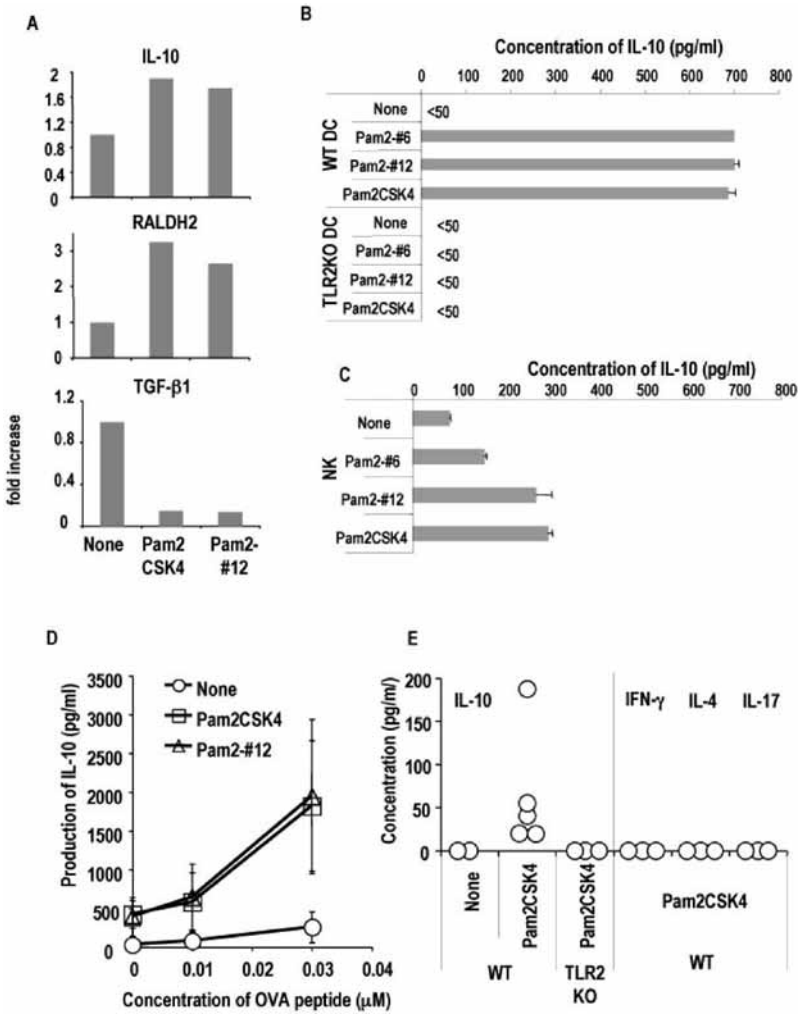

Fig. 8. Pam2 lipopeptides induce IL-10 and retinoic acid dehydrogenaze. (A) Spleen DCs from B6 mice were cultured with or without 100nM of Pam2CSK4 or Pam2Cys12. After 4 hours, total RNA was prepared and real-time PCR was performed. Expression of each sample was normalized to GAPDH mRNA expression and fold increase of each sample was calculated to the expression at 0 hours. One of 2 experiments is shown. (B) BM-DCs ($1x10^5$) from wild type (WT) or TLR2KO mice were cultured with or without 100 nM of Pam2Cys6, Pam2Cys12 and Pam2CSK4 for 24 hours. The culture supernatants were measured for IL-10. One of 2 experiments is shown. (C) NKs ($2x10^5$) from spleen were cultured with 100nM of Pam2Cys6, Pam2Cys12 and Pam2CSK4 for 24 hours. The culture supernatants were measured for IL-10. One of 2 experiments is shown. (D) OT II $CD4^+$T cells ($5x10^4$) were cultured with spleen DCs ($5x10^4$) with or without 100nM of Pam2CSK4 or Pam2Cys12 at the various dose of OVA peptide. After 5 days, supernatants measured for IL-10. Mean +/-SD from 2 separate experiments is shown. (E) WT or TLR2KO mice were i.p. injected with 10 nmol Pam2CSK4 and next day serum was measured for the indicated cytokine concentration.

not detect IL-10 in Pam2CSK4-treated TLR2KO mice (Fig.8E). Taken together, these results indicated that Pam2 lipopeptides induce IL-10 both *in vitro* and *in vivo* in a TLR2-dependent manner, which might play a role in suppressing tumor immunity induced by Pam2Cys lipopeptides.

Systemic injection of Pam2Cys lipopeptides expands Treg cells through the TLR2 dependent production of IL-10

Since Pam2Cys lipopeptides induce IL-10, we

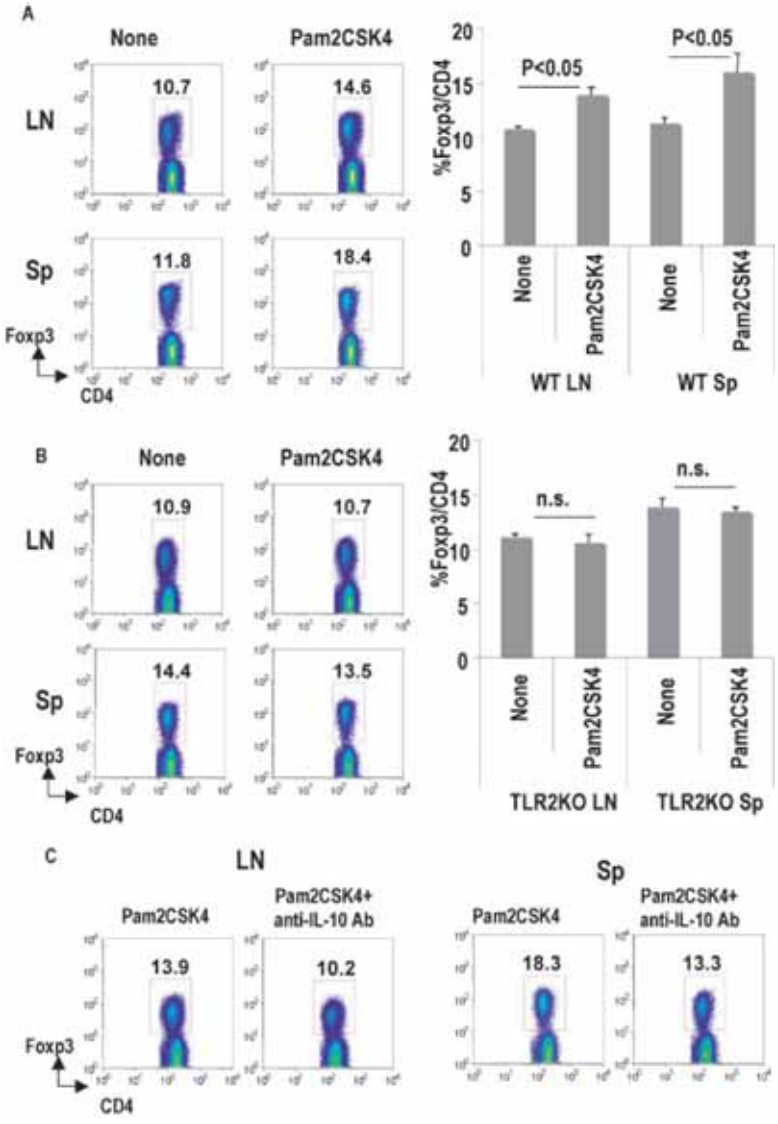

Fig. 9. Systemic injection of Pam2CSK4 expands Foxp3$^+$ T reg in a TLR2- and IL-10- dependent manner. (A) WT mice were i.p. injected with Pam2CSK4 (10 nmol) . After 3 days, spleen (Sp) and lymph node (LN) cells were analyzed for the expression of Foxp3. The plots were gated on CD4$^+$ T cells. One of 4 experiments is shown for the FACS plots. The graphic shows a summary from 4 separate experiments. P value is provided by student-t test. (B) As in (A), but TLR2KO mice were injected with Pam2CSK4. One of 2 experiments is shown for the FACS plots. The graphic shows a summary from 2 separate experiments. N.s. stands for not significant by student-t test. (C) As in (A), but mice were i.p. injected with Pam2CSK4 with or without 200 mg of anti-IL-10 mAb. One of 2 experiments is shown.

investigated whether systemic injection of Pam2Cys lipopeptides could affect Treg cell frequency. IL-10 produced by zymosan plays a role in inducing Treg cells (29). We found that the frequency of Foxp3$^+$ Treg was increased in the spleen and lymph nodes at day 3 after systemic injection of Pam2CSK4 (Fig. 9A). The frequency of T reg cells had returned to normal by day 7 after Pam2CSK4 injection (data not shown). The increase of T reg cells was dependent on TLR2 because Treg cells were not increased in TLR2KO mice injected with Pam2CSK4 (Fig. 9B).

To investigate whether the increase of Foxp3$^+$ Treg is dependent on the IL-10 produced by Pam2CSK4, mice were injected with neutralizing anti-

IL-10 mAb (JES5-2A5) and Pam2CSK4 (Fig. 9C). Control mice injected with anti-IL-10 mAb alone or untreated mice were not included in this experiment, however, the frequency of Foxp3$^+$ T reg cells in the mice injected with anti-IL-10 Ab alone would be similar to that of naïve mice since it is reported that the frequency of Foxp3$^+$ Treg cells is not affected in the spleen of IL-10 (30) or IL-10 receptor β knockout mice (31). After three days, co-administration of anti-IL-10 mAb blocked the increase of Treg cells after Pam2CSK4 injection (Fig. 9C).

Therefore, Pam2 lipopeptides expand Foxp3$^+$ Treg cells at day 3 after systemic injection in a TLR2- and IL-10 dependent manner (10).

Discussion

Here, we demonstrated that the a. a. sequence of *S. aureus* Pam2Cys peptides critically affects the agonistic function for TLR2 and the mode of NK activation. This NK activation is largely dependent on TLR2/MyD88 in BMDC in the mouse system. In addition, Pam2Cys12 and Pam2Cys18/19 have a weak ability to directly activate NK cells without participation of BMDC. In contrast, we determined Pam2Cys13, Pam2Cys15, and Pam2Cys16 to be dysfunctional, since these lipopeptides failed to activate TLR2/6 reporter signaling or induce cytokines in BMDC. Although the first Cys is conserved in all the lipopeptides tested, the following sequences varied (12), even though all showed BMDC maturation activity. Notably, the second a. a. residue was Ser/Thr or Gly/Ala in the functional lipopeptides, followed by undefined sequences (4). A length of more than three a.a. was indispensable for BMDC-mediated NK activation (Fig. 1, Pam2Cys17 vs. 18). The failure of Pam2Cys13, Pam2Cys15, and Pam2Cys16 to activate NK cells suggests the importance of the second and/or third residue for stimulating BMDC or directing NK activation. Pam2Cys13 harbors Pro in the second residue, which breaks hydrogen bond interactions. Likewise, Pam2Cys15 and Pam2Cys16 commonly possess Leu and ILe in the second and third residues, which also destabilize hydrogen bond interactions. Thus, these a. a. residues critically influence the effectual interaction between the Pam2Cys peptides and the TLR2 complex on either BMDC or NK cells (4).

TLR2 initiates immune response by recognizing diacylated lipoproteins in combination with TLR6. We surmise that this receptor complex recognizes the a. a. properties in the peptide sequence that activate mDC/NK cells. Crystal structure analysis indicates that hydrogen bonds between glycerol and the peptide backbone of the ligand and the leucine-rich repeat (LRR)11 loops of TLRs are critical for TLR heterodimerization (19,20). These hydrogen bonds bridge TLR2 and TLR6 with the ligand, and fix the conformation of the hydrophobic residues around the dimerization interface (19). The side chains of the first two a. a. of Pam2Cys have substantial interactions with the TLRs. The N-terminal Cys binds to the sulfur site formed by the hydrophobic F325, L328, F349, L350, and P352 residues of TLR2, and the L318 residue of TLR6 (19). The hydroxyl side chains of the second Ser/Thr form a medium-range hydrogen bond with the F325 backbone of TLR2. As seen in the TLR2/TLR6/Pam2CSK4 structure, the side chains beyond the third lysine residue have highly flexible structures and form only weak ionic or hydrogen bond interactions with the TLRs (19). Hence, our results with a. a. substitutions fit the proposed TLR2-Pam2CSK4 interacting model. We actually demonstrated here that the peptide sequences have a significant effect on the immunological activity of the lipopeptides *in vitro*. The recognition system for bacterial lipoproteins has developed to sense common structures of the lipid, as well as the peptide sequences.

What is the *in vivo* role in these bacterial lipopeptides is the coming question. Intraperitoneal (i.p.) injection of Pam2Cys lipopeptides is expected to induce cytokines and NK cell activation *in vivo*. We tested this possibility using a syngenic system with tumor-implant mice. Actually in a previous report, MALP-2 lipopeptide is capable of inducing tumor regression in mouse models (32). However, our trials suggested that the ability of Pam2Cys lipopeptide to suppress tumor progression is less prominent *in vivo* than we had expected. After many challenges, we found that most of the Pam2Cys lipopeptide

tested acted on the immune cells to release IL-10 and induce Foxp3$^+$ Treg cells *in vivo* (10). Perhaps, this is a main reason why i.p.-challenged Pam2Cys lipopeptides fail to express NK function and resultant tumor regression. Breaking this immune-suppressive environment induced by TLR2 will be required for us to apply Pam2Cys lipopeptides for a clinically effective immune adjuvant. The *S. aureus* lipopeptides are compatible with this principle.

Taken together, we showed that *S. aureus* lipopeptides induce mDC-mediated NK activation. It is intriguing that this is a case of the reported reciprocal activation (21), in which ligands-receptors on mDC and NK cells are involved. In a. a. sequences of Pam2Cys, lysine distal to the N-terminal Pam2 and hydroxyl residues proximal to the Pam2 affect NK-activating potential through its interaction with TLR2. When bacteria invade host tissue, they encounter many proteases. Since plasma serine proteases frequently cleave the Lys-X sequence of substrates, the lipoproteins may be clipped out into liberated lipopeptides containing Lys, which could be important in the context of TLR2-induced inflammatory immune responses. In fact, after completing this manuscript, two in press papers were released where some bacterial components are shown to participate in TLR2-mediated NK activation (33,34). Our findings furthered these notions by analyzing synthetic Pam2Cys peptides under the knowledge of the structural background of TLR2 (19,20).

A question remaining is why bacteria provide two sorts of lipopeptides with TLR2-activating and –nonactivating properties. So far, we have no experimental finding to sufficiently answer this question, but bacterial infection usually alters host inflammatory milieu and recruits immune competent cells to the lesion (35). In this context, it is not surprising that Pam2Cys lipopeptides serve as modifiers for host immune response against bacteria. Different responses could be expected to occur with various combinations of Pam2Cys peptides in infectious lesion. Here we demonstrate that NK activation is a phenotype induced by TLR2-activating bacterial lipopeptides, which properties are determined by the peptide sequence of the Pam2Cys. Furthermore,

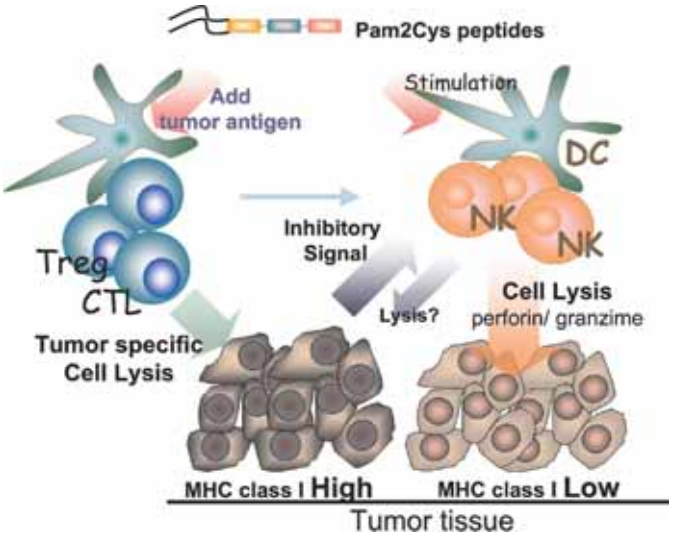

Fig. 10. Possible function of bacterial lipoproteins. Possible functions of bacterial lipopeptides acting on the immune system are depicted according to the literatures (26,37) and present study (38). The present study is summarized in Table 2.

they simultaneously induce IL-10 and Treg cells *in vivo* (10). Studies on these functional behaviors of lipopeptide towards mDC and on how TLR signals link NK activation and Treg induction in bacterial infectious diseases will be the next highlight for understanding the importance of early phase of innate cellular response against various bacterial infections (Fig. 10).

Footnote

Abbreviations

BM, bone marrow; DC, dendritic cells; EMCV, encephalomyocarditis virus; IFN, type I interferon; IPS-1, IFN-β promoter stimulator-1; IRF, interferon regulatory factor; MCMV, mouse cytomegalovirus; MDA5, melanoma differentiation associated gene 5; MEF, mouse embryonic fibroblasts; Mf, macrophages; MyD88, myeloid differentiation factor 88; PKR, ; PV, poliovirus; PVR, poliovirus receptor; RIG-I, retinoic acid inducible gene-1; TICAM-1, Toll/IL-1 receptor homology domain-containing adaptor molecule 1; TLR, toll-like receptor; WT, wild-type.

Acknowledgement

This work was supported in part by Waxmann Foundations. Financial supports by the Program of Founding Research Centers for Emerging and Reemerging Infectious Diseases, MEXT, is gratefully acknowledged.

Financial interest

Authors declare no competing of financial interest in this study.

References

(1) Haller D, Serrant P, Granato D, Schiffrin EJ, Blum S. (2002) Activation of human NK cells by staphylococci and lactobacilli requires cell contact-dependent costimulation by autologous monocytes. *Clin Diagn Lab Immunol* **9**: 649-657.

(2) Chavakis T, Preissner KT, Herrmann M. (2007) The anti-inflammatory activities of *Staphylococcus aureus*. *Trends Immunol*. **28**: 408-418.

(3) Takeuchi O, Hoshino K, Akira S. (2000) Cutting edge: TLR2-deficient and MyD88-deficient mice are highly susceptible to *Staphylococcus aureus* infection. *J Immunol* **165**: 5392-5396.

(4) Azuma M, Sawahata R, Akao Y, Ebihara T, Yamazaki S, Matsumoto M, Hashimoto M, Fukase K, Fujimoto Y, Seya T. (2010) The peptide sequence of diacyl lipopeptides determines dendritic cell TLR2-mediated NK activation. *PLoS ONE* **5**: e12550.

(5) Hamerman JA, Ogasawara K, Lanier LL. (2004) Cutting edge: Toll-like receptor signaling in macrophages induces ligands for the NKG2D receptor. *J Immunol* **172**: 2001-2005.

(6) Fujita M, Into T, Yasuda M, Okusawa T, Hamahira S, et al. (2003) Involvement of leucine residues at positions 107, 112, and 115 in a leucine-rich repeat motif of human Toll-like receptor 2 in the recognition of diacylated lipoproteins and lipopeptides and *Staphylococcus aureus* peptidoglycans. *J Immunol* **171**: 3675-3683.

(7) Nakao Y, Funami K, Kikkawa S, Taniguchi M, Nishiguchi M, et al. (2005) Surface-expressed TLR6 participates in the recognition of diacylated lipopeptide and peptidoglycan in human cells. *J Immunol* **174**: 1566-1573.

(8) Takeuchi O, Kawai T, Mühlradt PF, Morr M, Radolf JD, et al. (2001) Discrimination of bacterial lipoproteins by Toll-like receptor 6. *Int Immunol* **13**: 933-940.

(9) Fricke I, Mitchell D, Mittelstädt J, Lehan N, Heine H, Goldmann T, Böhle A, Brandau S. (2006) Mycobacteria induce IFN-gamma production in human dendritic cells via triggering of TLR2. *J Immunol*. **176**: 5173-5182.

(10) Yamazaki S, Okada K, Maruyama A, Matsumoto M, Yagita H, Seya T. (2011) TLR2-dependent induction of IL-10 and Foxp3$^+$ CD25$^+$ CD4$^+$ regulatory T cells prevents effective anti-tumor immunity induced by Pam2 lipopeptides in vivo. *PLoS One*. **6**: e18833.

(11) Metzger J, Jung G, Bessler WG, Hoffmann P, Strecker M, et al. (1991) Lipopeptides containing 2-(palmitoylamino)-6,7-bis(palmitoyloxy) heptanoic acid: synthesis, stereospecific stimulation of B-lymphocytes and macrophages, and adjuvanticity in vivo and in vitro. *J Med Chem* **34**: 1969-1974.

(12) Fujimoto Y, Hashimoto M. Furuyashiki M, Katsumoto M, Seya T, et al. (2009) Innate Immunostimulatory lipopepitdes of *Staphylococcus aureus* as TLR2 ligands; Prediction with mRNA expression, chemical synthesis and immunostimulatory activities. *ChemBioChem*. **10**: 2311-2315.

(13) Akazawa T, Okuno M, Okuda Y, Tsujimura K, Takahashi T, et al. (2007) Antitumor NK activation induced by the Toll-like receptor3-TICAM-1 (TRIF) pathway in myeloid dendritic cells. *Proc. Natl. Acad. Sci. USA*. **104**: 252-257.

(14) Ebihara T, Azuma M, Oshiumi H, Kasamatsu J, Iwabuchi K, Matsumoto K, Saito H, Taniguchi T, Matsumoto M, Seya T. (2010) Identification of a polyI:C-inducible membrane protein that participates in dendritic cell-mediated natural killer cell activation. *J Exp Med*. **207**: 2675-2687.

(15) Martinez J, Huang X, Yang Y. (2010) Direct TLR2

signaling is critical for NK cell activation and function in response to vaccinia viral infection. *PLoS Pathogen* **6**: e1000811.

(16) Marcenaro E, Ferranti B, Falco M, Moretta L, Moretta A. (2008) Human NK cells directly recognize Mycobacterium bovis via TLR2 and acquire the ability to kill monocyte-derived DC. *Int Immunol.* **20**: 1155-1167.

(17) Cerwenka A, Lanier LL. (2001) Natural killer cells, viruses and cancer. *Nat Rev Immunol* **1**: 41-49.

(18) Tanaka H, Mori Y, Ishii H, Akedo H. (1988) Enhancement of metastatic capacity of fibroblast-tumor cell interaction in mice. *Cancer Res* **48**: 1456-1459.

(19) Kang JY, Nan X, Jin MS, Youn SJ, Ryu YH, Mah S, Han SH, Lee H, Paik SG, Lee JO. (2009) Recognition of lipopeptide patterns by Toll-like receptor 2-Toll-like receptor 6 heterodimer. *Immunity*. **31**: 873-884.

(20) Jin MS, Kim SE, Heo JY, Lee ME, Kim HM, et al. (2007) Crystal structure of the TLR1-TLR2 heterodimer induced by binding of a tri-acylated lipopeptide. *Cell* **130**: 1071-1082.

(21) Gerosa F, Baldani-Guerra B, Nisii C, Marchesini V, Carra G, Trinchieri G. (2002) Reciprocal activating interaction between natural killer cells and dendritic cells. *J.Exp.Med.* **195**: 327-333.

(22) McCartney S, Vermi W, Gilfillan S, Cella M, Murphy TL, et al. (2009) Distinct and complementary functions of MDA5 and TLR3 in poly(I:C)-mediated activation of mouse NK cells. *J Exp Med.* **206**: 2967-2976.

(23) Schmidt J, Welsch T, Jäger D, Mühlradt PF, Büchler MW, Märten A. (2007) Intratumoural injection of the toll-like receptor-2/6 agonist 'macrophage-activating lipopeptide-2' in patients with pancreatic carcinoma: a phase I/II trial. *Brit. J. Cancer* **97**: 598-604.

(24) Akazawa T, Inoue N, Shime H, Sugiura K, Kodama K, Matsumoto M, Seya T. (2010) Adjuvant engineering for cancer immunotherapy: development of a synthetic TLR2 ligand with increased cell adhesion. *Cancer Sci*. **101**: 1596-1603.

(25) Akazawa T, Masuda H, Saeki Y, Matsumoto M, Takeda K, et al., (2004) Adjuvant-mediated tumor regression and tumor-specific cytotoxic response are impaired in MyD88-deficient mice. *Cancer Res*. **64**: 757-764.

(26) Miyake T, Kumagai Y, Kato H, Guo Z, Matsushita K, et al, (2009) Poly I:C-induced activation of NK cells by CD8 alpha$^+$ dendritic cells via the IPS-1 and TRIF-dependent pathways. *J. Immunol*. **183**: 2522-2528.

(27) Sun CM, Hall JA, Blank RB, Bouladoux N, Oukka M, et al. (2007) Small intestine lamina propria dendritic cells promote de novo generation of Foxp3 T reg cells via retinoic acid. *J Exp Med*. **204**: 1775-1785.

(28) Coombes JL, Siddiqui KR, Arancibia-Carcamo CV, Hall J, Sun CM, et al. (2007) A functionally specialized population of mucosal CD103$^+$ DCs induces Foxp3$^+$ regulatory T cells via a TGF-beta and retinoic acid-dependent mechanism. *J Exp Med*. **204**: 1757-1764.

(29) Manicassamy S, Ravindran R, Deng J, Oluoch H, Denning TL, et al. (2009) Toll-like receptor 2-dependent induction of vitamin A-metabolizing enzymes in dendritic cells promotes T regulatory responses and inhibits autoimmunity. *Nat Med*. **15**: 401-409.

(30) Collison LW, Pillai MR, Chaturvedi V, Vignali DA (2009) Regulatory T cell suppression is potentiated by target T cells in a cell contact, IL-35- and IL-10-dependent manner. *J Immunol*. **182**: 6121-6128.

(31) Murai M, Turovskaya O, Kim G, Madan R, Karp CL, et al. (2009) Interleukin 10 acts on regulatory T cells to maintain expression of the transcription factor Foxp3 and suppressive function in mice with colitis. *Nat Immunol*. **10**: 1178-1184.

(32) Sawahata R, Shime H, Yamazaki S, Inoue N, Akazawa T, Fujimoto Y, Fukase K, Matsumoto M, Seya T. (2011) Failure of mycoplasma lipoprotein MALP-2 to induce NK cell activation through dendritic cell TLR2. *Microbes Infect*. **13**: 350-358.

(33) Lindgren A, Pavlovic V, Flach CF, Sjöling A, Lundin S. (2011) Interferon-gamma secretion is induced in IL-12 stimulated human NK cells

by recognition of Helicobacter pylori or TLR2 ligands. *Innate Immun*. **17**: 191-203.
(34) Mian MF, Lauzon NM, Andrews DW, Lichty BD, Ashkar AA. (2010) FimH can directly activate human and murine natural killer cells via TLR4. *Mol Ther*. **18**: 1379-1388.
(35) Buwitt-Beckmann U, Heine H, Wiesmüller KH, Jung G, Brock R, et al. (2006) TLR1- and TLR6-independent recognition of bacterial lipopeptides. *J Biol Chem* **281**: 9049-9057.
(36) Seya T, Kasamatsu J, Azuma M, Shime H, Matsumoto M. (2011) Natural killer cell activation secondary to innate pattern sensing. *J. Innate Immun.* **3**: 264-273.
(37) Seya T, Shime H, Ebihara T, Oshiumi H, Matsumoto M. (2010) Pattern-recognition receptors of innate immunity and their application to tumor immunotherapy. *Cancer Sci.* **101**: 313-320.
(38) Azuma M, Matsumoto M, Seya T. (2011) The Natural killer cell activation by Pam2 lipopeptides. *Molecules*. (in press).


THE
WAKSMAN
FOUNDATION
OF
JAPAN
INC.